University of Wollongong Thesis Collection

2013

Study of pinning and supercurrent enhancement in doped MgB2

Feixiang Xiang
University of Wollongong, fx963@uow.edu.au

Recommended Citation

UNIVERSITY OF WOLLONGONG

Institute for Superconducting and Electronic Materials

Faculty of Engineering

Study of pinning and supercurrent enhancement in doped MgB$_2$

Feixiang Xiang

"This thesis is presented as part of the requirements for the award of the Degree of

Master of Engineering by Research

of the University of Wollongong"

Month and Year

CERTIFICATION

I, Feixiang Xiang, declare that this thesis, submitted in partial fulfilment of the requirements for the award of Master of Engineering by Research, in the Institute for Superconducting and Electronic Materials, Faculty of Engineering, University of Wollongong, is wholly my own work unless otherwise referenced or acknowledged. The document has not been submitted for qualifications at any other academic institution.

Feixiang Xiang

2013

ABSTRACT

MgB$_2$ is one candidate of the superconductors for practical application. Most of the applications require the high critical current density (J_c) which means high performance and cost-effective. However the J_c of pristine MgB$_2$ is far from the theoretical depairing current density because of the weak flux pinning and poor grain connectivity. In the work of this Master degree by research, several dopants were tried to enhance the J_c, meanwhile their corresponding flux pinning mechanism were studied.

The first three chapters of this thesis give the introduction, literature review and experimental methods. They cover the research motivation, basic superconducting properties of MgB$_2$, status quo of MgB$_2$ research on enhancement of upper critical field H_{c2} and J_c, and various experimental methods which are employed in this work.

The last two chapters, chapter 4 and chapter 5, present the main experimental works of this thesis.

In chapter 4, the effect of graphene oxide (GO) doping on improvement of J_c in MgB$_2$ was systematically studied with emphasis on flux pinning mechanism. It was confirmed that both of low field J_c and high field J_c could be enhanced by GO doping, and the high field J_c was further improved by optimized doping level. The low field and high field J_c improvement are due to the improved the grain connectivity and enhanced flux pinning, respectively. To understand the superior performance of GO doped MgB$_2$, the flux pinning mechanism was studied systematically. In the framework of the collective pinning theory, a B-T phase diagram has been constructed and in the single vortex regime, the transformation of pinning mechanism from transition temperature fluctuation induced pinning (δT_c pinning) to

mean free path fluctuation induced pinning (δl pinning) is observed in MgB_2 by adjusting the GO doping level. Furthermore, in terms of the thermally activated flux flow model the pinning potential in high field ($B > 5$ T) is enhanced by GO doping.

In chapter 5, Based on the overall improvement of J_c in GO doped MgB_2 and excellent high field J_c for nano-SiC doping, the effect of GO and nano-SiC co-doping effect on the superconductivity of MgB_2 was systematically examined by powder x-ray diffraction, transport and magnetization measurement. By co-doping impurity phases Mg_2Si and SiC appeared and a axis decreased and c axis remained unchanged. Compared with the un-doped samples, J_c was improved at high field for both of 5 K and 20 K. Compared with the 2wt % GO doped sample, at 20 K the J_c was further enhanced by co-doping but at 5 K the J_c improvement was not obvious as at 20 K. At 20 K, the normalized pinning force showed enhancement at high field compared with un-doped one but decrease compared with 2wt% GO doped ones. According to the thermally activated flux flow model, the pinning potentials of co-doped samples were further enhanced at high field.

DEDICATION

To my family

ACKNOWLEDGEMENTS

grandmother for your love to me since when I was born, I hope you are happy in the heaven and bless me as before.

TABLE OF CONTENTS

LIST OF FIGURES

x

LIST OF TABLES

No table of figures entries found.

1 INTRODUCTION

The superconductivity around 40K (Fig. 1.1) in MgB_2 was discovered in 2001 by Akimitsu group from Aoyama-Gakuin University, Japan[1]. Its T_c compared with intermetallic compound is relatively high, nearly doubling the T_c of conventional superconductors. And the crystal structure as shown in the Fig. 1.2 is simple which is advantageous for preparation.
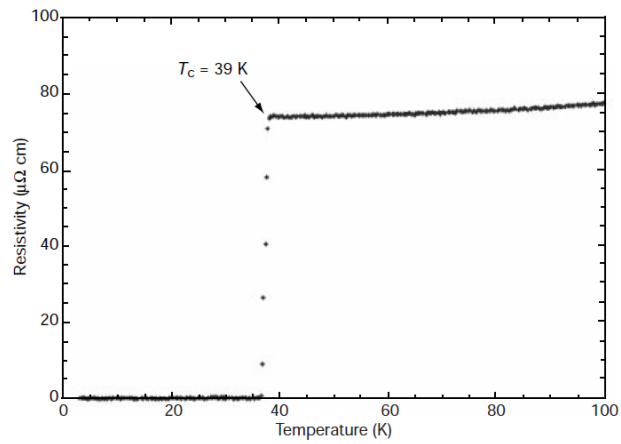
Figure 1.1 Temperature dependence of the resistivity of MgB2 under zero magnetic field.

Figure 1.2 Cystal structure of MgB_2.

1
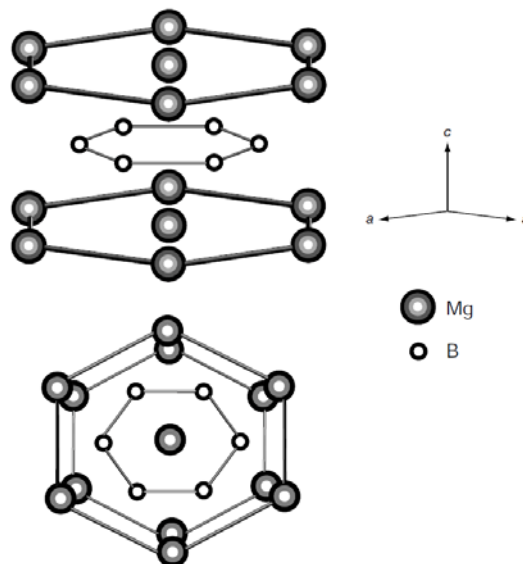
Soon after the discovery of its superconductivity, MgB_2 shows the promise for practical applications. First, it was proved the grain boundaries of MgB_2 are transparent to the supercurrent flow. This is different from the high temperature superconductors which exhibit very high transition temperature but the transport current densities of which are quite low in untextured polycrystalline sample[2]. As shown in the Fig. 1.3, the regions with a large number of high-angle grain boundaries support high current densities of the order of 10^5 Acm^{-2}, which they could not sustain if there are any inherent strong suppression of current across the grain boundaries[2].
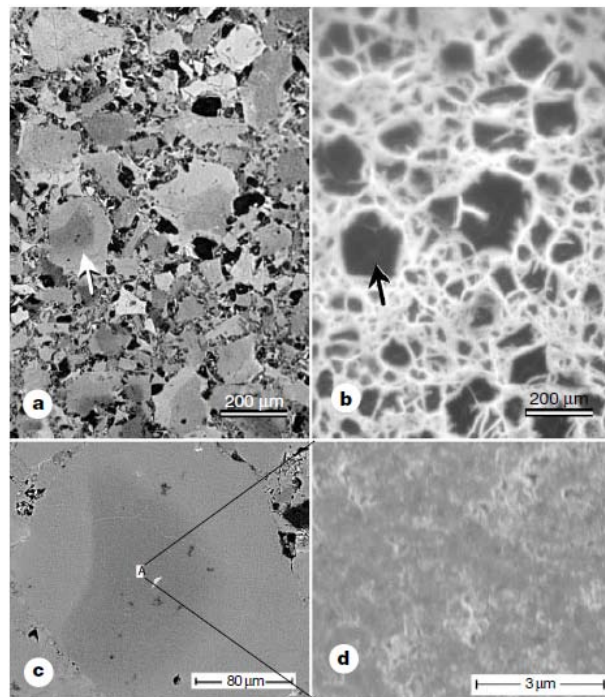
Figure 1.3 Summary of microstructural and magneto-optical analyses. Polarized light microscope and magneto-optical images of the same area of sample B are compared in **a** and **b**, respectively. Bright regions of **b** indicate areas where magnetic flux has penetrated the sample after a field of 120 mT was applied after cooling the sample in zero field to 11 K. Although the pronounced differences in contrast indicate extensive inhomogeneity of the sample, the dark regions represent areas of strong superconductivity and large screening currents. Image **c** presents a magnified view using SEM backscattered electron imaging of the strongly superconducting region marked with an arrow in **a** and **b**. At higher resolution, image **d**, a secondary electron examination of the central region in **c**, reveals that the area marked by an arrow in **a** and **b** has ~100-nm, fine-scale structure.

Second, the flux pinning of MgB_2 was proved can be enhanced by traditional routes that has already been successfully applied in the low- and high-temperature superconductors. Eom et al. employed the thin film deposition method and improve the magnetic J_c at 4.2 K above $10^5 Acm^{-2}$ at nearly 10 T by alloying with oxygen, as shown in Fig. 1.4[3]. On the other hand, Bugoslavsky et al. use proton irradiation to induce crystalline disorder in bulk samples of MgB_2. Through this treatment, the reduction of J_c in magnetic field at 20 K is much slower than in untreated samples as shown in Fig. 1.5, whereas the irreversibility field doubles on irradiation, about the same improvement observed by Eom.et al. in their thin films[4, 5].
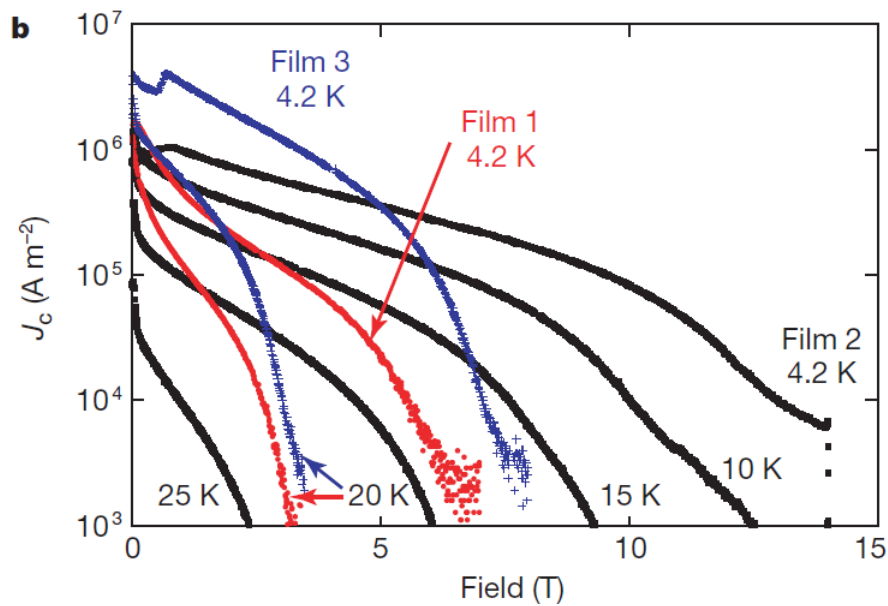
Figure 1.4 The derived values of the critical current density are plotted as a function of field at 4.2 and 20 K for films 1 and 3, and at 4.2, 10, 15, 20, and 25 K for film 2. We note that the data for film 2 at 4.2 K are above 10^5 A cm^{-2} (a common benchmark for superconducting magnet applications) at nearly 10 T.
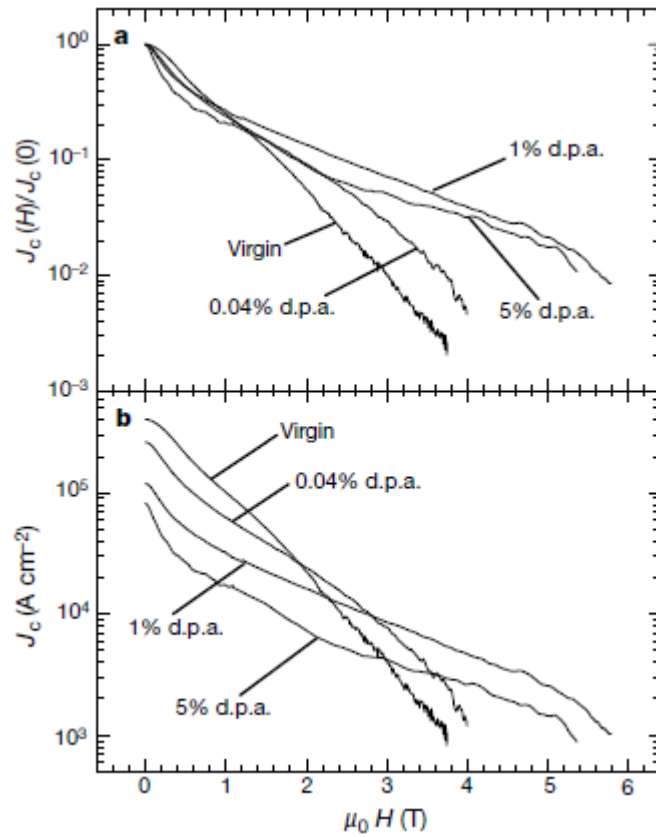
Figure 1.5 Effect of irradiation on the field-dependence of *Jc* at 20 K; the behaviour at other temperatures is similar. Jc is obtained from the magnetization hysteresis width, using the Bean model.

Third, MgB2 wires could be fabricated by powder-in-tube (PIT) method and the iron could be used as the sheath material which is cheap as shown in Fig.1.6[6]. The *Jc* at 25 K and 1 Tesla fields reach as high as 30,000 Acm-2 as shown in Fig. 1.7 which is already high enough for power transmission cables[6].
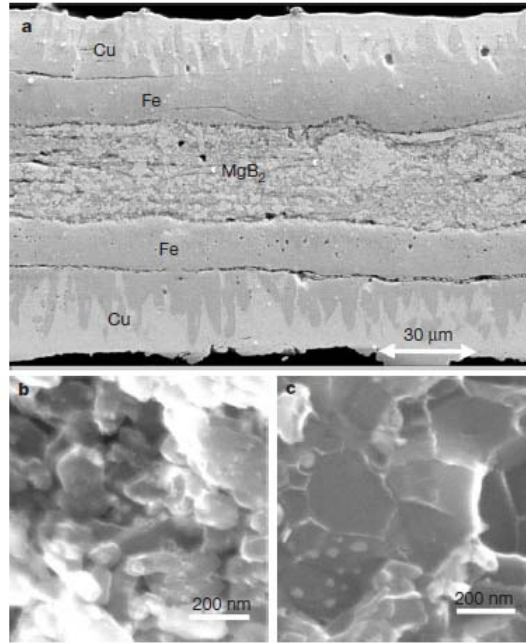
Figure 1.6 left, Microstructure of the MgB2 ribbons were fabricated using Fe or Cu/Fe tubes with outside diameters of 5±6.35 mm.
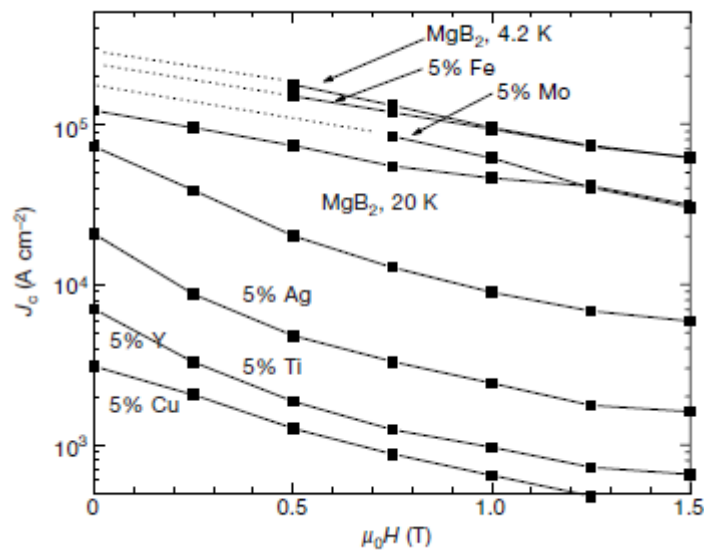
Figure 1.7 J_c (magnetization) versus H plots for various MgB_2 samples.

For industrial application, the thin film method and proton radiation method still cost too much. The alternative method is chemical doping, which is low cost but effective. Atomic substitution shifts the Fermi level and enhances impurity

scattering, thus increasing the upper critical field, H_{c2}, and also introduces point defects which act as the pinning centers, therefore leading to the higher irreversibility field, H_{irr}, and critical current density, J_c, in field.

In the past 11 years, several dopants such as nano-SiC[7], CNTs[8], nano Si[9], carbohydrate[10], silicon oil[11], and so on, have been found having positive effects on H_{c2}, H_{irr} and J_c. Among them, nano-SiC doping has been proved as the most effective dopants to improve the high field Jc. As shown in Fig. 1.8, at 5 K and 8 T, the J_c can be improve more than an order of magnitude by nano-SiC doping. However, also as shown in the Fig. 1.8, the there is a crossover between Jc curves of the undoped and doped one inn low fields. Recently, our team has found that graphene can improve J_c at self field and low field with very little reduction in T_c, because the graphene doping can improve the grain connectivity. But its high field J_c is not competitive with that of nano-SiC doped one. Also, we very recently found the graphene oxide (GO) doping can improve both the low and high field J_c, and the high field J_c is better than the graphene doping.
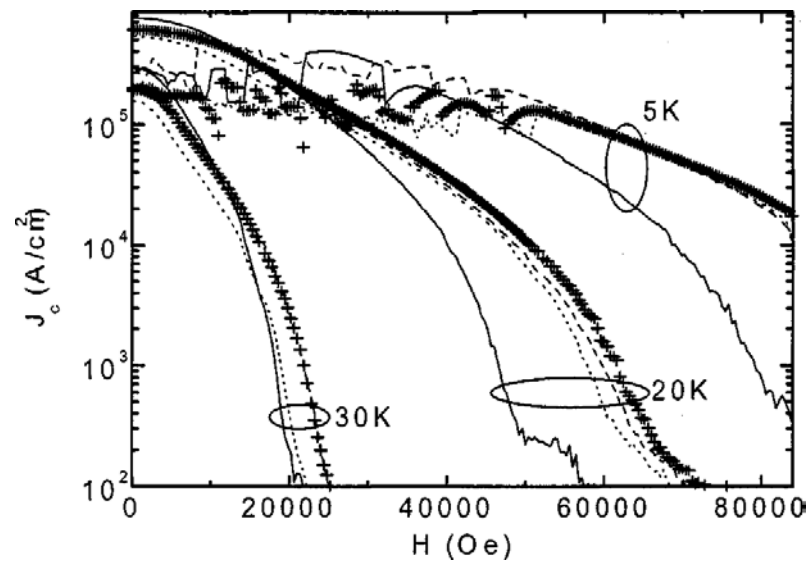
Figure 1.8 Magnetic Jc for nano-SiC doped MgB$_2$.

6

In type-II superconductors, due to its short coherence length, the most effective elementary interaction between vortex and pinning center is core interaction, which originates from the coupling of locally distorted superconducting properties with the periodic variation of the superconducting order parameter. Inhomogeneities in different parameters cause different "elementary pinning mechanisms". There exists two predominant mechanisms of core pinning, i.e. δT_c pinning and δl pinning. Whereas δT_c pinning is caused by the spatial variation of the GL coefficient α associated with disorder in the transition temperature T_c, variations in the charge-carrier mean free path l near lattice defects are the main cause of δl pinning[12, 13]. For MgB_2 superconductor, it has been shown that δT_c pinning is dominant in un-doped MgB_2 samples, and δl pinning is dominant in carbon doped MgB_2 bulks, while δT_c and δl pinning coexist in silicone oil doped bulk samples[14-16]. But the systematical transformation from δT_c to δl pinning has not been observed.

As described above, the disorder which comes from the defects or inhomogeneity will pinning the vortices, and therefore maintain the zero resistance state. Whereas thermal energy may allow flux lines jump from one pinning site to another, which causes the finite resistivity below the transition temperature. It manifests a field-dependent broadening of the resistive transition. This phenomenon is very prominent in high temperature superconductors because of their large anisotropy induced by the 2D structure and high transition temperatures. With a layer structure and relatively high T_c, thermally activated flux flow also results in the field-dependent broadening of the resistive transition in MgB_2. But it exhibits different behaviour compared to the high temperature superconductors (HTS)[17-19]. First, the U_0 is very large in low field, on the order of 10^4 K; second, it exhibits very strong field dependence in high

field[20]. So far, research on MgB_2 has been focused on pristine samples, however, with only limited studies reported on doping effects on U_0.[21, 22].

In the research of my Master study, I will study the pinning and supercurrent enhancement in doped MgB_2. The graphene oxide (GO) will be used as a dopant to confirm the improvement of the overall in-field J_c and optimize the experimental procedure to further improve the J_c. By study of the H_{irr}, H_{c2}, vortex phase diagram, pinning types and pinning potential and grain connectivity, the mechanism of the overall in-field J_c improvement will be understood. After that, the GO doping will be applied to improve the performance of the MgB_2 wires.

References:

1.   J. Nagamatsu, N. Nakagawa, T. Muranaka, Y. Zenitani and J. Akimitsu, Nature **410** (6824), 63-64 (2001).

2.   D. C. Larbalestier, L. D. Cooley, M. O. Rikel, A. A. Polyanskii, J. Jiang, S. Patnaik, X. Y. Cai, D. M. Feldmann, A. Gurevich, A. A. Squitieri, M. T. Naus, C. B. Eom, E. E. Hellstrom, R. J. Cava, K. A. Regan, N. Rogado, M. A. Hayward, T. He, J. S. Slusky, P. Khalifah, K. Inumaru and M. Haas, Nature **410** (6825), 186-189 (2001).

3.   C. B. Eom, M. K. Lee, J. H. Choi, L. J. Belenky, X. Song, L. D. Cooley, M. T. Naus, S. Patnaik, J. Jiang, M. Rikel, A. Polyanskii, A. Gurevich, X. Y. Cai, S. D. Bu, S. E. Babcock, E. E. Hellstrom, D. C. Larbalestier, N. Rogado, K. A. Regan, M. A. Hayward, T. He, J. S. Slusky, K. Inumaru, M. K. Haas and R. J. Cava, Nature **411** (6837), 558-560 (2001).

4.   Y. Bugoslavsky, L. F. Cohen, G. K. Perkins, M. Polichetti, T. J. Tate, R. Gwilliam and A. D. Caplin, Nature **411** (6837), 561-563 (2001).

5.   P. Grant, Nature **411** (6837), 532-533 (2001).

6.   S. Jin, H. Mavoori, C. Bower and R. B. van Dover, Nature **411** (6837), 563-565 (2001).

7.   S. X. Dou, S. Soltanian, J. Horvat, X. L. Wang, S. H. Zhou, M. Ionescu, H. K. Liu, P. Munroe and M. Tomsic, Applied Physics Letters **81** (18), 3419-3421 (2002).

8.   S. X. Dou, W. K. Yeoh, O. Shcherbakova, D. Wexler, Y. Li, Z. M. Ren, P. Munroe, S. K. Chen, K. S. Tan, B. A. Glowacki and J. L. MacManus-Driscoll, Advanced Materials **18** (6), 785-788 (2006).

9.   X. L. Wang, S. H. Zhou, M. J. Qin, P. R. Munroe, S. Soltanian, H. K. Liu and S. X. Dou, Physica C: Superconductivity **385** (4), 461-465 (2003).

10.   J. H. Kim, S. Zhou, M. S. A. Hossain, A. V. Pan and S. X. Dou, Applied Physics Letters **89** (14), 142505-142503 (2006).

11.   X. L. Wang, Z. X. Cheng and S. X. Dou, Applied Physics Letters **90** (4), 042501-042503 (2007).

12.   G. Blatter, M. V. Feigel'man, V. B. Geshkenbein, A. I. Larkin and V. M. Vinokur, Reviews of Modern Physics **66** (4), 1125-1388 (1994).

13.   W. Roger, Reports on Progress in Physics **62** (2), 187 (1999).

14.   M. J. Qin, X. L. Wang, H. K. Liu and S. X. Dou, Physical Review B **65** (13), 132508 (2002).

15.   J. L. Wang, R. Zeng, J. H. Kim, L. Lu and S. X. Dou, Physical Review B **77** (17), 174501 (2008).

16.   S. R. Ghorbani, X. L. Wang, S. X. Dou, S.-I. K. Lee and M. S. A. Hossain, Physical Review B **78** (18), 184502 (2008).

17.   T. T. M. Palstra, B. Batlogg, L. F. Schneemeyer and J. V. Waszczak, Physical Review Letters **61** (14), 1662-1665 (1988).

18. T. T. M. Palstra, B. Batlogg, R. B. van Dover, L. F. Schneemeyer and J. V. Waszczak, Physical Review B **41** (10), 6621-6632 (1990).

19. X. L. Wang, A. H. Li, S. Yu, S. Ooi, K. Hirata, C. T. Lin, E. W. Collings, M. D. Sumption, M. Bhatia, S. Y. Ding and S. X. Dou, Journal of Applied Physics **97** (10), 10B114-113 (2005).

20. A. Sidorenko, V. Zdravkov, V. Ryazanov, S. Horn, S. Klimm, R. Tidecks, A. Wixforth, T. Koch and T. Schimmel, Philosophical Magazine **85** (16), 1783-1790 (2005).

21. J. Chen, V. Ferrando, P. Orgiani, A. V. Pogrebnyakov, R. H. T. Wilke, J. B. Betts, C. H. Mielke, J. M. Redwing, X. X. Xi and Q. Li, Physical Review B **74** (17), 174511 (2006).

22. K. S. B. De Silva, X. Xu, S. Gambhir, X. L. Wang, W. X. Li, G. G. Wallace and S. X. Dou, Scripta Materialia **65** (7), 634-637 (2011).

2 LITERATURE REVIEW

2.1   Crystal structure

The X-ray diffraction (XRD) pattern measured at room temperature is shown in Fig. 2.1(a)[1]. All the intense peaks can be indexed assuming a hexagonal unit cell, with a = 0.3086 nm and c = 0.3524 nm. The crystal structure of MgB_2 with the space group P6/mmm is shown in the Fig. 2.2[1], which consists of two homey boron layers with one magnesium layer located the centre of the hexagons In-between the boron planes. In boron layers, each boron atom is equidistant from three other boron atoms of which the structure is the same as structure of carbon layer of the graphite.
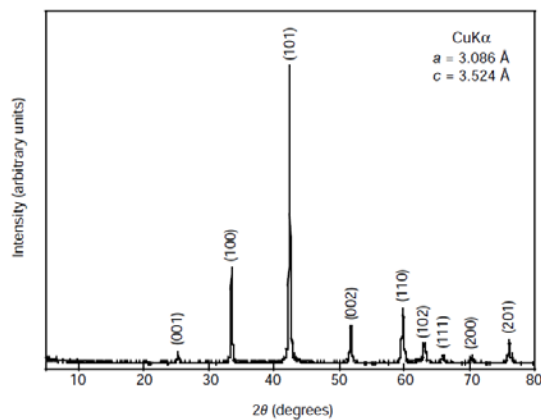
Figure 2.1 X-ray diffraction pattern of MgB_2 at room temperature[1];
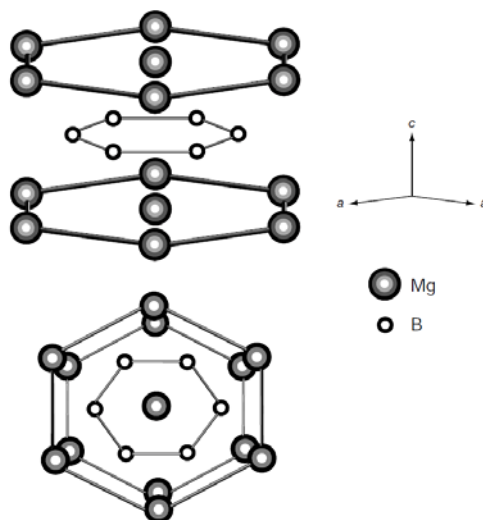
Figure 2.2 Crystal structure of MgB_2[1].

2.2   Electronic structure

The electrons at the Fermi surface of MgB_2 are mainly p electrons of boron, with Mg donating its s electrons to the conducting bands[2-4]. There are four conducting bands. From the σ–bonding $p_{x,y}$ orbitals of boron two σ bands are derived, whereas two π bands are derived from the π-binding (hole-like) and antibonding (electron-like) p_z orbitals. The σ states are two-dimensional confined in the boron planes and the π states are three-dimensional extending in all the direction[4, 5]. The charge density distribution shows that the bonds within the boron layers are strongly covalent, whereas the bonds between these layers are metallic[6]. The Fermi surface of MgB_2 is shown in Fig. 2.3. The two cylinders around the Γ-A lines are the two σ bands and the two webbed tunnels are due to the two π bands. The densities of states at the Fermi level are 0.300 states eV^{-1}/cell for the two σ bands and 0.410 states eV^{-1}/cell for the two π bands[6, 7].

The impurity scattering between the σ and π bands are small, as argued Mazin $et\ al$[8]. This is mainly because the $p_{x,\ y}$ (in-plane) and p_z (out-of-plane) orbitals are orthogonal to each other, and the overlap integrals which determine the interband coupling and interband impurity scattering are strongly reduced. Further, the p_z orbitals have odd parity and the $p_{x,y}$ ortibals have even parity with respect to the B layer, leading to small hybridization between the σ and π bands[8].
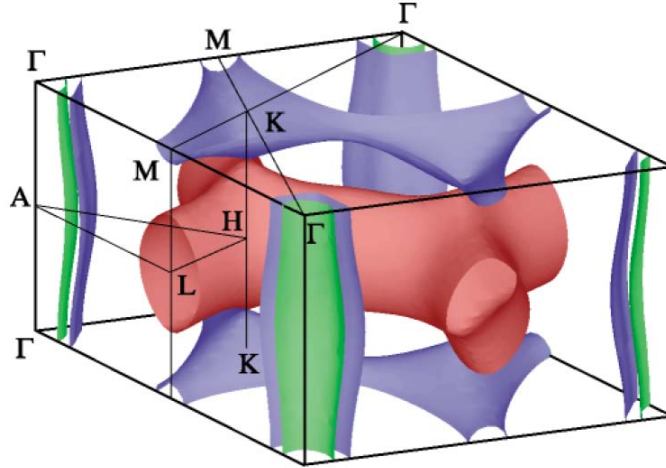
Figure2.3 The Fermi surface of MgB$_2$. Green and blue cylinders (holelike) come from the bonding $p_{x,y}$ bands, the blue tubular network (holelike) from the bonding p_z bands, and the red (electronlike) tubular network from the antibonding p_z band. The last two surfaces touch at the K point[4].

2.3   The E$_{2g}$ phonon and electron-phonon coupling

There are four phonon modes at the Brillouin zone center in MgB$_2$: the B$_{1g}$, E$_{2g}$, A$_{2u}$, and E$_{1u}$ modes[9,10]. The E$_{2g}$ mode involves the in-plane vibration of the boron ions in opposite directions (bond stretching). This motion changes the $p_{x,y}$ ortital overlap; therefore the electron-phonon coupling between the E$_{2g}$ mode and the σ band is very strong[3, 4, 10], as shown in Fig.2.4. It is this strong electron-phonon coupling that leads to the high T_c in MgB$_2$.

The E$_{2g}$ phonon is anharmonic" the dependence of the phonon energy on boron displacement has a large fourth-power term[10, 11]. The harmonicity is confined to phonons near the г–A line, where the electron-phonon coupling is also very large[12]. The anharmonicity causes the electron-phonon couplings as compared with the harmonic phonon, although the estimate of the phonon frequency shift depends on the methods of calculation[13].
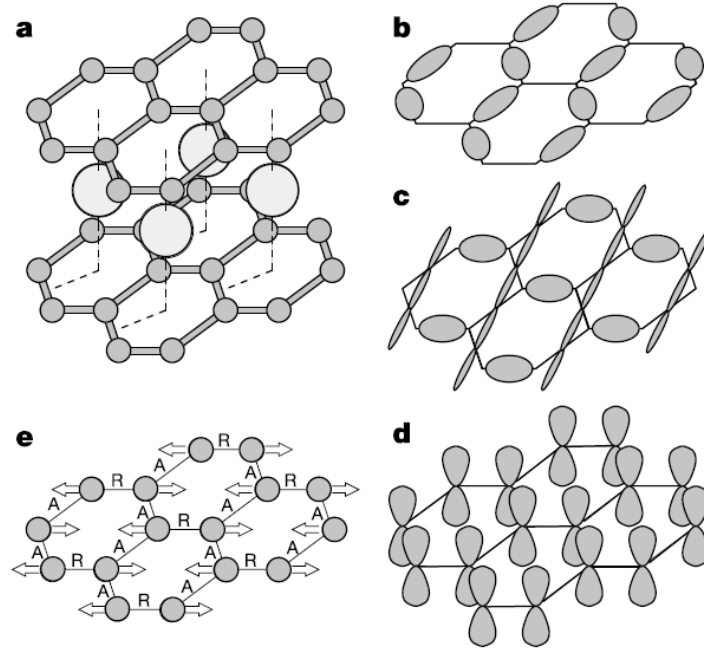
Figure 2.4 Crystal structure of MgB$_2$, electronic states at the Fermi level, and a vibrational mode of boron atoms. **a**, Crystal structure of MgB$_2$. Boron atoms form honeycomb planes, and magnesium atoms occupy the centres of the hexagons in-between boron planes. **b, c**, σ-bonding states at the Fermi level derived from boron p$_{x,y}$ orbitals. **d**, A σ-bonding state at the Fermi level derived from boron p_z orbitals. **e**, A vibrational mode of boron atoms that couples strongly to σ-bonding electronic states at the Fermi level. As boron atoms move in the arrow directions, shortened bonds, marked with 'A', become attractive to electrons, whereas elongated bonds, marked with 'R', become repulsive. The σ-bonding states (**b, c**) couple strongly to the vibrational mode because they are mainly located in either the attractive or the repulsive bondings of the mode. The π-bonding states (**d**) do not couple strongly to this mode[5].

Because there are four conduction bands, the electron-phonon coupling constant becomes a 4x4 matrix including phonon-mediated scattering of electron from any one of the 4 bands to any other of the 4 bands[7, 11]. Since the two σ bands are similar and the two π bands are similar (even though one π band is hole-like and the other is electron-like), the matrix is most often simplified to 2x2, and MgB$_2$ is referred to as a two-band superconductors[11]. The electron-phonon coupling constant matrix elements have been calculated by various groups: $\lambda_{\sigma\sigma}$=0.96, $\lambda_{\pi\pi}$=0.29, $\lambda_{\sigma\pi}$=0.23, $\lambda_{\pi\sigma}$=0.17 and the total λ=0.77 by Liu and co-wokers[6, 11]; $\lambda_{\sigma\sigma}$=1.017, $\lambda_{\pi\pi}$=0.448, $\lambda_{\sigma\pi}$=0.213,

$\lambda_{\pi\sigma}$=0.155 and λ=0.87 by Golubov *et al*[7]; $\lambda_{\sigma\sigma}$=0.78, $\lambda_{\pi\pi}$=0.21, $\lambda_{\sigma\pi}$=0.15, $\lambda_{\pi\sigma}$=0.11 and λ=0.61 by Choi *et al* (obtained from integration of $\lambda(\boldsymbol{k}, \boldsymbol{k'})$ over the Fermi surfae[6, 12]) and $\lambda_{\sigma\sigma}$=0.83, $\lambda_{\pi\pi}$=0.28, $\lambda_{\sigma\pi}$=0.22, $\lambda_{\pi\sigma}$=0.16 and λ=0.71 Floris *et al*[14]. Despite some differences among the results, it is clear that the electron-phonon coupling is very strong for the σ bands and much weaker for the π bands. The interband coupling is even weaker, although it is not negligible[15].

2.4 Two-gap superconductivity

From the information on the electron-phonon coupling constant matrix elements and with appropriate semi-phenomenological Columb pseudo-potential matrix elements, the superconducting energy gap and T_c were calculated[7, 11]. The results show 2 gaps, Δ_σ and Δ_π, that vanish together as the temperature increases towards T_c[7], in agreement with the experimental results such as that shown in Fig.2.5.
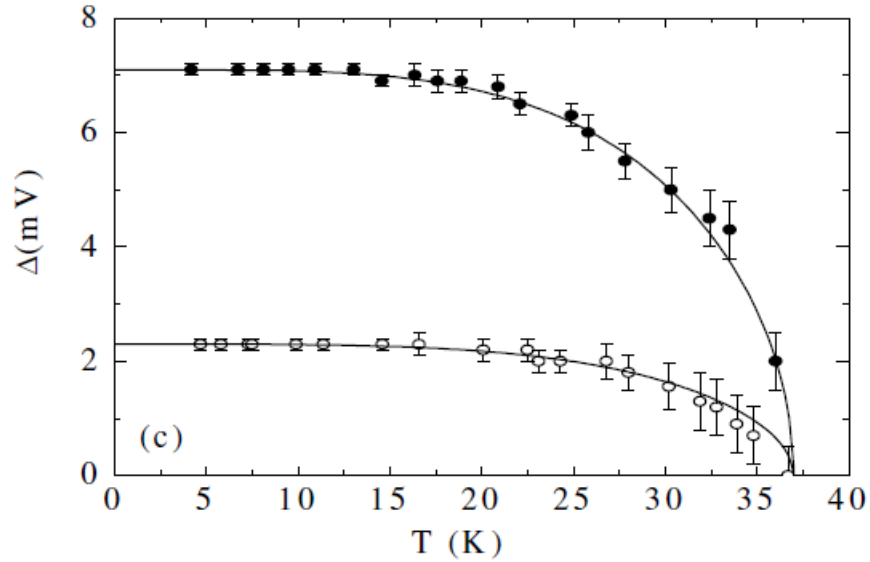
Figure 2.5 Values of the two gaps in MgB_2 extracted from the scanning tunnelling spectroscopy as a function of temperature. The lines are the BCS $\Delta(T)$[16].

The details of the two-band superconductivity have been described by Choi et al[5], who employed an anisotropic Eliashberg formalism and calculated the electron-phonon coupling constant for electron pairs originating from all sheets of the Fermi surface[12]. The energy gap value for each point of the Fermi surface is shown in Fig. 2.6 (a). The colour scale corresponds to the distribution of gap values shown in Fig. 2.6 (b). The gap on the σ bands ranges from 6.4 to 7.2 meV with an average of 6.8 meV, and on the π bands it ranges from 1.2 to 3.7 meV with an average of 1.8 meV[5]. From the BSC relation $\Delta(0)=1.764kT_c$, the σ gap would lead to a superconductor with T_c of 45 K and π gap to T_c of 15K. Because of the finite interband coupling, superconductivity occurs at a T_c of 39K in MgB_2[17].
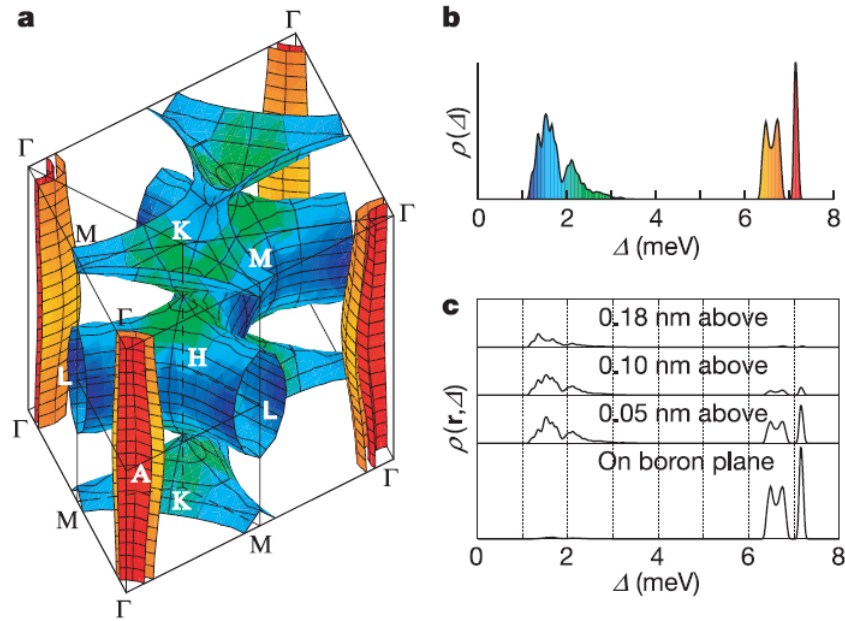
Figure 2.6 The superconducting energy gaps on the Fermi surface for MgB_2 from the band structure calculation. The color scale corresponds to the distribution of gap values shown in (**b**)[5].

Mazin et al have argued that that it is not necessary to use the fully anisotropic Eliashberg formalism and the two-gap formalism is sufficient unless the intraband scattering is small and the mean free path of the sample is greater than 1500Å[12].

2.5 Experimental evidences for two bands and two gaps

The first experimental hint to the two-band superconductivity came from the specific heat measurements[18,19,20]. As shown in Fig. 2.7 where the electronic specific heat is plotted as a function of temperature, the experimental data cannot be explained by the one-gap BCS model with a T_c of 39.4K[5]. At lower temperatures, the experimental results become higher than the BCS curve and then show another decrease to zero suggestive of another transition. This shoulder is a strong indication of a second, smaller gap. Also plotted in the figure is the result of the calculation by Choi *et al* using two gaps shown in Fig. 2.5, and it is in excellent agreement with the experiments[5]. The low temperature shoulder is caused by the excitations across the π gap.
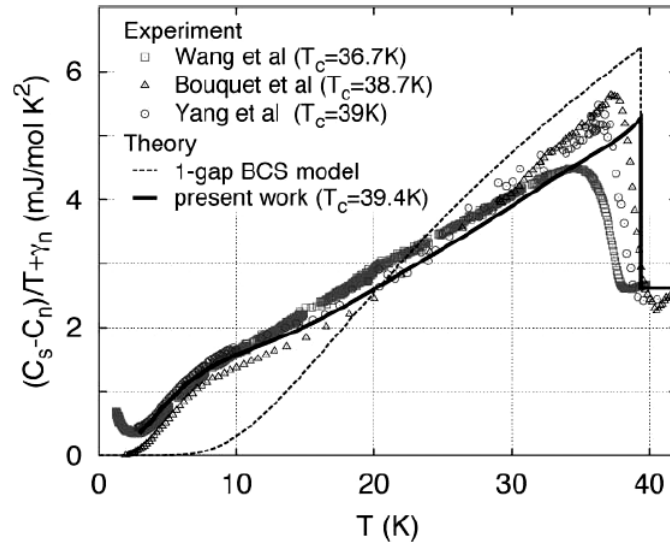
Figure 2.7 Electronic contribution to the specific heat as a function of temperature for MgB_2. The solid curve is the result of a two-gap model calculation. The dashed curve is the single-gap BCS prediction for a superconductor with T_c of 39.4 K[5].
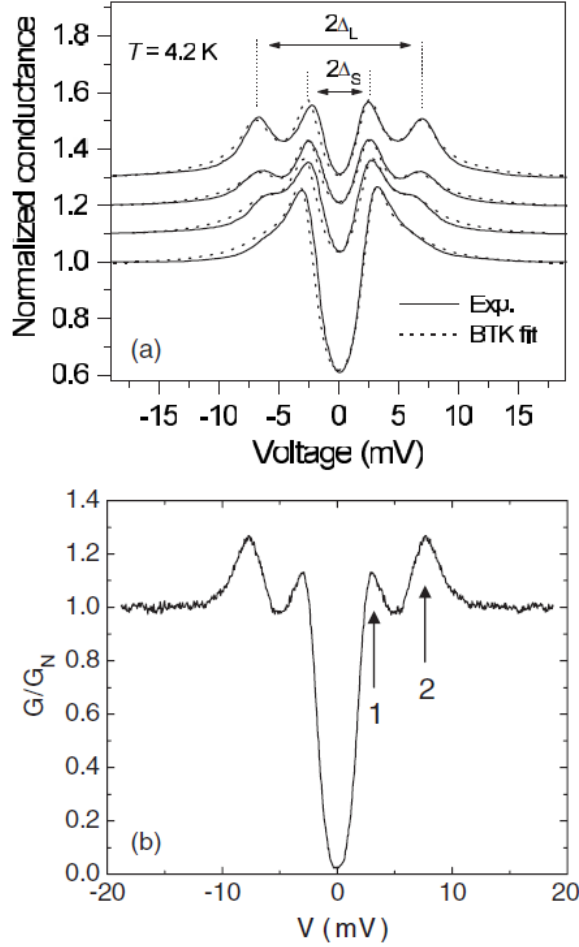
Figure 2.8 (*a*) Cu–MgB$_2$ point-contact spectra at $T = 4.2$K (solid lines) for several polycrystalline MgB$_2$ samples. The dotted lines are BTK model fitting results. (*b*) An STM spectrum tunneling into the *ab* plane on an off-axis MgB$_2$ epitaxial film at 4.2 K[21].

Point-contact spectroscopy[21-24] and tunnelling spectroscopy[16, 25, 26] allow direct measurement of the superconducting gap. Fig. 2.8(*a*) shows the Cu–MgB$_2$ point-contact spectra on several polycrystalline MgB$_2$ samples measured at $T = 4.2$K by Szabo *et al*[21]. The dotted lines are the two-band Blonder–Tinkham–Klapwijk (BKT) model fits with different barrier transparencies and weight factors (from 65% to 95% π-band contribution). Conductance peaks corresponding to the two gaps are clearly observed: $\Delta_\sigma = 6.8$ meV and $\Delta_\pi = 2.8$ meV. Fig. 2.8(*b*) shows tunnelling spectrum on an off-axis MgB$_2$ epitaxial film measured at 4.2K by Iavarone *et al* clearly showing

the two gaps[27]. The result by Iavarone *et al* shown in Fig. 2.4 indicates $\Delta_\sigma = 7.1$ meV

and $\Delta_\pi = 2.3$ meV at 4.2K[16].
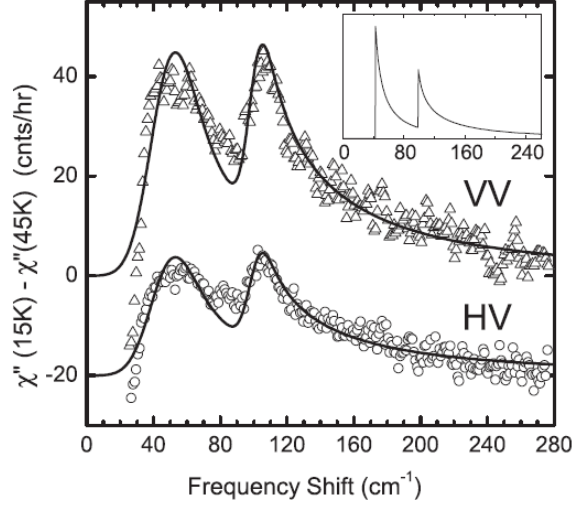
Figure 2.9 Electronic Raman spectra obtained by subtracting the 45K spectra from the 15K spectra. The thick solid lines are theoretical fits. The *HV* spectra are shifted for clarity. The inset is a calculated spectrum without Gaussian broadening[28].

Fig. 2.9 shows electronic Raman spectra, obtained by subtracting the spectra in the normal state from that in the superconducting state, from a polycrystalline MgB_2 sample by Chen *et al*[28]. Two peaks appear as a result of the superconducting transition at 50 and 105 cm^{-1}, which are the pair-breaking peaks corresponding to two binding energies of the Cooper pairs $2\Delta_\pi$ and $2\Delta_\sigma$[28]. The gap values thus obtained are $\Delta_\sigma = 7.1$ meV and $\Delta_\pi = 2.3$ meV.

Photoemission spectroscopy also provided evidence for the existence of two bands[29] and two gaps[30-32]. Fig. 2.10 (the inset shows details near E_F) shows photoemission spectra of MgB_2 measured in the superconducting and normal state by Tsuda *et al*[30]. Besides a peak around 7 meV and a shift of the leading edge, indicating the opening of a superconducting gap, a shoulder structure at 3.5 meV was observed. The

spectrum can only be fitted if two superconducting gaps, one at 1.7 meV (broken line) and the other at 5.6 meV (dotted line), are assumed. Later, the two gaps have been separately measured using angle-resolved photoemission spectroscopy (ARPES) [31, 32].
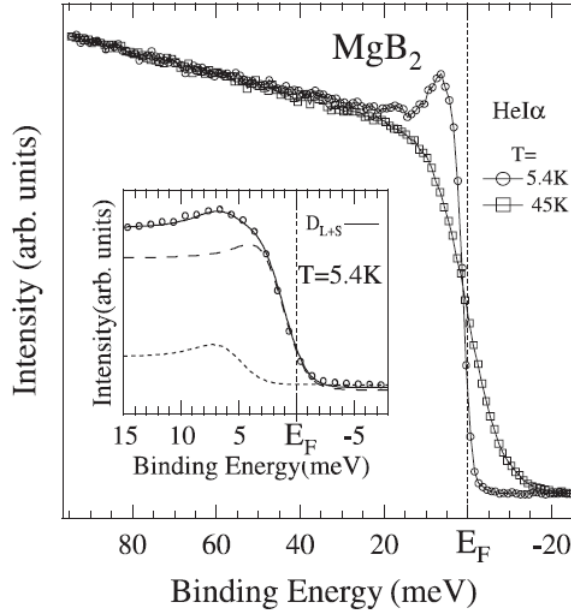
Figure 2.10 Photoemission spectra measured at 5.4 and 45 K. The inset shows the enlarged spectrum near E_F taken at 5.4 K, which can be fitted by assuming two gaps at 1.7 meV (broken line) and 5.6 meV (dotted line), respectively[30].

2.6   Upper critical field

For single-gap dirty limit superconductors, the upper critical field h $H_{c2}(0)=0.69T_c(dH_{c2}/dT)Tc$ and $(dH_{c2}/dT)_{Tc} \propto \rho_n$[33]; therefore H_{c2} increases with normal-state resistivity ρ_n, which can be achieved by adding impurities and defects into the superconductor. Gurevich pointed out that the two-band superconductor MgB$_2$ can be understood as a weakly-coupled bilayer in which two thin films corresponding to the σ and π bands are in contact through Josephson coupling[34] (see Fig. 2.11). Using the dirty-limit weak-coupling multi band BCS model taking into account both

20

interband and intraband scattering by nonmagnetic impurities, Gurevich showed that the temperature dependence of $H_{c2}(T)$ depends on whether the σ bands or π bands are dirtier and can be very different from that in the one-band theory[35]. As schematically shown in Fig. 2.11, the global $H_{c2}(T)$ of the bilayer is dominated by the layer with the higher H_{c2}. If the π layer is dirtier, it will have higher H_{c2} at low temperature even though its T_c is much lower. As a result, an upturn in the global $H_{c2}(T)$ occurs at low temperature. Because of the existence of two bands, $H_{c2}(0)$ in MgB_2 can exceed $0.69T_c(dH_{c2}/dT)T_c$ considerably.
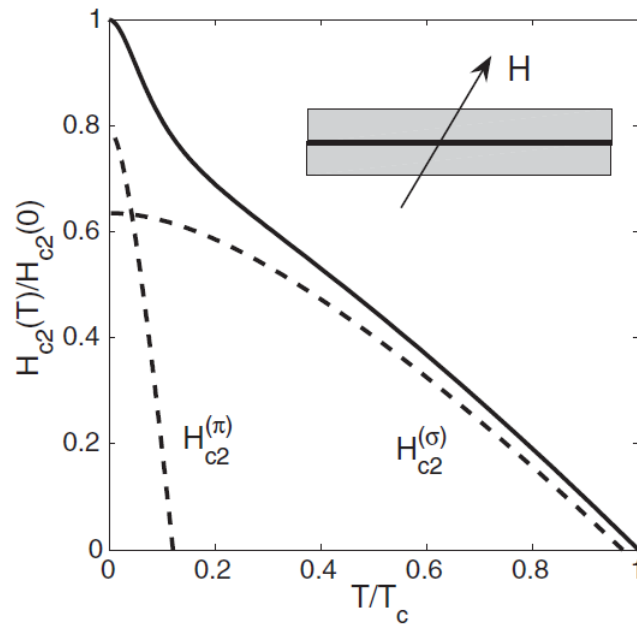
Figure 2.11 Temperature dependence of H_{c2} for the dirty two-gap superconductor MgB_2 illustrated by a bilayer toy model shown in the inset. The dashed curves are for σ and π films in the one-gap dirty limit. The solid curve shows $H_{c2}(T)$ calculated from the two-gap dirty-limit BCS theory[34].
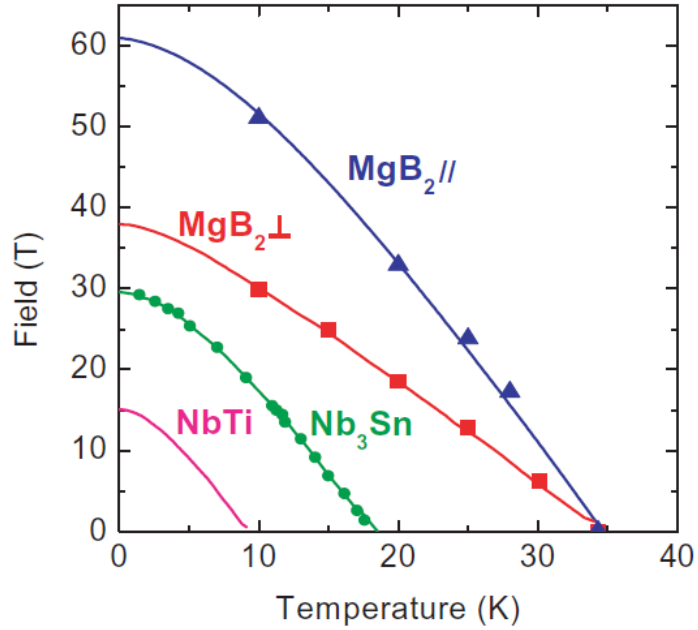
Figure 2.12 H_{c2} versus temperature plots for a carbon-alloyed HPCVD film, Nb–Ti (bulk) and Nb$_3$Sn (bulk). The triangle and square data are for the *ab* planes of MgB$_2$ parallel and normal to the field, respectively[2].

The H_{c2} behaviors described by Gurevich have been observed in experiment. For example, in thin films from various groups with disorder introduced in different ways, Braccini *et al* observed different types of temperature dependence of H_{c2}, including the anomalous upturn at low temperature, reflecting different multi band scattering in these samples[36]. The value of H_{c2} in carbon-doped thin films has reached over 60 T at low temperature (see Fig. 2.12), approaching the BCS paramagnetic limit of 65 T[36]. Considering the electron–phonon coupling effect, Gurevich argued that the strong coupling paramagnetic limit in MgB$_2$ can be as high as 130 T; thus there is still room for further enhancement of H_{c2} by engineering the σ- and π-band scattering[34]. The high H_{c2} in MgB$_2$ is very attractive for high-magnetic-field applications.

2.7   Hall effect and magnetoresistance

When the magnetic field is not so strong as to make the electron orbit quantization significant, the Hall effect and magnetoresistance in MgB_2 also demonstrate unique properties due to the existence of the multiple bands. Fig. 2.13 shows the Hall coefficient R_H measured with the magnetic field aligned either parallel to the *ab* plane or parallel to the *c* axis of MgB_2 single crystals by Eltsev *et al*[37]. They found that the in-plane $R_H(H\|c)$ is positive whereas the out-of-plane $R_H(H//ab)$ is negative. In materials with multiple bands, the sign of R_H is determined by a sum of $n_i\mu_i^2/q_i$ over all the bands, where *n* is the carrier density, μ is the mobility, *q* is the charge of the carrier, which is positive for holes and negative for electrons, and *i* represents different bands. When *H//c*, all the four bands shown in Fig. 2.14 contribute to the Hall field and the hole-like carriers dominate, thus $R_H>0$. However, when *H//ab*, the contributions of the two two-dimensional σ bands are substantially smaller due to their low mobilities, and the π-electron band dominates, thus $R_H < 0$[37]. The experiment is in agreement with band structure calculations[38].
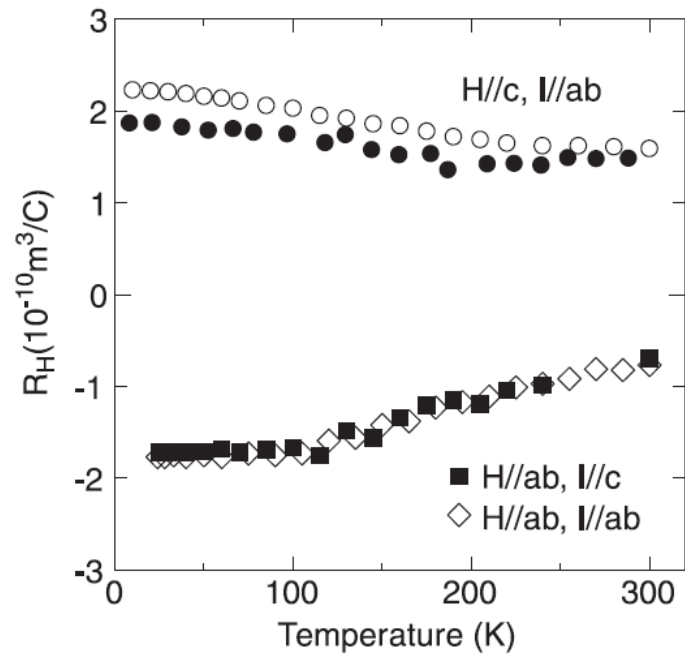
Figure 2.13 The in-plane ($H//c$) and out-of-plane ($H//ab$) Hall coefficients as a function of temperature in the normal state of MgB2 measured on several single crystals[37].
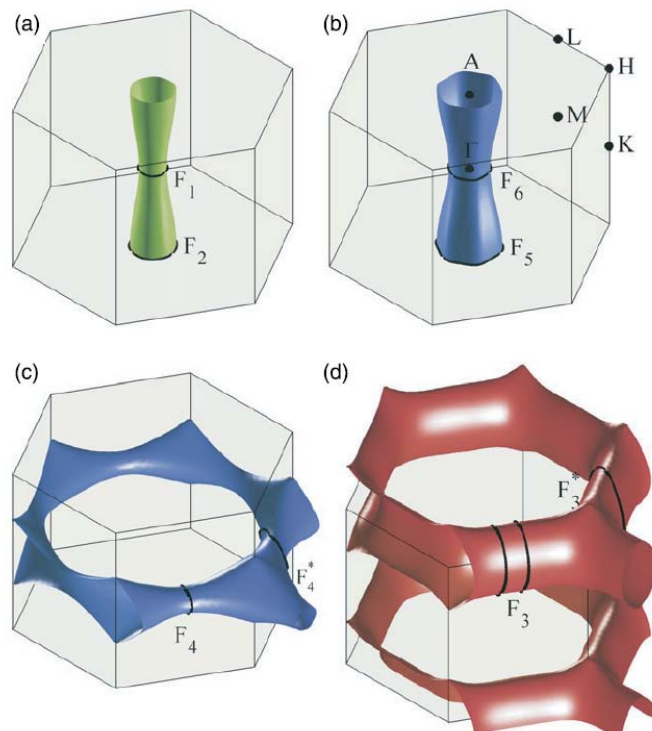
Figure 2.14 Fermi surface of MgB2 from band structure calculation plotted with the Γ point at the Brillouin zone center. Possible dHvA extremal orbits are indicated. (*a*) σ-light-hole band, (*b*) σ-heavy-hole band, (*c*) π-hole band and (*d*) π-electron band[39].

The existence of multiple bands in MgB_2, in particular when one π band is electron-like and the other three bands are hole-like, results in large magnetoresistance in clean MgB_2 samples[40-43]. At 18 T and 45 K, $\Delta\rho/\rho_0 = 130\%$ has been observed in an HPCVD film with $\rho_0=0.34$ $\mu\Omega$cm[43]. The magnetoresistance depends on a sum of $\sigma_i\sigma_j(\omega c_i\tau_i-\omega_{cj}\tau_j)^2$ over all the bands, where σ is the conductivity, ω_c is the cyclotron frequency $\omega_c \equiv qB/m^*$, which is positive for holes and negative for electrons, τ is the relaxation time and i and j represent different bands. The $\omega_{ci}\tau_i$ and $\omega_{cj}\tau_j$ terms add up when the i and j bands have different carriers and reduce each other when the carriers are of the same type.
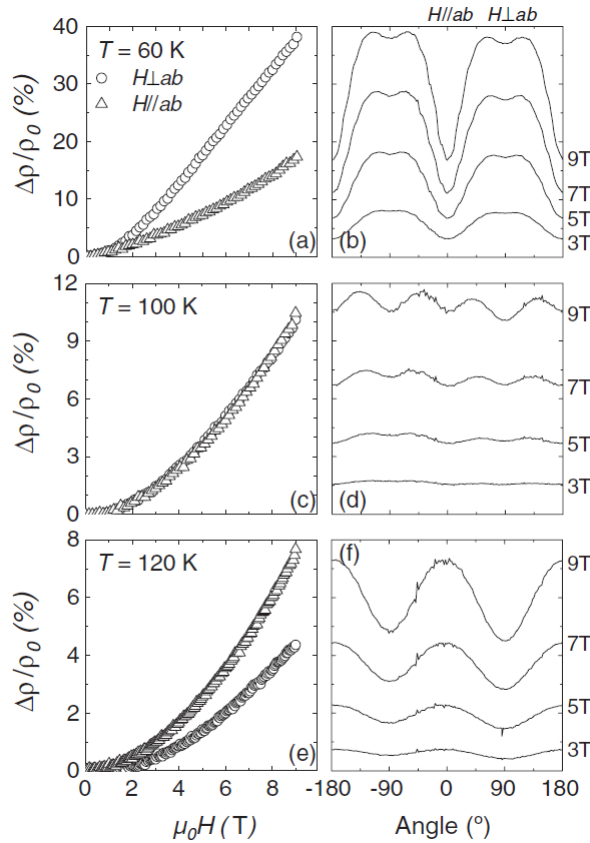
Figure 2.15 Magnetic field dependence ((a), (c) and (e)) and angular dependence ((b), (d) and (f)) of magnetoresistance of a MgB2 film. The results are for $T = 60$K ((a) and (b)), 100K ((c) and (d)) and 120K ((e) and (f)). A change in angular dependence is seen as the temperature is increased[43].

25

Li *et al* have shown that the magnetoresistance of MgB$_2$ has an angular dependence which changes dramatically with temperature[43]. In Fig. 2.15, the magnetic field dependence (left panels) and angular dependence (right panels) of the magnetoresistance for a MgB$_2$ film are shown for three temperatures. For $H \perp ab$, the magnetoresistance changes from a minimum at low temperature to a maximum at high temperature. The temperature-dependent anisotropy can be explained by the highly anisotropic Fermi surface of MgB$_2$ and different electron–phonon coupling from the different bands. When the applied field direction changes, the orbiting plane of the electron intercepts the Fermi surface at different angles. As a result, σ_i, ω_{ci} and τ_i of the four bands change, resulting in the angular dependence of the magnetoresistance. As the temperature increases, σ_i is reduced more rapidly for the σ bands than for the π bands due to the stronger electron–phonon interaction, and the contributions of the π bands become more important, leading to the observed changed in the angular dependence[43].
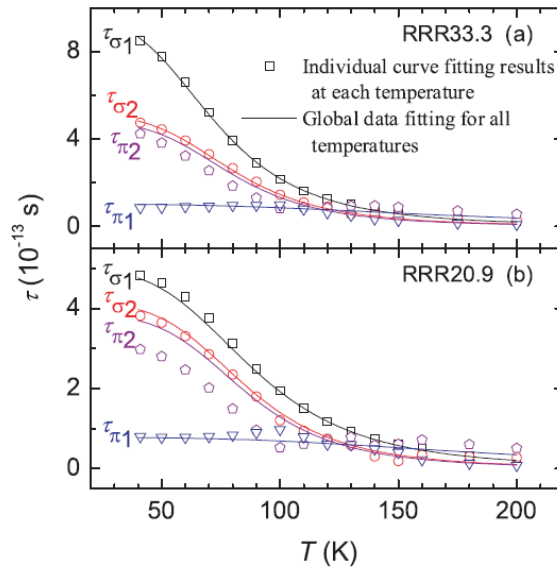
Figure 2.16 Temperature dependence of transport scattering times for the four bands for two MgB$_2$ films with RRR values of (*a*) 33.3 and (*b*) 20.9[44].

In combination with band structure calculations, efforts have been made to extract the scattering information for the different bands from the magnetotransport data[42, 44-47]. Fig. 2.16 shows the temperature dependence of electronic lifetimes for each of the four bands in two MgB$_2$ films with different RRR values, (*a*) 33.3 and (*b*) 20.9, obtained by Yang *et al* using both the magnetoresistance and the magnetic field dependence of the Hall coefficient[44]. In both films, the π_1 band is much dirtier than other bands at low temperatures, and the scattering rates become similar at high temperatures due to the electron–phonon scattering. Disorder, which reduces RRR, mainly enhances scattering in the cleaner bands. From the significant difference in the scattering rates in π_1 and π_2 bands, it is clear that the fully band-resolved information on the intraband scattering is important for a correct understanding of MgB$_2$.

2.8   Enhancement of H_{c2} and J_c by chemical doping

Consider the effect of the Lorentz force due to the transport current on the flux in a type II superconductor, electrical resistance associated with creep or flow will be induced and therefore causes the dissipation of energy. In order to make the type II superconductor carry a usefully high current in the presence of the strong penetrating field without dissipation of energy, "pinning force" need to be introduced and pins the vortices to fixed location in the materials. Pinning results from any spatial inhomogeneity of the material since local variations of ξ, λ or H_{c2} due to impurities, grain boundaries, voids, etc., will cause local variations of ε_1, the free energy per unit length of a flux line, causing some locations of the vortex to be favoured over others.

For prinstine MgB$_2$ superconductor, the J_c drops rapidly. The flux pinning was proved can be enhanced by traditional routes that has already been successfully

applied in the low- and high-temperature superconductors. Eom et al. employed the thin film deposition method which introduce the grain boundary pinning and improve the magnetic J_c at 4.2K above $10^5 Acm^{-2}$ at nearly 10T by alloying with oxygen, as shown in Fig. 3 (a)[48]. On the other hand, Bugoslavsky *et al*[49] use proton irradiation to induce crystalline disorder in bulk samples of MgB_2. Through this treatment, the reduction of J_c in magnetic field at 20K is much slower than in untreated samples as shown in Fig. 3(b), whereas the irreversibility field doubles on irradiation, about the same improvement observed by Eom.et al. in their thin films[48].

For industrial application, the thin film method and proton radiation method still cost too much. The alternative method is chemical doping, which is low cost but effective. Atomic substitution shifts the Fermi level and enhances impurity scattering, thus increasing the upper critical field, H_{c2}, and also introduces point defects which act as the pinning centers, therefore leading to the higher irreversibility field, H_{irr}, and critical current density, J_c, in field.

2.8.1 Carbon doping

Carbon doping is aimed at substitution of boron in MgB_2, and the $J_c(H)$ and H_{c2} of carbon-doped MgB_2 have been studied by several groups, all showing positive results. The substitution of carbon for boron has a great impact on the carrier density and impurity scattering, because MgB_2 is a two-gap superconductor. It is expected that the carbon, which has one more electron than boron, will donate electrons to the σ band. This would suggest that the superconductivity in MgB_2 is substantially modified by carbon doping. As a result, this opens up the possibility that maximum enhancement of the upper critical field, the irreversibility field, and the critical current density can be achieved by a controlled carbon doping.

From the applications point of view, the effect of C doping on the flux pinning properties is crucially important. The Soltanian *et al* firstly studied the carbon effect on $J_c(H)$ and H_{irr} in MgB_2[50]. They found that both the a-axis lattice parameter and the T_c decreased monotonically with increasing doping level (Fig. 2.18), with the T_c dropping only 2.7 K at the highest nominal composition of x = 0.4, for a sample sintered at 770°C for 30 min. In addition to the MgB_2 main phase, nano-size Mg_2C_3 and MgB_2C_2 particles were noticed in the XRD. The real doping level was substantially less than the nominal one, as evidenced by the impurity phases containing carbon. Nevertheless, the enhancement of $J_c(H)$ was not optimized, as the details of processing conditions were not studied, and magnetic J_c only reached 2×10^3 A/cm^2 at 5 K and 8 T for the x = 0.05 sample.
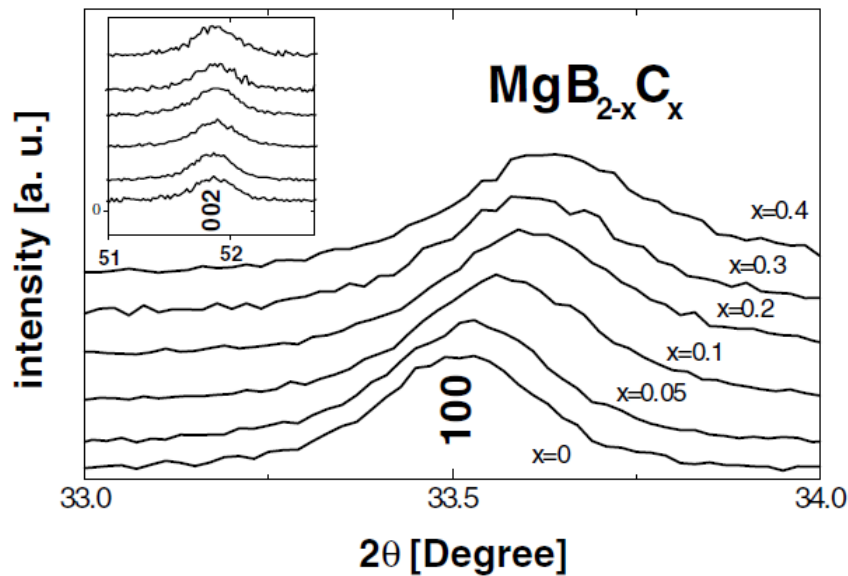
Figure 2.17 The (100) and (002) (inset) Bragg reflections for the $MgB_{2-x}C_x$ composition with x = 0, 0.05, 0.1, 0.2, 0.3, and 0.4. The results showed that carbon substitution only has an effect on the *a* lattice parameter[50].

Recently, the effects of C doping on the flux pinning and critical current density in MgB_2 were studied again using amorphous carbon in pellet and wire form[51]. Carbon substitution into boron sites was confirmed by the shrinkage of the lattice parameter

a with increasing C doping level. C substitution significantly enhanced both magnetic critical current density, $J_c(H)$, and transport critical current at high sintering temperatures, such as 900 $^{\circ}$C. Under the optimum conditions, transport J_c was enhanced by a factor of 5.7 at 12 T and 4.2 K as compared to the pure MgB$_2$ wire. Consequently, flux pinning was enhanced by the carbon substitution for boron with increasing processing temperature. A better enhancement of nano-C doping was also observed by Ma *et al*[52] for MgB$_2$ tapes. The transport J_c for the 5 at% C-doped tape reached 1.85×10^4 A/cm^2 at 10 T and 2.8×10^3 A/cm^2 at 14 T, respectively, both at 5 K. A significant enhancement of vortex pinning in the carbon-doped MgB$_2$ film has been reported by Pogrebnyakov *et al*[53], as shown in Fig. 2.18. TEM images showed that the doped films are textured, with columnar nanograins of Mg(B$_{1-x}$C$_x$)$_2$ and a preferential c-axis orientation[53]. Based on these results, nano-C is proposed to be one of the most promising dopants besides SiC for the enhancement of flux pinning for MgB$_2$ in high fields.
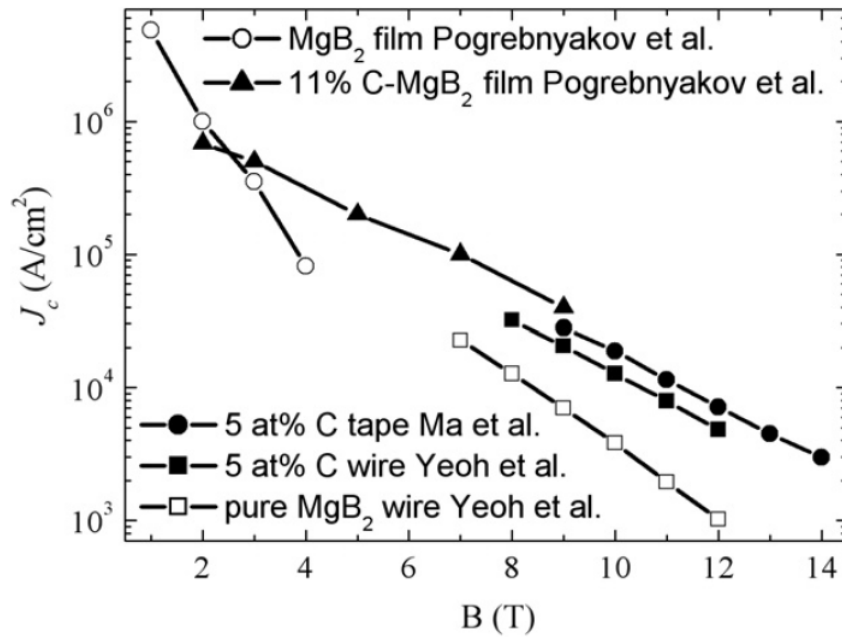
Figure 2.18 J_c–H curves at 4.2 K for pure and C-doped MgB$_2$ wire, tape, and film[54].

More encouraging results on carbon substitution on H_{c2} have been reported by several groups, all showing an enhancement of H_{c2} by carbon substitution, with a range of enhanced H_{c2} values from 25 to 40 T (at temperatures 4.2 K and below)[55-59]. The enhancement of H_{c2} is in agreement with the model of two-band impurity scattering of charge carriers as predicted in MgB$_2$, which indicates increased intraband scattering via shortening of the electron mean free path l[35]. As a consequence, ξ will be shortened according to the equation $1/\xi = 1/l + 1/\xi_0$[35], where ξ and l are the coherence length and mean free path, respectively.
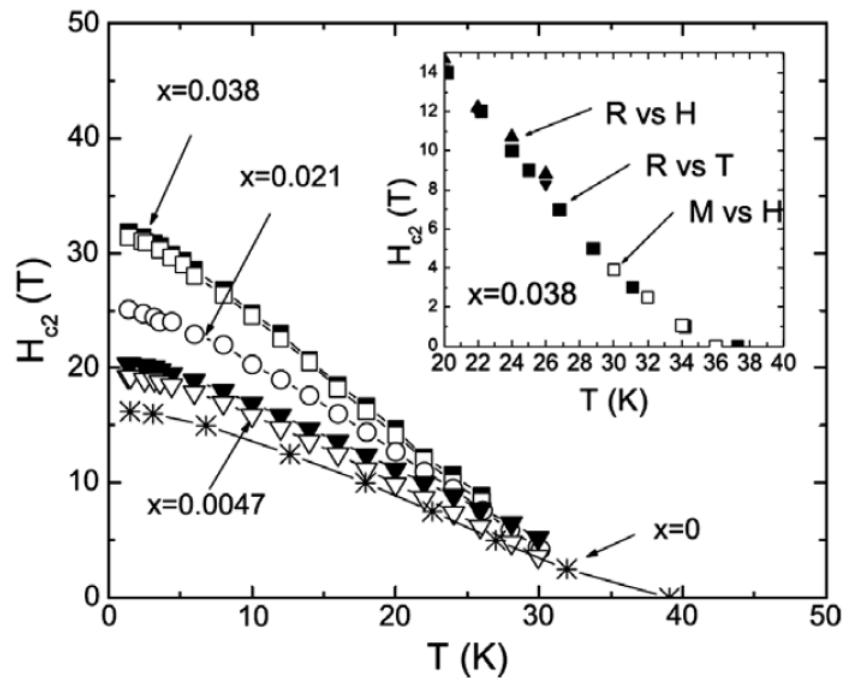
Figure 2.19 Superconducting upper critical field H$_{c2}$ as a function of temperature for Mg(B$_{1-x}$C$_x$)$_2$, x $\leq$ 0.038 samples. Inset: $H_{c2}(T)$ closer to T_c determined from temperature dependent resistivity (solid squares), field dependent resistivity (triangles), and field dependent magnetization (open squares)[60].

By using the chemical vapor deposition (CVD) method to co-deposit B together with elemental carbon, Wilke *et al* have successfully raised H_{c2} (T=0) for pure MgB$_2$ from 16.0 to 32.5 T in a carbon doped MgB$_2$ filament, with slight depression of T_c from 39.2 to 36.2 K for 3.8% C substitution, as shown in Fig. 2.19[60]. Later, Senkowicz et

al. proved that milling C with MgB_2 can produce H_{c2} (0 K) equal to that obtained for single crystals and CVD filaments. Bulk samples of milled carbon and MgB_2 powder subjected to hot isostatic pressing and Mg vapor produced an H_{c2} in excess of 32 T and Jc approaching 10^6 A/cm^{-2} for H = 0 T[61].

On the other hand, higher H_{c2} has been achieved in C alloyed thin films, which seems to be related to the expanded *c*-axis[61]. Record high values of $H_{c2} \parallel c$ at 4.2 K ($\approx$35 T) and $H_{c2} \parallel ab$ at 4.2 K ($\approx$51 T) were observed perpendicular and parallel to the *ab*-plane, respectively. Extrapolation of the experimental data to T = 0 suggests that $H_{c2} \parallel ab$ may approach the paramagnetic limit of $\approx$70 T[36]. Furthermore, H_{c2} with a value of 52–55 T was commonly observed for the carbon alloyed thin films at temperatures around 1.5–4.2 K[61, 62].

2.8.2   Nano-SiC doping

Due to the fact that MgB_2 has a relatively large coherence length, a stronger pinning force will be introduced when the dopant size is comparable to the coherence length[63]. A significant breakthrough in enhancing J_c was achieved using nanoscale SiC doping into MgB_2 by the University of Wollongong (UoW) group[64-66]. The 10 wt% nano-SiC-doped MgB2 bulk samples showed $H_{irr} \approx$ 8 T and $J_c \approx 10^5$ Acm^{-2} under 3 T at 20 K, with T_c reduction not pronounced, even in heavily doped samples with SiC up to 30%[64]. This group has demonstrated that C substitution for B resulted in a large number of intra-granular dislocations and dispersed nanosize impurities, which are both responsible for the significant enhancement in flux pinning[65, 66]. In a comparative study of a clean limit and Mg vapour-treated samples the UoW group has shown that there are two closely related but distinguishable mechanisms that

control the performance of $J_c(H):H_{c2}$ and flux pinning. Nano-SiC doping enhances both H_{c2} and flux pinning through multiple scattering channels[67]. The SiC-doped MgB$_2$ wires are even better than the thin film MgB$_2$, which had exhibited the strongest reported flux pinning and the highest J_c in high fields to date.
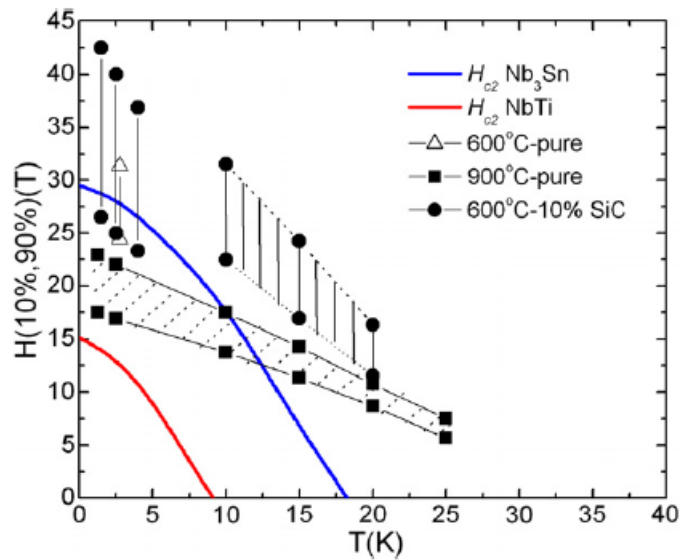
Figure 2.20 The H$_{c2}$ and H$_{irr}$ values of pure and SiC-added MgB2 sintered at 600 and 900 °C, respectively. The H$_{c2}$ and H$_{irr}$ values were obtained from the 10% and 90% normal state, respectively. The H$_{c2}$ values of Nb–Ti and Nb3Sn are also shown in the figure[68].

Inspired by the SiC doping, Xu et al. approached SiC doping by using polycarbosilane (PCS) as the SiC source[69]. PCS has been used widely as a precursor for the fabrication of SiC reinforced composite ceramics, as SiC nano-crystals can be synthesized by the pyrolysis of PCS. As with the SiC doping, the J_c values were enhanced significantly, and the $J_c(B)$ dependence was improved at low temperature and high magnetic fields. On the other hand, Wang et al. tried to reproduce the SiC result by using Si + C co-doping into MgB$_2$[70]. However, it was observed that the J_c values of the SiC-doped MgB$_2$ remained the best in comparison with those of the co-doping sample. The extent of enhancement of J_c and flux pinning of nano-SiC

33

doping can be explained by the dual reaction model, which will be discussed later in this work.

The Ohio State University has undertaken comprehensive studies of H_{c2} and H_{irr} with SiC addition in short and strand samples. An increase in H_{c2} from 20.5 T to more than 33 T and enhancement of H_{irr} from 16 T to a maximum of 28 T for an SiC doped sample was observed at 4.2 K[71]. More recently, a study by Matsumoto et al. showed that very high values of $H_{c2}(0)$ exceeding 40 T can be attained in SiC-doped bulk MgB_2 sintered at $600^{o}C$[68]. This result is considerably higher than in the C-doped single crystal[72], filament[60], or bulk samples[73]. What is more interesting is that the samples having the largest upper critical field showed a much broader transition of ΔH (10–90%), suggesting that significant inhomogeneity is introduced by alloying and by reaction at low temperature (see Fig. 2.16). This has important consequences for the application of MgB_2 wires and tapes for the cable and magnet industries, making them competitive with low T_c superconductors like NbTi and Nb_3Sn.
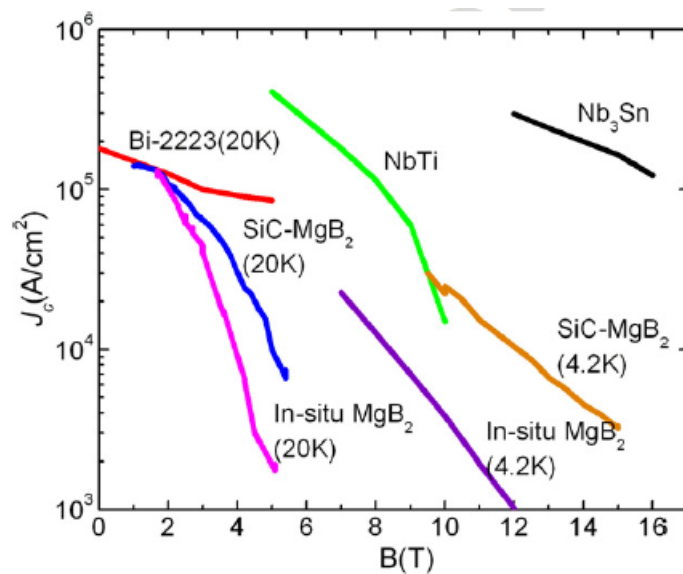
Figure 2.21 Comparison of J_c of MgB_2 with other commercial superconducting wire[54].

Fig. 2.21 shows the critical current density of MgB_2 in comparison to other commercial superconductor materials. It should be noted that the J_c of SiC-doped MgB_2 stands out very strongly even at 20 K in low field and that it is comparable to the value of Jc for Nb–Ti at 4.2 K, which is very useful for application of magnetic resonance imaging (MRI). At 20 K, the best J_c for the 10 wt% SiC doped sample was almost $10^5 A/cm^2$ at 3T, which is comparable with the J_c of state-of-the-art Ag/Bi-2223 tapes. These results indicate that powder-in-tube-processed MgB_2 wire is promising, not only for high-field applications, but also for applications at 20 K with a convenient cryocooler.

2.8.3   CNT doping

Among the various carbon precursors, carbon nanotubes (CNT) are particularly interesting, as their special geometry (high aspect ratio and nanometer diameter) may induce more effective pinning centers compared to other carbon-containing precursors. It has been demonstrated that CNTs can be embedded in Bi-2212, functioning like columnar defects, enhancing J_c in the Bi-based superconductor[74, 75]. A similar method has been reported by Yang et al. for a significant enhancement in J_c(H) in high temperature superconductors by introducing nanorods as columnar pinning centers into the superconductors[76].

Wei *et al* have studied the superconductivity of MgB_2- carbon multiwalled nanotube (MWCNT) composites[77]. However, the effects of multiwalled carbon nanotube doping on critical current density and flux pinning have not been reported. The authors' group have systematically investigated the doping effects of single-walled carbon nanotubes (SWCNTs) and multiwalled carbon nanotubes (MWCNTs) on the T_c, lattice parameters, $J_c(B)$, microstructure, and H_{c2} of MgB_2/Fe wire and bulk

samples[78-81]. Similarly to the C-doped MgB_2, the CNT doped samples only showed the optimum J_c at high sintering temperature ($\geq900^\text{o}\text{C}$) where the high processing temperature encourages better carbon substitution compared to low processing temperatures. The best performance in $J_c(B)$ was shown by SWCNT doping with sintering at 900^oC, and the $J_c(4.2\text{ K})$ reached the values of 50,955 and 3566 A/cm^2 at 7 and 12 T, respectively, as shown in Fig. 2.22. Yeoh et al. have showed that there is a correlation between the reactivity of the CNT and the amount of carbon substitution in the MgB_2, with the substitution of carbon for boron only occurring after the carbon atoms break free from the CNT[82].

However, longer CNTs tend to entangle and agglomerate, which results in inhomogeneous mixing of the CNTs with the precursor powder, blocking the current transport and suppressing the J_c[83]. Ultrasonication of CNT-doped MgB_2 was successfully introduced to improve the homogenous mixing of CNTs with the MgB_2 matrix, resulting in a significant enhancement in the field dependence of the critical current density, while avoiding the side-effects that would occur at higher processing temperatures[84].
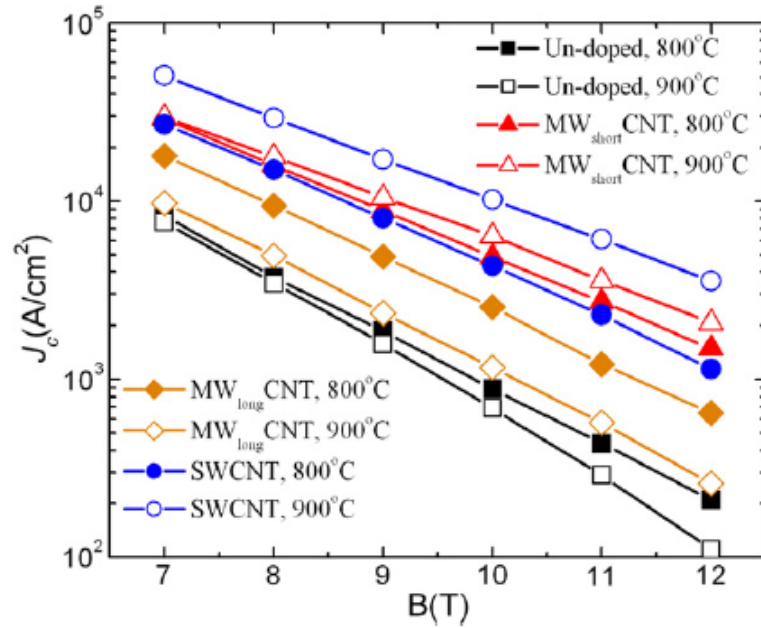
Figure 2.22 Transport critical current at 4.2 K at fields up to 12 T for nano-Cdoped and several CNT-doped wires produced at sintering temperatures of 800 and 900 °C. Pure MgB2 results are included for comparison[79].

It has been experimentally proved that the J_c of CNT doped samples is relatively insensitive to the heating rate in comparison to the un-doped and SiC-doped samples[85]. Dou et al. have pointed out that the CNT doping significantly improved heat transfer and dissipation during materials processing[86], due to the high thermal conductivity and stable electric conductivity of CNT[87, 88]. With the high axial strength and stiffness, approaching values for an ideal carbon fiber[89], CNT doping can improve the current path and connectivity between the grains in MgB_2.
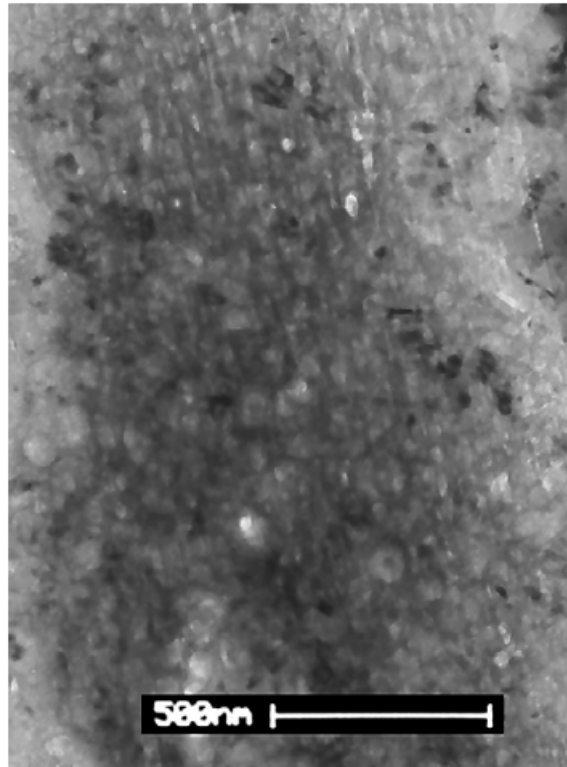
Figure 2.23 TEM image showing a number of straight CNTs embedded in MgB2. The elongated CNTs will improve the grain connectivity and act as efficient flux pinning sites[90].

To further advance the development of MgB_2, a method combining the advantages of magnetic field processing and CNT doping for processing MgB_2 superconductors has been demonstrated[90]. According to Dou *et al*, the unique magnetic field processing reduces the resistivity in CNT-doped MgB_2, straightens the entangled CNTs, and improves the adherence between the CNTs and the MgB_2 as shown in Fig. 2.23. H_{irr} for a 10 T field processed CNT doped sample reached 9 T at 20 K, which is close to the best value of SiC doped MgB_2 at 20 K.

2.8.4 Hydrocarbon and carbohydrate doping
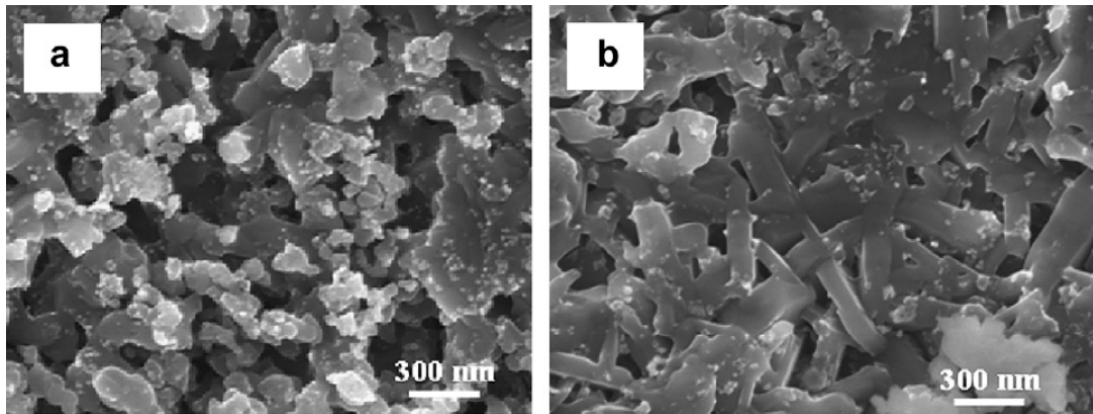
Figure 2.24 Photographs from field emission gun-scanning electron microscopy: (a) un-doped MgB_2, and (b) MgB_2 + 30 wt% $C_4H_6O_5$. As the doping level increases to 30 wt%, grains appear to have a bar/plate shape, with their width up to 150 nm and length up to 400 nm, in a well connected grain network[91].

In most experimental reports, the nano-dopants were introduced via solid state reaction, which is a dry mixing process. Alloying elements might not be distributed homogeneously, since defect energies are high, which could have important consequences for the observed superconducting properties. Recently, it has been demonstrated that hydrocarbon and carbohydrate dopings have advantages over other carbon dopants, resulting in J_c values almost comparable with those from the best SiC nano-powder doping[91-93]. Moreover, this approach provides additional benefits to the J_c(H) performance in low fields, that is, J_c at low fields does not degrade at certain doping levels as it does for any other C doping method. Due to the fact that most of the organic reagents decompose at temperatures below the formation temperature of MgB_2, highly reactive and fresh C on the atomic scale can be introduced, hence the C substitution for B can take place at as low a temperature as the formation temperature of MgB_2. Micro-structural analyses suggest that J_c enhancement is due to the substitution of carbon for boron in MgB_2, liquid

homogenous mixing, and a smaller MgB_2 grain size due to the low processing temperature, as shown in Fig. 2.24.

2.8.5 Graphene and graphene oxide doping

Graphene is a two-dimensional (2D) atomic crystal which consists of carbon atoms arranged in a hexagonal lattice (Fig. 1.25). Its single-layered honeycomb structure makes it the "mother" of all carbon-based systems: the graphite we find in our pencils is simply a stack of graphene layers; carbon nanotubes are made of rolledup sheets of graphene; and buckminsterfullerene molecules, or "buckyballs", are nanometre-size spheres of wrapped-up graphene (Fig. 1.25)[94]. These forms of carbon were isolated long before graphene and have been used in many applications, but their electric, magnetic and elastic properties all originate in the properties of graphene[94].
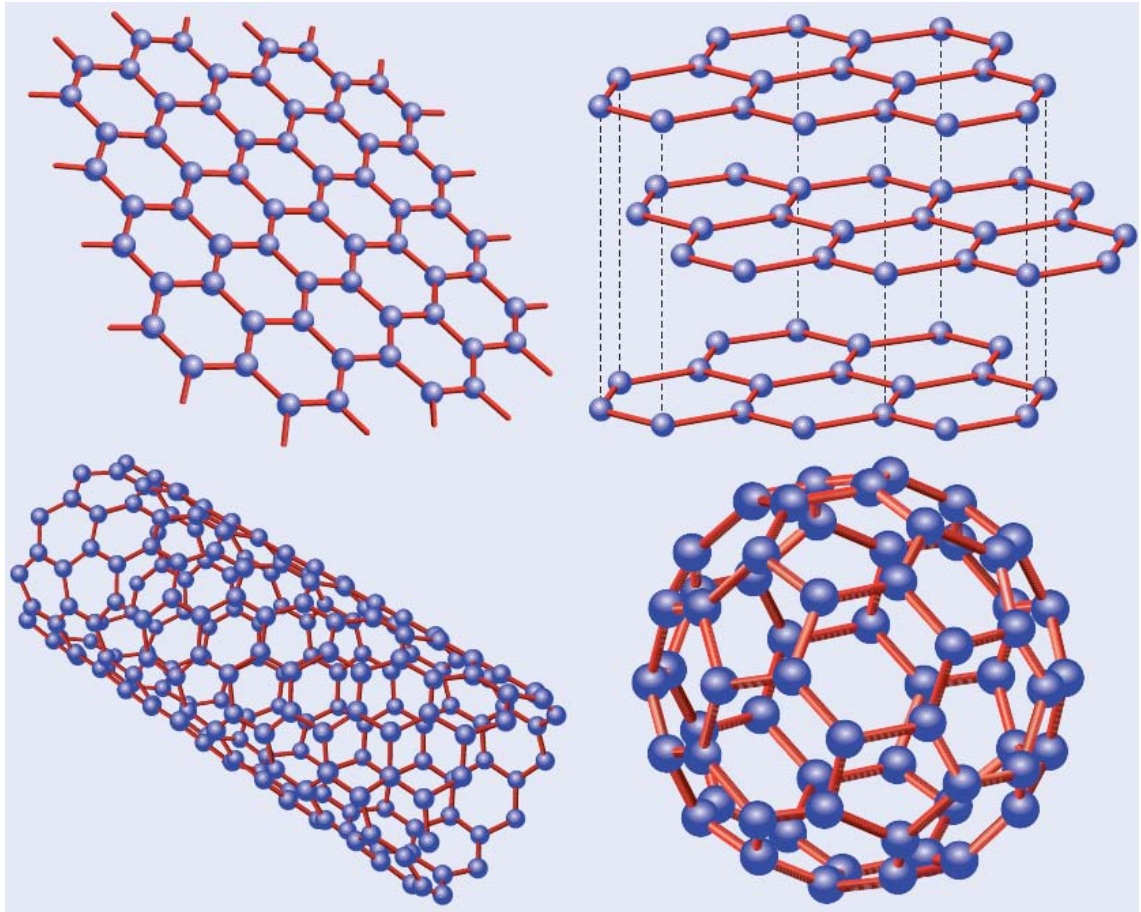
Figure 2.25 Graphene (top left) consists of a 2D hexagonal lattice of carbon atoms. Each atom is covalently bonded to three others; but since carbon has four valence electrons, one is left free – allowing graphene to conduct electricity. Other well-known forms of carbon all derive from graphene: graphite is a stack of graphene layers (top right); carbon nanotubes are rolled-up cylinders of graphene (bottom left); and a buckminsterfullerene (C60) molecule consists of graphene balled into a sphere by introducing some pentagons as well as hexagons into the lattice (bottom right)[94].

As a conductor of electricity it has extremely electrical conductivity[95]. As a conductor of heat it also has superior thermal conductivity and outperforms all other known materials[96]. Graphene is an ideal candidate for use as a reinforcement in high performance composites, because it is the strongest and simultaneously one of the stiffest known materials, with a Young's modulus of 1 TPa[97]. Since it is nano-sizedd, extremely electrically and thermally conductive and strongest and stiffest materials

41

graphene is suitable for being added into MgB_2, to improve the flux pinning, grain connectivity, mechanical property and heat transfer performance, respectively. Its negative thermal expansion coefficient can also benefit the strain flux pinning for MgB_2.
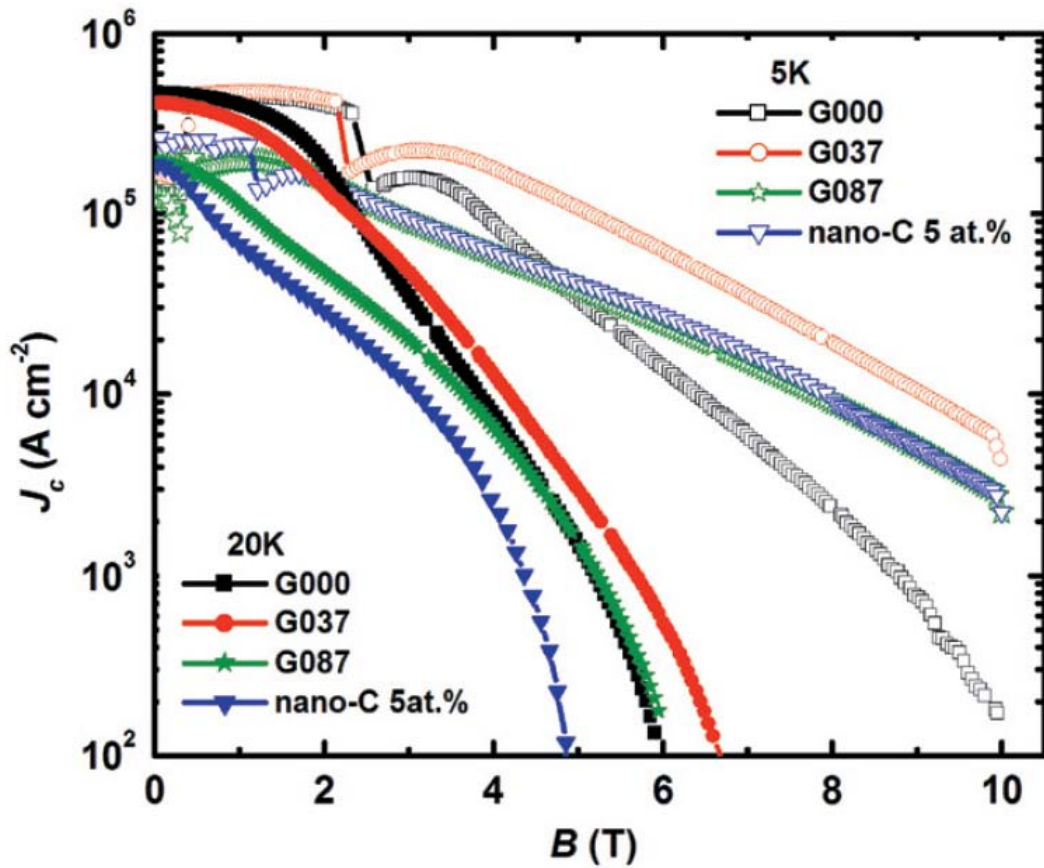
Figure 2.26 Critical current density as a function of magnetic field at 5 and 20 K for with and without graphene doped bulk samples. 5 at.% nano-C doped sample for a comparable result at the same sample preparation route[98].

Such a excellent new materials also attracted the people in superconducting research area, Xu *et al* [98] first studied graphene doped MgB_2 and J_c was enhanced by an order of magnitude at 8 T and 5 K as shwon Fig. 2.25. The strong pinning enhancement was argued to be attributed to a combination of C substitution and thermal strain

induced defects. Later, Silva *et al* found the graphene found the low field J_c was also improved by graphene doping as shown in Fig. 1.26[99] and Fig. 1.27[100]. However, the high field J_c is not comparative with nano-SiC doped.
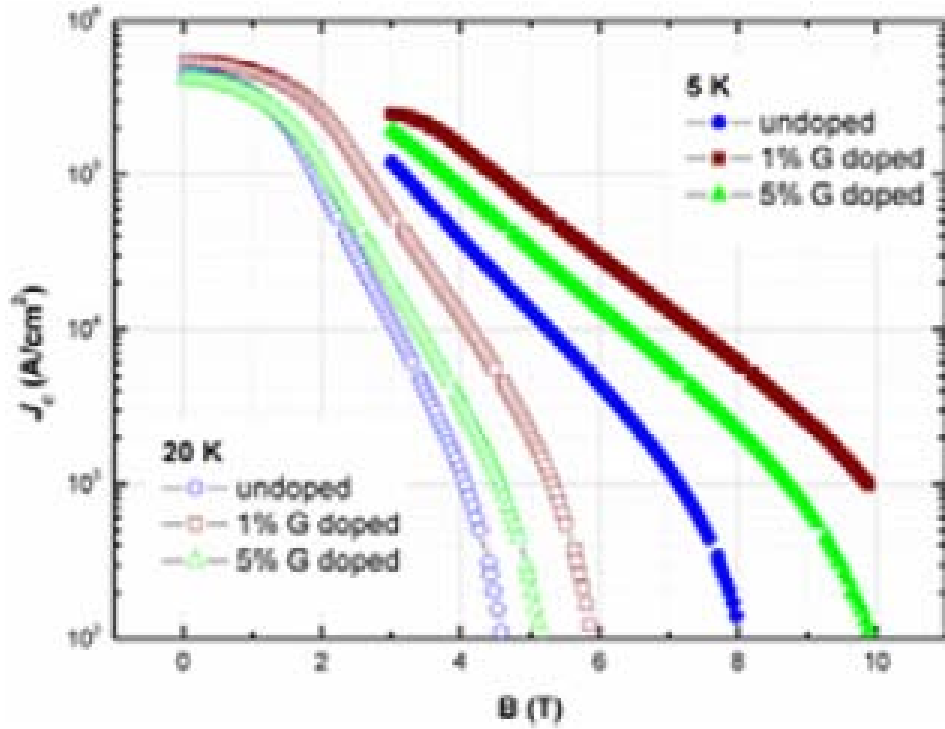
Figure 2.27 Variation of the critical current density with applied magnetic field for undoped and graphene doped MgB$_2$ bulk samples[99].
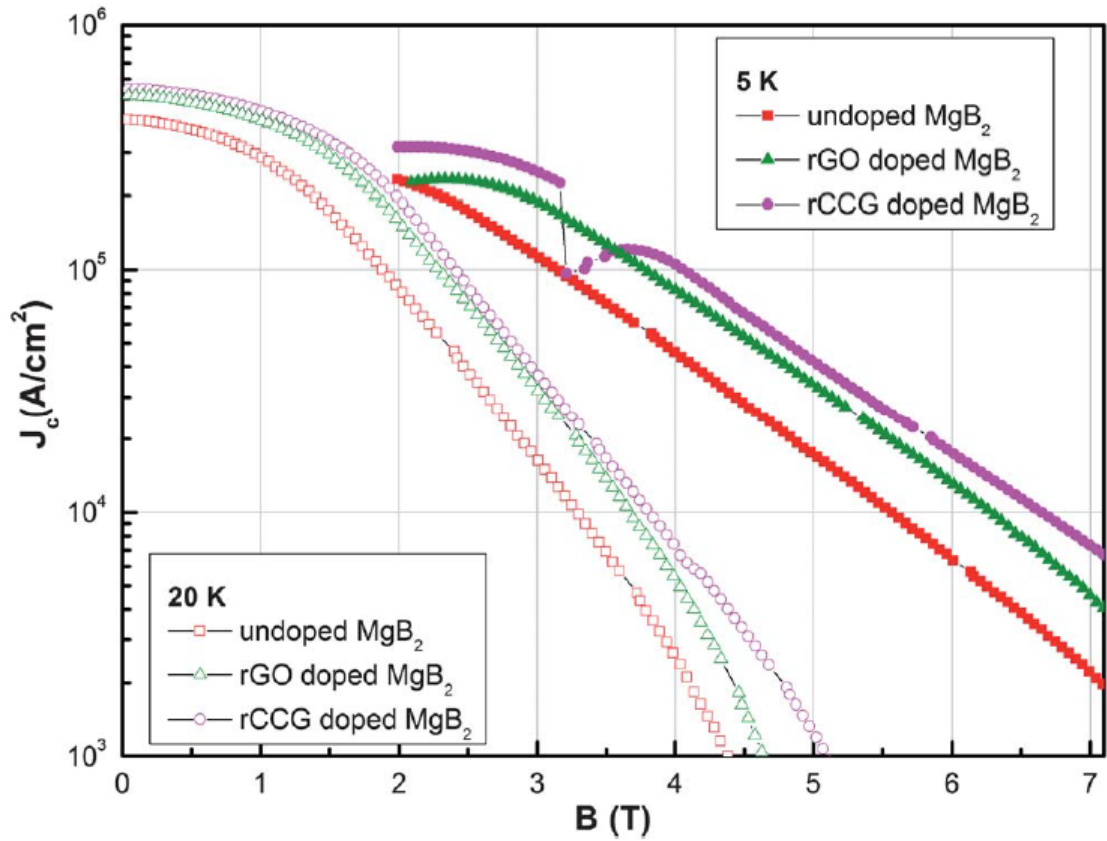
Figure 2.28 In-field Jc performance of undoped, rGO- and rCCG-doped MgB2 bulk samples[100].

Recently, Silva *et al* also found the graphene oxide could also improve the overall field J_c and the high field J_c is better than graphene doped MgB_2. Graphene oxide is also single layer sheet (as shown in Fig.1.29[101]) which is exfoliated in water from strongly oxygenated and highly hydrophilic layered graphite oxide[102-104]. It can be produced considerable quantities relies on the chemical conversion of graphite to graphite oxide[102, 103, 105-107], This provides a very convenient setting for the implementation of solution-phase techniques toward the conversion of graphene oxide back to graphene by way of chemical reduction[104, 106] or the processing of the graphene oxide sheets into films and paperlike materials[106-108]. And the graphene oxide dispersion could be prepared in the organic solvents[109-111] which provide an approach for uniform mixture of GO with boron powder.
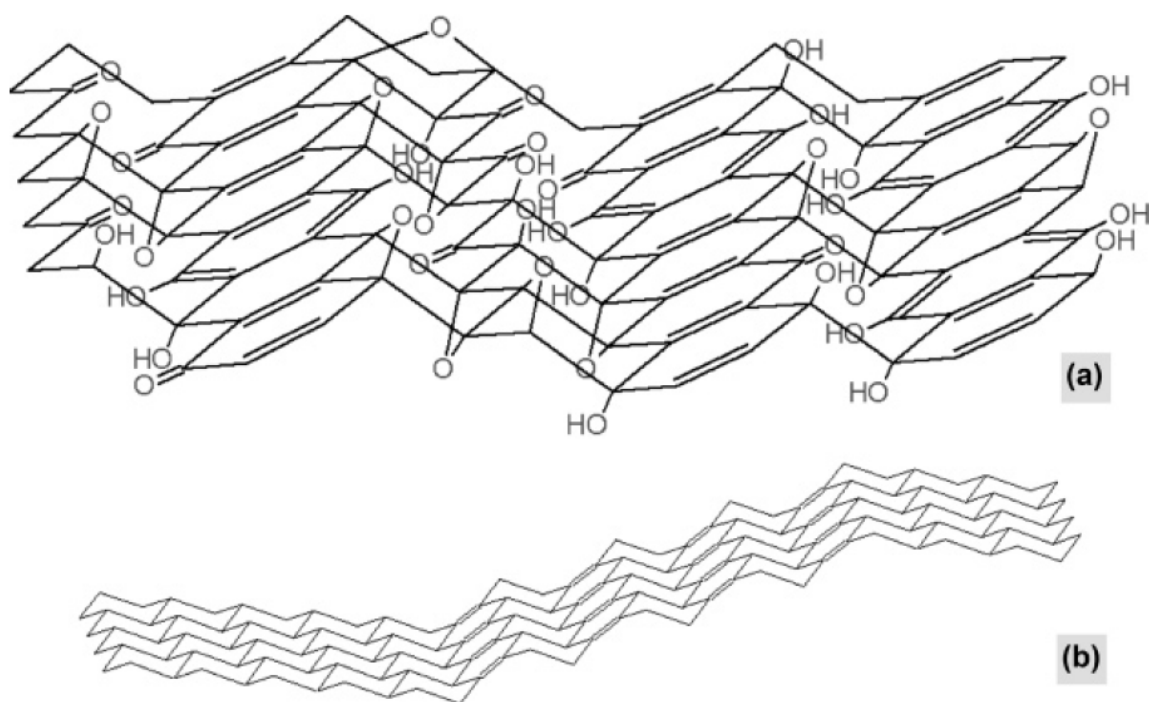
Figure 2.29 Scheme of new structure model of GO: (a) Surface Species and (b) Folded Carbon Skeleton

2.9 Summary

This chapter reviews the basic properties of MgB_2 including its crystal structure, electronic structure and superconducting properties, and it also reviews various methods of chemical doping to enhance the H_{c2} and J_c. This chapter is important and elemental for this thesis because the knowledge of basic properties of MgB_2 is helpful, it could not only associate MgB_2 with conventional superconductors and high temperature superconductors but also help us understand the unique feature of MgB_2; and the review of chemical doping paves the way for discovering the new dopants to further enhance the H_{c2} and J_c.

2.10 References

1.   J. Nagamatsu, N. Nakagawa, T. Muranaka, Y. Zenitani and J. Akimitsu, Nature **410** (6824), 63-64 (2001).

2.   X. X. Xi, Reports on Progress in Physics **71** (11), 116501 (2008).

3. J. M. An and W. E. Pickett, Physical Review Letters **86** (19), 4366-4369 (2001).

4. J. Kortus, I. I. Mazin, K. D. Belashchenko, V. P. Antropov and L. L. Boyer, Physical Review Letters **86** (20), 4656-4659 (2001).

5. H. J. Choi, D. Roundy, H. Sun, M. L. Cohen and S. G. Louie, Nature **418** (6899), 758-760 (2002).

6. I. I. Mazin and V. P. Antropov, Physica C: Superconductivity **385** (1–2), 49-65 (2003).

7. A. A. Golubov, J. Kortus, O. V. Dolgov, O. Jepsen, Y. Kong, O. K. Andersen, B. J. Gibson, K. Ahn and R. K. Kremer, Journal of Physics: Condensed Matter **14** (6), 1353 (2002).

8. I. I. Mazin, O. K. Andersen, O. Jepsen, O. V. Dolgov, J. Kortus, A. A. Golubov, A. B. Kuz'menko and D. van der Marel, Physical Review Letters **89** (10), 107002 (2002).

9. K. P. Bohnen, R. Heid and B. Renker, Physical Review Letters **86** (25), 5771-5774 (2001).

10. T. Yildirim, O. Gülseren, J. W. Lynn, C. M. Brown, T. J. Udovic, Q. Huang, N. Rogado, K. A. Regan, M. A. Hayward, J. S. Slusky, T. He, M. K. Haas, P. Khalifah, K. Inumaru and R. J. Cava, Physical Review Letters **87** (3), 037001 (2001).

11. A. Y. Liu, I. I. Mazin and J. Kortus, Physical Review Letters **87** (8), 087005 (2001).

12. H. J. Choi, D. Roundy, H. Sun, M. L. Cohen and S. G. Louie, Physical Review B **66** (2), 020513 (2002).

13. M. Calandra, M. Lazzeri and F. Mauri, Physica C: Superconductivity **456** (1–2), 38-44 (2007).

14. A. Floris, A. Sanna, M. Lüders, G. Profeta, N. N. Lathiotakis, M. A. L. Marques, C. Franchini, E. K. U. Gross, A. Continenza and S. Massidda, Physica C: Superconductivity **456** (1–2), 45-53 (2007).

15. J. Geerk, R. Schneider, G. Linker, A. G. Zaitsev, R. Heid, K. P. Bohnen and H. v. Löhneysen, Physical Review Letters **94** (22), 227005 (2005).

16. M. Iavarone, G. Karapetrov, A. E. Koshelev, W. K. Kwok, G. W. Crabtree, D. G. Hinks, W. N. Kang, E.-M. Choi, H. J. Kim, H.-J. Kim and S. I. Lee, Physical Review Letters **89** (18), 187002 (2002).

17. W. Pickett, Nature **418** (6899), 733-734 (2002).

18. Y. Wang, T. Plackowski and A. Junod, Physica C: Superconductivity **355** (3–4), 179-193 (2001).

19. F. Bouquet, R. A. Fisher, N. E. Phillips, D. G. Hinks and J. D. Jorgensen, Physical Review Letters **87** (4), 047001 (2001).

20. H. D. Yang, J. Y. Lin, H. H. Li, F. H. Hsu, C. J. Liu, S. C. Li, R. C. Yu and C. Q. Jin, Physical Review Letters **87** (16), 167003 (2001).

21. P. Szabó, P. Samuely, J. Kačmarčík, T. Klein, J. Marcus, D. Fruchart, S. Miraglia, C. Marcenat and A. G. M. Jansen, Physical Review Letters **87** (13), 137005 (2001).

22. H. Schmidt, J. F. Zasadzinski, K. E. Gray and D. G. Hinks, Physical Review Letters **88** (12), 127002 (2002).

23. R. S. Gonnelli, D. Daghero, G. A. Ummarino, V. A. Stepanov, J. Jun, S. M. Kazakov and J. Karpinski, Physical Review Letters **89** (24), 247004 (2002).

24. W. K. Park and L. H. Greene, Review of Scientific Instruments **77** (2), 023905-023906 (2006).

25. F. Giubileo, D. Roditchev, W. Sacks, R. Lamy, D. X. Thanh, J. Klein, S. Miraglia, D. Fruchart, J. Marcus and P. Monod, Physical Review Letters **87** (17), 177008 (2001).

26. M. R. Eskildsen, M. Kugler, S. Tanaka, J. Jun, S. M. Kazakov, J. Karpinski and Ø. Fischer, Physical Review Letters **89** (18), 187003 (2002).

27. M. Iavarone, G. Karapetrov, A. Menzel, V. Komanicky, H. You, W. K. Kwok, P. Orgiani, V. Ferrando and X. X. Xi, Applied Physics Letters **87** (24), 242506-242503 (2005).

28. X. K. Chen, M. J. Konstantinović, J. C. Irwin, D. D. Lawrie and J. P. Franck, Physical Review Letters **87** (15), 157002 (2001).

29. H. Uchiyama, K. M. Shen, S. Lee, A. Damascelli, D. H. Lu, D. L. Feng, Z. X. Shen and S. Tajima, Physical Review Letters **88** (15), 157002 (2002).

30. S. Tsuda, T. Yokoya, T. Kiss, Y. Takano, K. Togano, H. Kito, H. Ihara and S. Shin, Physical Review Letters **87** (17), 177006 (2001).

31. S. Souma, Y. Machida, T. Sato, T. Takahashi, H. Matsui, S. C. Wang, H. Ding, A. Kaminski, J. C. Campuzano, S. Sasaki and K. Kadowaki, Nature **423** (6935), 65-67 (2003).

32. S. Tsuda, T. Yokoya, Y. Takano, H. Kito, A. Matsushita, F. Yin, J. Itoh, H. Harima and S. Shin, Physical Review Letters **91** (12), 127001 (2003).

33. N. R. Werthamer, E. Helfand and P. C. Hohenberg, Physical Review **147** (1), 295-302 (1966).

34. A. Gurevich, Physica C: Superconductivity **456** (1–2), 160-169 (2007).

35. A. Gurevich, Physical Review B **67** (18), 184515 (2003).

36. V. Braccini, A. Gurevich, J. E. Giencke, M. C. Jewell, C. B. Eom, D. C. Larbalestier, A. Pogrebnyakov, Y. Cui, B. T. Liu, Y. F. Hu, J. M. Redwing, Q. Li, X. X. Xi, R. K. Singh, R. Gandikota, J. Kim, B. Wilkens, N. Newman, J. Rowell, B. Moeckly, V. Ferrando, C. Tarantini, D. Marré, M. Putti, C. Ferdeghini, R. Vaglio and E. Haanappel, Physical Review B **71** (1), 012504 (2005).

37.   Y. Eltsev, K. Nakao, S. Lee, T. Masui, N. Chikumoto, S. Tajima, N. Koshizuka and M. Murakami, Physical Review B **66** (18), 180504 (2002).

38.   G. Satta, G. Profeta, F. Bernardini, A. Continenza and S. Massidda, Physical Review B **64** (10), 104507 (2001).

39.   A. Carrington, E. A. Yelland, J. D. Fletcher and J. R. Cooper, Physica C: Superconductivity **456** (1–2), 92-101 (2007).

40.   D. K. Finnemore, J. E. Ostenson, S. L. Bud'ko, G. Lapertot and P. C. Canfield, Physical Review Letters **86** (11), 2420-2422 (2001).

41.   S. L. Bud'ko, C. Petrovic, G. Lapertot, C. E. Cunningham, P. C. Canfield, M. H. Jung and A. H. Lacerda, Physical Review B **63** (22), 220503 (2001).

42.   I. Pallecchi, V. Braccini, E. Galleani d'Agliano, M. Monni, A. S. Siri, P. Manfrinetti, A. Palenzona and M. Putti, Physical Review B **71** (10), 104519 (2005).

43.   Q. Li, B. T. Liu, Y. F. Hu, J. Chen, H. Gao, L. Shan, H. H. Wen, A. V. Pogrebnyakov, J. M. Redwing and X. X. Xi, Physical Review Letters **96** (16), 167003 (2006).

44.   H. Yang, Y. Liu, C. Zhuang, J. Shi, Y. Yao, S. Massidda, M. Monni, Y. Jia, X. Xi, Q. Li, Z.-K. Liu, Q. Feng and H.-H. Wen, Physical Review Letters **101** (6), 067001 (2008).

45.   I. Pallecchi, V. Ferrando, E. G. D'Agliano, D. Marré, M. Monni, M. Putti, C. Tarantini, F. Gatti, H. U. Aebersold, E. Lehmann, X. X. Xi, E. G. Haanappel and C. Ferdeghini, Physical Review B **72** (18), 184512 (2005).

46.   I. Pallecchi, M. Monni, C. Ferdeghini, V. Ferrando, M. Putti, C. Tarantini and E. Galleani D'Agliano, Eur. Phys. J. B **52** (2), 171-179 (2006).

47.   M. Monni, I. Pallecchi, C. Ferdeghini, V. Ferrando, A. Floris, E. Galleani d'Agliano, E. Lehmann, I. Sheikin, C. Tarantini, X. Xi, X., S. Massidda and M. Putti, EPL **81** (6), 67006 (2008).

48. C. B. Eom, M. K. Lee, J. H. Choi, L. J. Belenky, X. Song, L. D. Cooley, M. T. Naus, S. Patnaik, J. Jiang, M. Rikel, A. Polyanskii, A. Gurevich, X. Y. Cai, S. D. Bu, S. E. Babcock, E. E. Hellstrom, D. C. Larbalestier, N. Rogado, K. A. Regan, M. A. Hayward, T. He, J. S. Slusky, K. Inumaru, M. K. Haas and R. J. Cava, Nature **411** (6837), 558-560 (2001).

49. Y. Bugoslavsky, L. F. Cohen, G. K. Perkins, M. Polichetti, T. J. Tate, R. Gwilliam and A. D. Caplin, Nature **411** (6837), 561-563 (2001).

50. S. Soltanian, J. Horvat, X. L. Wang, P. Munroe and S. X. Dou, Physica C: Superconductivity **390** (3), 185-190 (2003).

51. W. K. Yeoh, J. H. Kim, J. Horvat, X. Xu, M. J. Qin, S. X. Dou, C. H. Jiang, T. Nakane, H. Kumakura and P. Munroe, Superconductor Science and Technology **19** (6), 596 (2006).

52. Y. Ma, X. Zhang, G. Nishijima, K. Watanabe, S. Awaji and X. Bai, Applied Physics Letters **88** (7), 072502-072503 (2006).

53. A. V. Pogrebnyakov, X. X. Xi, J. M. Redwing, V. Vaithyanathan, D. G. Schlom, A. Soukiassian, S. B. Mi, C. L. Jia, J. E. Giencke, C. B. Eom, J. Chen, Y. F. Hu, Y. Cui and Q. Li, Applied Physics Letters **85** (11), 2017-2019 (2004).

54. W. K. Yeoh and S. X. Dou, Physica C: Superconductivity **456** (1–2), 170-179 (2007).

55. T. Masui, S. Lee and S. Tajima, Physical Review B **70** (2), 024504 (2004).

56. E. Ohmichi, E. Komatsu, T. Masui, S. Lee, S. Tajima and T. Osada, Physical Review B **70** (17), 174513 (2004).

57. Z. Hol'anová, Kačmar̆, amp, x, J. k, P. Szabó, P. Samuely, I. Sheikin, R. A. Ribeiro, S. L. Bud'ko and P. C. Canfield, Physica C: Superconductivity **404** (1–4), 195-199 (2004).

58. M. Putti, V. Braccini, C. Ferdeghini, I. Pallecchi, A. S. Siri, F. Gatti, P. Manfrinetti and A. Palenzona, Physical Review B **70** (5), 052509 (2004).

59. P. Samuely, Z. Hoľanová, P. Szabó, H. T. Wilke, S. L. Bud'ko and P. C. Canfield, physica status solidi (c) **2** (5), 1743-1748 (2005).

60. R. H. T. Wilke, S. L. Bud'ko, P. C. Canfield, D. K. Finnemore, R. J. Suplinskas and S. T. Hannahs, Physical Review Letters **92** (21), 217003 (2004).

61. C. Ferdeghini, V. Ferrando, C. Tarantini, E. Bellingeri, G. Grasso, A. Malagoli, D. Marre, M. Putti, P. Manfrinetti, A. Pogrebnyakov, J. M. Redwing, X. X. Xi, R. Felici and E. Haanappel, Applied Superconductivity, IEEE Transactions on **15** (2), 3234-3237 (2005).

62. V. Ferrando, P. Orgiani, A. V. Pogrebnyakov, J. Chen, Q. Li, J. M. Redwing, X. X. Xi, J. E. Giencke, C.-B. Eom, Q.-R. Feng, J. B. Betts and C. H. Mielke, Applied Physics Letters **87** (25), 252509-252503 (2005).

63. S. Soltanian, X. Wang, J. Horvat, Q. Mengjun, L. Huakun, P. R. Munroe and S. X. Dou, Applied Superconductivity, IEEE Transactions on **13** (2), 3273-3276 (2003).

64. S. X. Dou, S. Soltanian, J. Horvat, X. L. Wang, S. H. Zhou, M. Ionescu, H. K. Liu, P. Munroe and M. Tomsic, Applied Physics Letters **81** (18), 3419-3421 (2002).

65. S. X. Dou, A. V. Pan, S. Zhou, M. Ionescu, H. K. Liu and P. R. Munroe, Superconductor Science and Technology **15** (11), 1587 (2002).

66. S. X. Dou, A. V. Pan, S. Zhou, M. Ionescu, X. L. Wang, J. Horvat, H. K. Liu and P. R. Munroe, Journal of Applied Physics **94** (3), 1850-1856 (2003).

67. S. X. Dou, V. Braccini, S. Soltanian, R. Klie, Y. Zhu, S. Li, X. L. Wang and D. Larbalestier, Journal of Applied Physics **96** (12), 7549-7555 (2004).

68. A. Matsumoto, H. Kumakura, H. Kitaguchi, B. J. Senkowicz, M. C. Jewell, E. E. Hellstrom, Y. Zhu, P. M. Voyles and D. C. Larbalestier, Applied Physics Letters **89** (13), 132508-132503 (2006).

69.	H. L. Xu, Y. Feng, Y. Zhao, Y. D. Xu, X. J. Wu, M. H. Pu, G. Yan, Y. F. Lu, C. S. Li, P. Ji, Z. H. Shen and Z. Xu, Superconductor Science and Technology **19** (1), 68 (2006).

70.	X. L. Wang, S. Soltanian, M. James, M. J. Qin, J. Horvat, Q. W. Yao, H. K. Liu and S. X. Dou, Physica C: Superconductivity **408–410** (0), 63-67 (2004).

71.	M. Bhatia, M. D. Sumption and E. W. Collings, Applied Superconductivity, IEEE Transactions on **15** (2), 3204-3206 (2005).

72.	S. M. Kazakov, R. Puzniak, K. Rogacki, A. V. Mironov, N. D. Zhigadlo, J. Jun, C. Soltmann, B. Batlogg and J. Karpinski, Physical Review B **71** (2), 024533 (2005).

73.	B. J. Senkowicz, J. E. Giencke, S. Patnaik, C. B. Eom, E. E. Hellstrom and D. C. Larbalestier, Applied Physics Letters **86** (20), 202502-202503 (2005).

74.	K. Fossheim, E. D. Tuset, T. W. Ebbesen, M. M. J. Treacy and J. Schwartz, Physica C: Superconductivity **248** (3–4), 195-202 (1995).

75.	S.-L. Huang, M. R. Koblischka, K. Fossheim, T. W. Ebbesen and T. H. Johansen, Physica C: Superconductivity **311** (3–4), 172-186 (1999).

76.	P. Yang and C. M. Lieber, Science **273** (5283), 1836-1840 (1996).

77.	J. Wei, Y. Li, C. Xu, B. Wei and D. Wu, Materials Chemistry and Physics **78** (3), 785-790 (2003).

78.	S. X. Dou, W. K. Yeoh, J. Horvat and M. Ionescu, Applied Physics Letters **83** (24), 4996-4998 (2003).

79.	W. K. Yeoh, J. Horvat, S. X. Dou and V. Keast, Superconductor Science and Technology **17** (9), S572 (2004).

80.	J. H. Kim, W. K. Yeoh, M. J. Qin, X. Xu and S. X. Dou, Journal of Applied Physics **100** (1), 013908-013906 (2006).

81.   J. H. Kim, W. K. Yeoh, M. J. Qin, X. Xu, S. X. Dou, P. Munroe, H. Kumakura, T. Nakane and C. H. Jiang, Applied Physics Letters **89** (12), 122510-122513 (2006).

82.   W. K. Yeoh, J. Horvat, J. H. Kim, X. Xu and S. X. Dou, Applied Superconductivity, IEEE Transactions on **17** (2), 2929-2932 (2007).

83.   W. K. Yeoh, J. Horvat, S. X. Dou and P. Munroe, Applied Superconductivity, IEEE Transactions on **15** (2), 3284-3287 (2005).

84.   W. K. Yeoh, J. H. Kim, J. Horvat, S. X. Dou and P. Munroe, Superconductor Science and Technology **19** (2), L5 (2006).

85.   S. K. Chen, K. S. Tan, B. A. Glowacki, W. K. Yeoh, S. Soltanian, J. Horvat and S. X. Dou, Applied Physics Letters **87** (18), 182504-182503 (2005).

86.   S. X. Dou, W. K. Yeoh, O. Shcherbakova, D. Wexler, Y. Li, Z. M. Ren, P. Munroe, S. K. Chen, K. S. Tan, B. A. Glowacki and J. L. MacManus-Driscoll, Advanced Materials **18** (6), 785-788 (2006).

87.   B. Q. Wei, R. Vajtai and P. M. Ajayan, Applied Physics Letters **79** (8), 1172-1174 (2001).

88.   P. Kim, L. Shi, A. Majumdar and P. L. McEuen, Physical Review Letters **87** (21), 215502 (2001).

89.   M. M. J. Treacy, T. W. Ebbesen and J. M. Gibson, Nature **381** (6584), 678-680 (1996).

90.   S. X. Dou, W. K. Yeoh, O. Shcherbakova, J. Horvat, J. H. Kim, A. V. Pan, D. Wexler, Y. Li, W. X. Li, Z. M. Ren, P. Munroe and J. Z. Cui, Applied Physics Letters **89** (20), 202504-202503 (2006).

91.   J. H. Kim, S. Zhou, M. S. A. Hossain, A. V. Pan and S. X. Dou, Applied Physics Letters **89** (14), 142505-142503 (2006).

92.   H. Yamada, M. Hirakawa, H. Kumakura and H. Kitaguchi, Superconductor Science and Technology **19** (2), 175 (2006).

93. S. Zhou, A. V. Pan, D. Wexler and S. X. Dou, Advanced Materials **19** (10), 1373-1376 (2007).

94. F. G. Antonio Castro Neto, Nuno Miguel Peres, Physics World **19** (2006).

95. I. Meric, M. Y. Han, A. F. Young, B. Ozyilmaz, P. Kim and K. L. Shepard, Nat Nano **3** (11), 654-659 (2008).

96. A. A. Balandin, S. Ghosh, W. Bao, I. Calizo, D. Teweldebrhan, F. Miao and C. N. Lau, Nano Letters **8** (3), 902-907 (2008).

97. L. Gong, I. A. Kinloch, R. J. Young, I. Riaz, R. Jalil and K. S. Novoselov, Advanced Materials **22** (24), 2694-2697 (2010).

98. X. Xu, S. X. Dou, X. L. Wang, J. H. Kim, J. A. Stride, M. Choucair, W. K. Yeoh, R. K. Zheng and S. P. Ringer, Superconductor Science and Technology **23** (8), 085003 (2010).

99. K. S. B. De Silva, X. Xu, S. Gambhir, X. L. Wang, W. X. Li, G. G. Wallace and S. X. Dou, Scripta Materialia **65** (7), 634-637 (2011).

100. K. S. B. De Silva, S. Gambhir, X. L. Wang, X. Xu, W. X. Li, D. L. Officer, D. Wexler, G. G. Wallace and S. X. Dou, Journal of Materials Chemistry **22** (28), 13941-13946 (2012).

101. T. Szabó, O. Berkesi, P. Forgó, K. Josepovits, Y. Sanakis, D. Petridis and I. Dékány, Chemistry of Materials **18** (11), 2740-2749 (2006).

102. S. Stankovich, D. A. Dikin, G. H. B. Dommett, K. M. Kohlhaas, E. J. Zimney, E. A. Stach, R. D. Piner, S. T. Nguyen and R. S. Ruoff, Nature **442** (7100), 282-286 (2006).

103. C. Gómez-Navarro, R. T. Weitz, A. M. Bittner, M. Scolari, A. Mews, M. Burghard and K. Kern, Nano Letters **7** (11), 3499-3503 (2007).

104. Y. Xu, H. Bai, G. Lu, C. Li and G. Shi, Journal of the American Chemical Society **130** (18), 5856-5857 (2008).

105. R. Verdejo, F. Barroso-Bujans, M. A. Rodriguez-Perez, J. Antonio de Saja and M. A. Lopez-Manchado, Journal of Materials Chemistry **18** (19), 2221-2226 (2008).

106. D. Li, M. B. Muller, S. Gilje, R. B. Kaner and G. G. Wallace, Nat Nano **3** (2), 101-105 (2008).

107. X. Wang, L. Zhi and K. Mullen, Nano Letters **8** (1), 323-327 (2007).

108. G. Eda, G. Fanchini and M. Chhowalla, Nat Nano **3** (5), 270-274 (2008).

109. J. I. Paredes, S. Villar-Rodil, A. Martínez-Alonso and J. M. D. Tascón, Langmuir **24** (19), 10560-10564 (2008).

110. S. Niyogi, E. Bekyarova, M. E. Itkis, J. L. McWilliams, M. A. Hamon and R. C. Haddon, Journal of the American Chemical Society **128** (24), 7720-7721 (2006).

111. S. Stankovich, R. D. Piner, S. T. Nguyen and R. S. Ruoff, Carbon **44** (15), 3342-3347 (2006).

3 EXPERIMENTAL METHODS

3.1   Fabrication technique.

Fabrication of polycrystalline bulk samples are very important, it not only provides a much easier way for studying the new superconductors comparing with the single crystal samples but also paves the way for fabricating the superconducting wires and tapes. For MgB_2 bulk samples, they can be fabricated by different methods; in the research work of this thesis, diffusion method and in-situ method are employed.

3.1.1 Diffusion method.

The very first sample fabricated by the diffusion method was reported just a few weeks after the announcement of the superconductivity in MgB_2 [ref.]. In this report, MgB_2 wire was produced by sealing 100-mm-diam boron fiber [10] and Mg into a Ta tube with a nominal ratio of MgB_2. Considering that at 950 ^{o}C the low vapor pressure of Mg, about 200 Torr [9], it is believed that MgB_2 forms via a process of diffusion of Mg vapor into the boron grains.

For the MgB_2 pellets studied in this thesis, firstly the crystalline boron powders (99.999%) with particle size of 0.2-2.4 µm mixed with or without dopants were pressed into pellets. They were then put into iron tubes filled with Mg powders (325 mesh, 99%), and then the iron tubes were sealed at both ends. Given the loss of the Mg during the sintering, the atomic ratio between Mg and B was 1.2:2. The samples were sintered at 800 °C for 10 h in a quartz tube with flowing high purity argon gas. After that, the samples were furnace cooled to room temperature.

3.1.2 In-situ method.

The in-situ method is the most widely used method. It is also suitable for large scale industrial production, such as powder in tube (PIT) technique.

The in-situ method used in the research work of this thesis can be seen as the simplified method from PIT. First, the stoichiometric crystalline boron powder and magnesium powder were mixed well in the mortar by pestle for 30~40 min. Then the powder mixture were pressed into pellets and put into the iron tubes. The two ends of the tube were sealed and sintered in quartz tube with flowing high purity argon gas at various temperatures for 30 min, and furnace cooled to room temperature.

3.1.3 Wire prepared by powder-in-tube method.

The powder-in-tube (PIT) method is one of most popular technique for fabricating the superconducting wires such as Nb_3Tn, MgB_2, and BSCCO (2212 and 2223). Normally, the precursor powders were first packed into metal tube or sheath with one end sealed by aluminum foils and after packing the other end is also sealed with aluminum foils. The metal tube then was swaged by the swaging machine to reach the diameter which is suitable for dies used in the drawing process. The swaged tube was drawn through dies on the draw bench so that diameter of whole tube is the same. Repeating this process until the tube is suitable for wires, such 1.4 mm or 0.8 mm. The sheath material used in this research work is iron for its low cost. To get the final MgB2 phase, the wires were sintered in the furnace at 800 ^{o}C for 30 min.

3.2   Powder x-ray diffraction

To check the phase purity and determine the lattice parameters of the samples, powder x-ray diffraction measurement was performed on the GBC MMA X-ray diffractometer using the CuKα (λ=1.5406^{o}A) radiation. The bulk samples were

grinded into powder form and then fixed on the quartz slide with a drop of ethanol. Before the measurement, diffractometer was calibrated by the standard silicon sample. The scan range is from 10° to 90°.

3.3   Transport measurement.

The transport measurement was used to determine the superconducting transition temperature, the irreversibility filed (H_{irr}), upper critical field (H_{c2}) and the residual resistivity ratio (RRR). The temperature dependent AC resistivity in applied field up to 13T was measured by a Quantum Design (QD) 14T Physical Property Measurement System (PPMS) using the resistivity option.
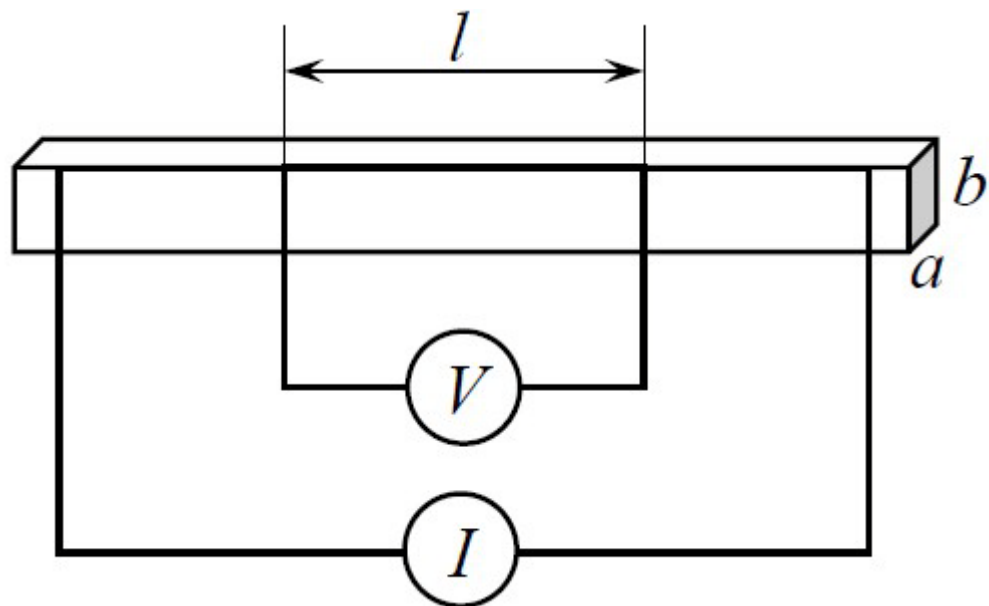
Figure 3.1 Schematic diagram of four probe resistivity measurement.

MgB$_2$ pellets were cut into bar shape and the resistivity measurement was made in a standard four probe geometry using the Silver Conductive Coating 18DB70X (Electron Microscope Science) to attach copper wires for the contacts (See figure). They were cured at 100 ^{o}C for 5 min or air cured for 24 h. For The typical contact

resistance is 1~3 ohm. The current limit, power limit, voltage limit, calibration mode and drive mode for the bridges are 1000A, 5000W, 95mV, standard and AC, respectively.

T_c was defined by the point where the resistivity starts to drop sharply. The H_{c2} and H_{irr} of a certain temperature were determined by measuring the temperature where the resistivity drops 10% and 90%, respectively, at a certain field. The transition width was defined by temperature difference between the two temperatures. The RRR is the ratio of the resistivity at 300k ($\rho_{(300K)}$) over the resistivity at 40K ($\rho_{(40K)}$).

3.4   Magnetization measurement.

Magnetization measurement was performed on a QD 14T PPMS using the Vibration Sample Magnetometer (VSM) option. The QD VSM for PPMS is a fast and sensitive DC magnetometer. The basic measurement is accomplished by oscillating the sample near a detection (pickup) coil and synchronously detecting the voltage induced. By using a compact gradiometer pickup coil configuration, a relatively large oscillation amplitude (1.3 mm peak) and a frequency of 40 Hz, the system is able to resolve magnetization changes of less than 10-6 emu at a data rate of 1 Hz.

For the zero field cooling (ZFC), the samples were cooled down to 25K, then applied the field with magnitude 50 Oe, and warmed up to the temperature 42K. For field cooling (FC), following the ZFC, the samples were cooled down to 25K. The transition temperature measured by the magnetization was defined by the temperature where the diamagnetic signal appeared.

For magnetic Jc calculation, magnetization measurement was performed on the bar with dimension of 1x2x3 cm^3 cut from the MgB$_2$ pellets. The field direction is

parallel with the length as seen in schematic Fig. 3.2. By using the Bean model, the magnetic J_c is deduced from $J_c = \frac{20\Delta M}{V[1-\frac{a}{3b}]}$ ($a < b$), where a and b are the dimensions of the sample perpendicular to the field, V is the sample volume, and $\Delta M = (|M+| + |M-|)/2$ (where $M+$ and $M-$ are the descending and ascending branches of the magnetization loop, respectively).

For bar shape $(b > a)$

$$J_c = \frac{20\Delta M}{a^2 bh\left(1-\frac{a}{3b}\right)}$$
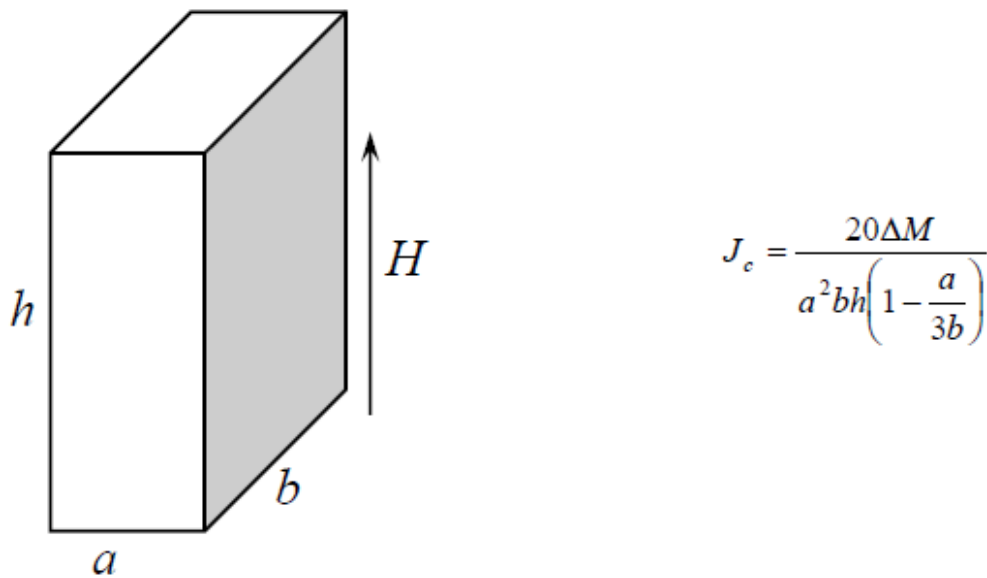
Figure 3.2 Schematic diagram of the sample shape and the direction relation of the field with the dimension.

3.5   Scanning electric microscopy.

To observe microstructure of the samples, the JEOL JSM-7500FA SEM was employed. The conventional scanning electron microscope with thermionic source and a large specimen chamber have practical magnifications up to several hundreds of thousands of times (100,000 – 200,000x). This allows observation of features down to a few tens of Angstroms (30-50A). Field emission scanning microscopy (FESEM) is widely used for surface observation of various nano materials and

medical, biological samples. It is also used in production lines for quality control, yield management, and failure analysis. The JSM-7500FA features enhanced performance, ease of operation, and energy efficiency. The microscope, in addition to its high performance at high accelerating voltage, has achieved a resolution of 1.4 nm at 1 kV by using gentle beam irradiation and minimizing power supply noise. It is highly resistant to floor vibration and acoustic noise to support tough installation requirements. Supporting a minimum accelerating voltage of 100 V in the lowest accelerating voltage range, the microscope is capable of imaging of the extreme surface of various samples.

4 EVIDENCE FOR TRANSFORMATION FROM ΔT_C TO ΔL PINNING IN MGB$_2$ BY GRAPHENE OXIDE DOPING WITH IMPROVED LOW AND HIGH FIELD J_C AND PINNING POTENTIAL

4.1 Introduction

In type-II superconductors, due to its short coherence length, the most effective elementary interaction between vortex and pinning center is core interaction, which originates from the coupling of locally distorted superconducting properties with the periodic variation of the superconducting order parameter. Inhomogeneities in different parameters cause different "elementary pinning mechanisms". There exists two predominant mechanisms of core pinning, i.e. δT_c pinning and δl pinning. Whereas δT_c pinning is caused by the spatial variation of the Ginzburg-Landau coefficient α associated with disorder in the transition temperature T_c, variations in the charge-carrier mean free path l near lattice defects are the main cause of δl pinning[1, 2]. For MgB$_2$ superconductor, it has been shown that δT_c pinning is dominant in un-doped MgB$_2$ samples, and δl pinning is dominant in carbon doped MgB$_2$ bulks, while δT_c and δl pinning coexist in silicone oil doped bulk samples[3-5]. But the systematical transformation from δT_c to δl pinning has not been observed.

Thermal energy may allow flux lines jump from one pinning site to another, which causes the finite resistivity below the transition temperature. It manifests a field-dependent broadening of the resistive transition. This phenomenon is very prominent in high temperature superconductors because of their large anisotropy induced by the 2D structure and high transition temperatures. With a layer structure and relatively high T_c, thermally activated flux flow also results in the field-dependent broadening of the resistive transition in MgB$_2$. But it exhibits different behaviour compared to the high temperature superconductors (HTS)[6-9]. First, the pinning potential, U_0, is

very large in low field, on the order of 10^4 K; second, it exhibits very strong field dependence in high field[10]. So far, research on MgB_2 has been focused on pristine samples, however, with only limited studies reported on doping effects on U_0 [11, 12].

Due to lack of intrinsic pinning, the J_c value of pristine MgB_2 drops very fast in field[13]. Chemical doping by nano-SiC, Si, C, and other carbon or silicon containing dopants has shown positive effects on high field J_c enhancement, however, the self field and low field J_c, as well as T_c, deteriorate[11, 14-18]. Recently, our team has found that graphene can improve J_c at self field and low field with very little reduction in T_c[12, 19, 20], but its high field J_c is not competitive with that of nano-SiC doped one. Also, we very recently found the graphene oxide (GO) doping can improve both the low and the high field J_c, which different from the above dopants[21].

In this work, we represent systematical study on the flux pinning mechanism of GO doped MgB_2 with much improved low field and high field J_c. By analysis of the flux pinning mechanism, the vortex pinning diagram is derived. According to the collective pinning theory, by adjusting the doping level the transformation from transition temperature fluctuation induced pinning, δT_c pinning, to mean free path fluctuation induced pinning, δl pinning, was observed. In additions, the pinning potential is enhanced in high field ($B > 5$ T) by GO doping.

4.2 Experimental

MgB_2 samples were fabricated via diffusion of magnesium into boron pellets. The GO was prepared by the Hummers method[22, 23]. The dried GO was ground and then sonicated by an ultrasonic vibrator in tetrahydrofuran (THF) for 1 h, so that a uniform GO suspension was achieved. Crystalline boron powder (99.999%) with particle size of 0.2-2.4 µm and GO suspension were first mixed in a mortar until the

mixture dried in the air. The mixture was pressed into pellets, which were then put into iron tubes filled with Mg powders (325 mesh, 99%), and then the iron tubes were sealed at both ends. The atomic ratio between Mg and B was 1.2:2. The samples were sintered at 800 °C for 10 h in a quartz tube with flowing high purity argon gas. After that, the samples were furnace cooled to room temperature.

The phases and crystal structures were characterized by powder X-ray diffraction. Measurements of the temperature- and field-dependence of the electrical resistivity and magnetization were performed using a physical properties measurement system (Quantum Design). Magnetic J_c was deduced from the Bean model: $J_c=20\Delta M/V[a(1-a/3b)]$ $(a < b)$, where a and b are the dimensions of the sample perpendicular to the field, V is the sample volume, and $\Delta M = (|M+| + |M-|)/2$ (where $M+$ and $M-$ are the descending and ascending branches of the magnetization loop, respectively).

4.3   Results and Discussion

Figure 4.1 (a) shows the powder X-ray diffraction patterns for un-doped, and 1 wt% and 2 wt% GO doped samples, respectively. No impurity phase can be detected in the un-doped sample, while there is a trace amount of MgO phase existing in the GO doped samples. An expanded view of the (002) and (110) peaks is shown in the inset of Fig. 4.1(a), where the peak intensity is normalized by the corresponding highest (101) peak. Within the accuracy of these measurements, no peak shift is observed in the (002) peak, indicating that the c-axis parameter remains unchanged with doping, while the (110) peak shifts systematically to higher angle with GO doping, which indicates that the a-axis parameter is reduced with increasing doping level. This

64
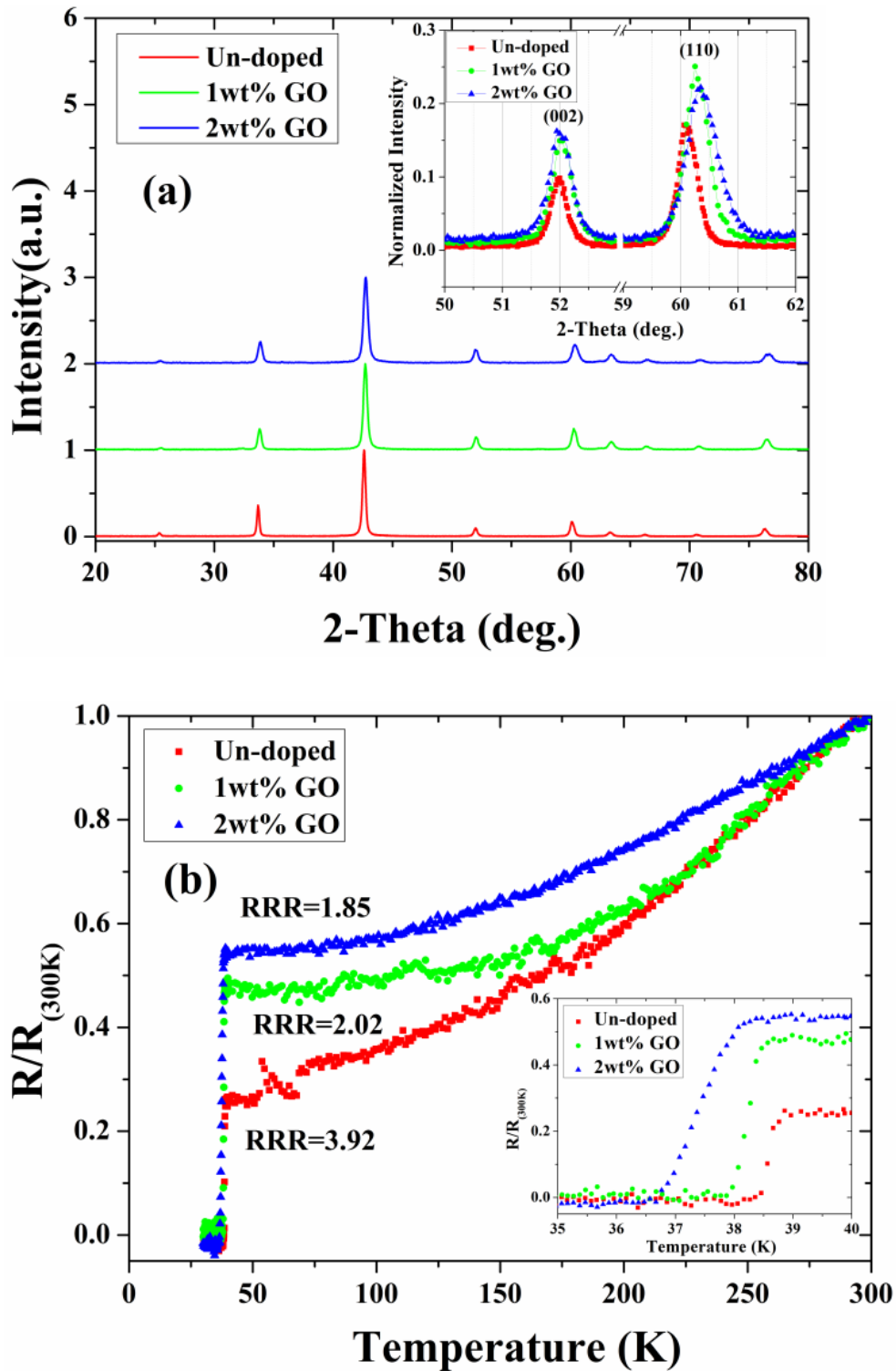
Figure 4.1 (a) X-ray diffraction patterns of the un-doped, 1 wt% GO doped, and 2 wt% GO doped samples. The inset shows selected regions of the XRD data. Note that whereas there is no detectable shift of the (002) peak, the (110) peak shifts systematically with carbon substitution. (b) Normalized resistivity as a function of temperature for un-doped and GO doped samples from 30 to 300 K. The inset shows an enlarged view of the transition region.

65

result is consistent with other types of carbon doped bulk MgB_2 samples[3, 4]. The shrinkage of the *a*-axis parameter indicates that the carbon released from GO has substituted onto B sites in MgB_2. The GO contains both C and O with extremely low dimensions, which is believed to be the origin of the improved properties. Meanwhile, broadening of both the (110) and the (002) peaks is observed. For the un-doped, and the 1 wt% and 2 wt% GO doped samples, the full width at half maximum (FWHM) of the (110) peak is 0.380, 0.456, and 0.569, respectively; the FWHM of the (002) peak is 0.344, 0.387, and 0.440, respectively. The peak broadening for the doped samples could have resulted from the decrease in the grain size or the increased strain caused by doping.

Figure 4.1 (b) shows the temperature dependence of the normalized resistivity of the un-doped and doped samples from 33 K to 300 K. For the GO doped samples, the normalized resistivity near T_c at 40 K is greater than for the un-doped sample. The T_c values and residual resistivity ratios, RRR = *R(300K)/R(40K)*, are 38.96, 38.77, and 38.47 K, and 3.92, 2.02, and 1.85, for the un-doped, and the 1 wt% and 2 wt% GO doped samples, respectively. Therefore, the GO doping does not alter the superconductivity significantly.
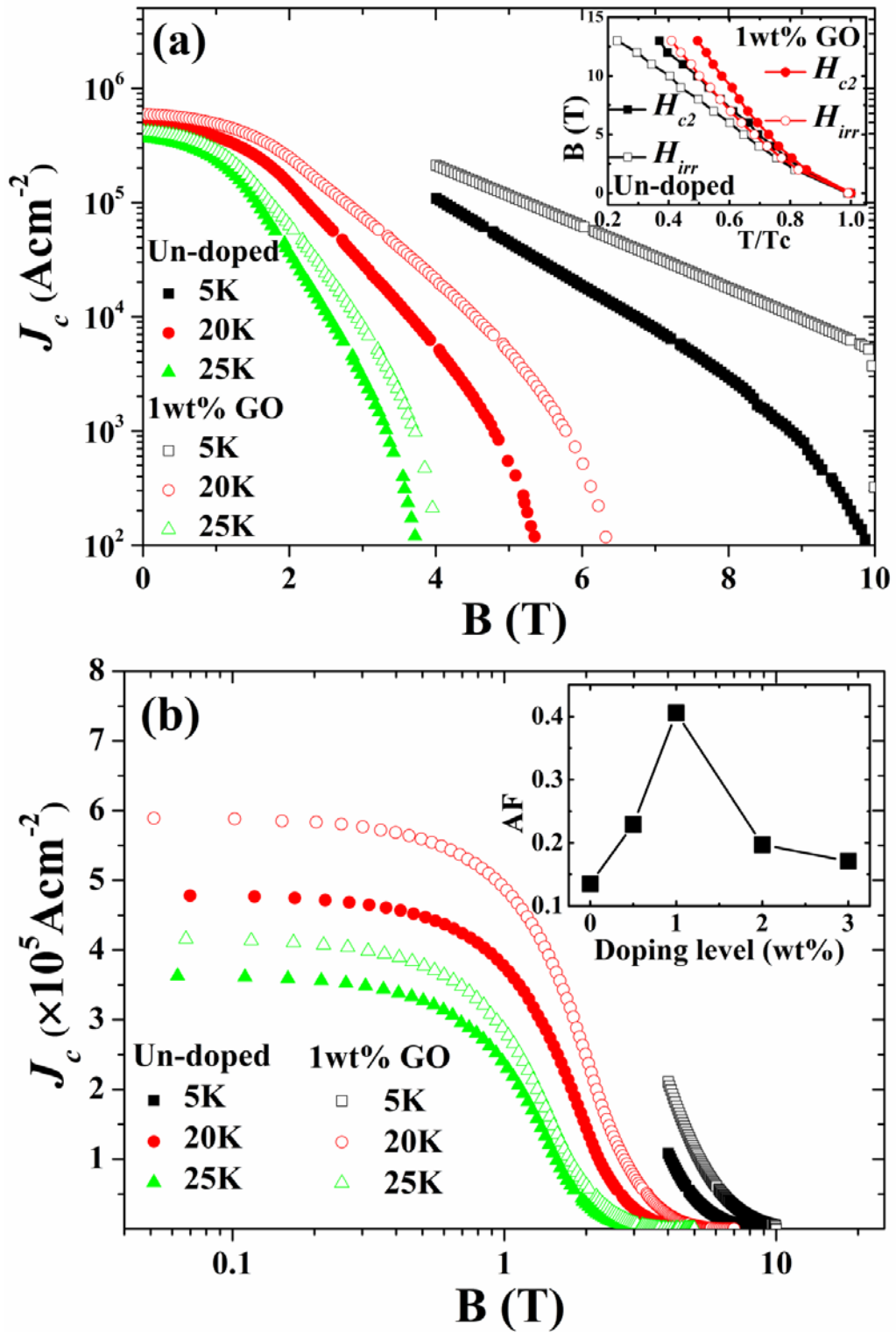
Figure 4.2 **(a)** Log Jc vs. B for un-doped and 1 wt% GO doped samples at various temperatures. The inset shows Hc2 and Hirr, which were deduced 0.9 and 0.1 of ρ(H,T). **(b)** Jc vs. log B for the un-doped and 1 wt% GO doped samples at various temperatures. The top inset shows the Jc at 0.05 T for the un-doped and 1 wt% GO doped samples, and the bottom inset shows that AF varies with different doping levels.

Figure 4.2(a) and (b) shows the magnetic field dependence of the critical current density J_c for the un-doped and 1 wt% GO doped MgB_2 at various temperatures. Fig. 4.2 (a) shows the high field J_c of the 1 wt% GO doped sample is enhanced compared with the un-doped sample from 5 K up to 25 K. For example, at 5 K and 10 T, the J_c for the un-doped sample is about 100 $A \cdot cm^{-2}$, approaching the irreversibility field, but with 1 wt% GO doping, the J_c is as high as 5200 $A \cdot cm^{-2}$, about 52 times as great. As shown in Fig. 4.1(b), GO doping increases the impurity scattering, which can cause an increase in the upper critical field (H_{c2}) and higher irreversibility field (H_{irr}). In addition, the defects, smaller grain size, and/or strain caused by doping could also improve the J_c in field. The enhanced H_{irr} and H_{c2} are shown in the inset of Fig. 4.2(a). Fig. 4.2(b) presents the low field J_c for the un-doped and 1 wt% GO doped samples. It can be seen that the low field J_c for 1 wt% GO addition is also improved compared with the un-doped sample. It is believed that the enhancement of J_c at low field is due to the improvement in the grain connectivity[24] and we used Rowell's model to calculate the effective conducting area or active fraction (A_F)[25]. Normally using the methodology of Rowell to estimate connectivity suggests that few alloyed samples of MgB_2 have connectivity fractions that exceed 0.1[26]. In the inset (b) of Fig. 1(b), it can be seen the effective conducting area is improved by doping with GO, the 1 wt% GO doped sample shows the best grain connectivity with A_F value of 0.4 comparing with 0.135 of un-doped sample. But after that, the effective conducting area show a decrease, which could be because a high concentration of GO decreases the volume of the superconducting phase.

(a) 2wt% GO Doped

Legend:
- □ 13K
- ○ 15K
- △ 18K
- ▽ 20K
- ◁ 23K
- ▷ 25K
- ☆ 28K
- ⬠ 30K
- ◑ 32K

(b) 23K

B_{sb}

B_{th}
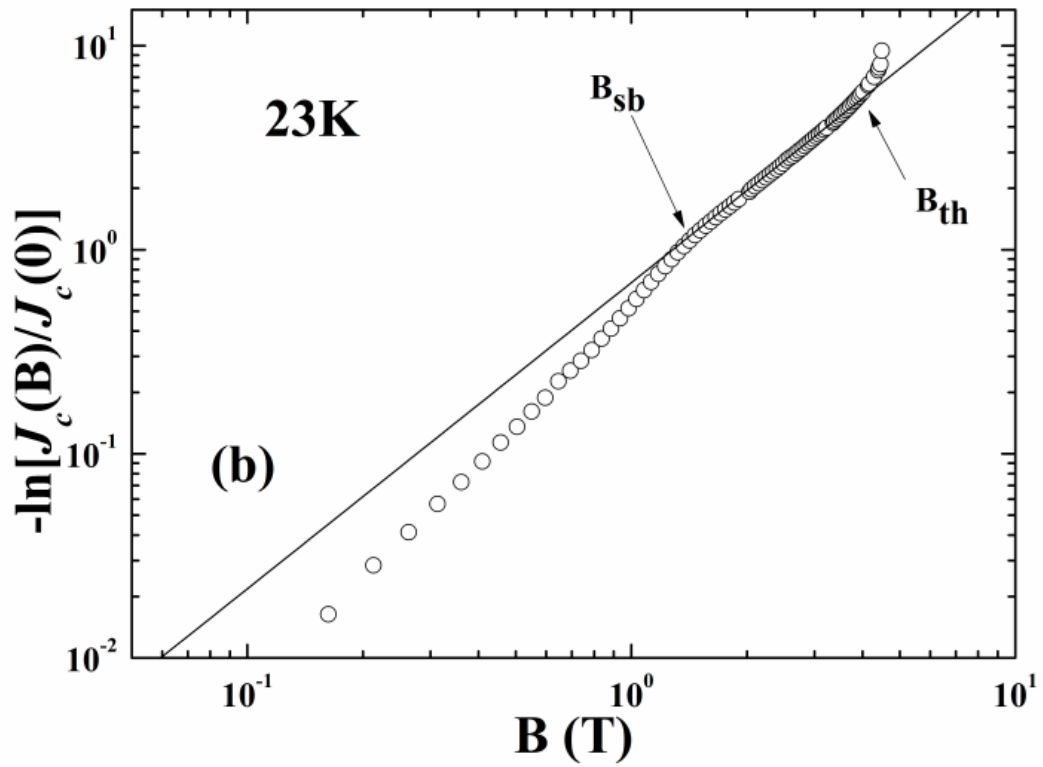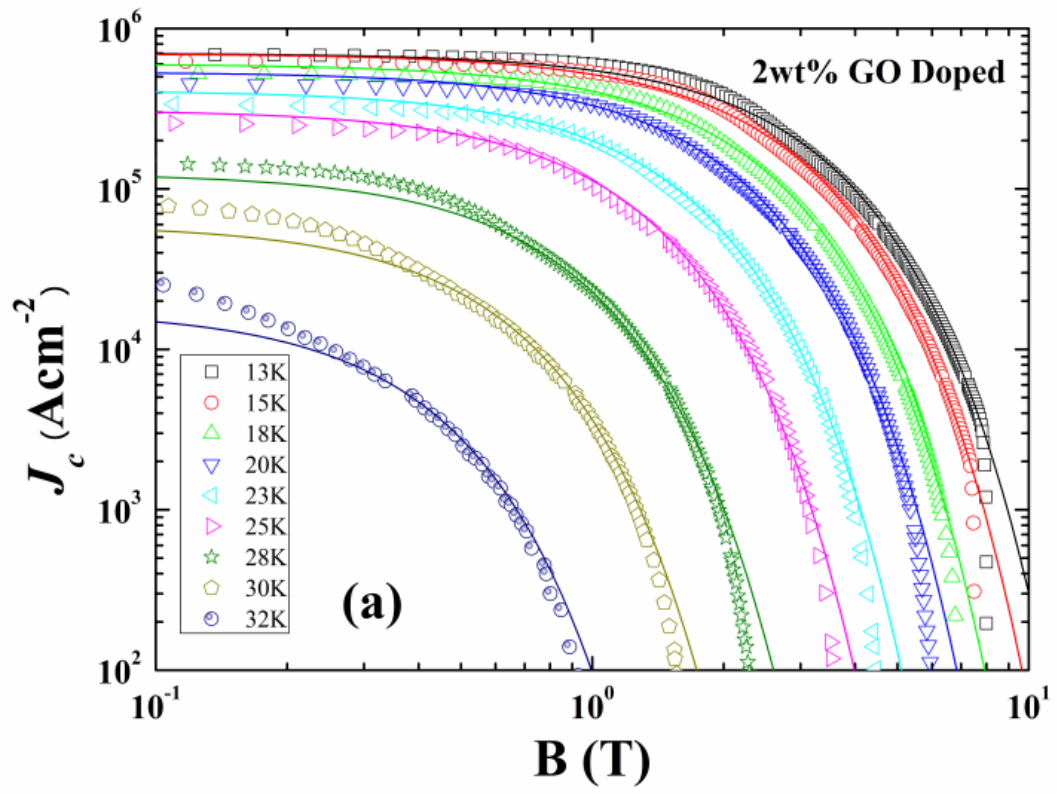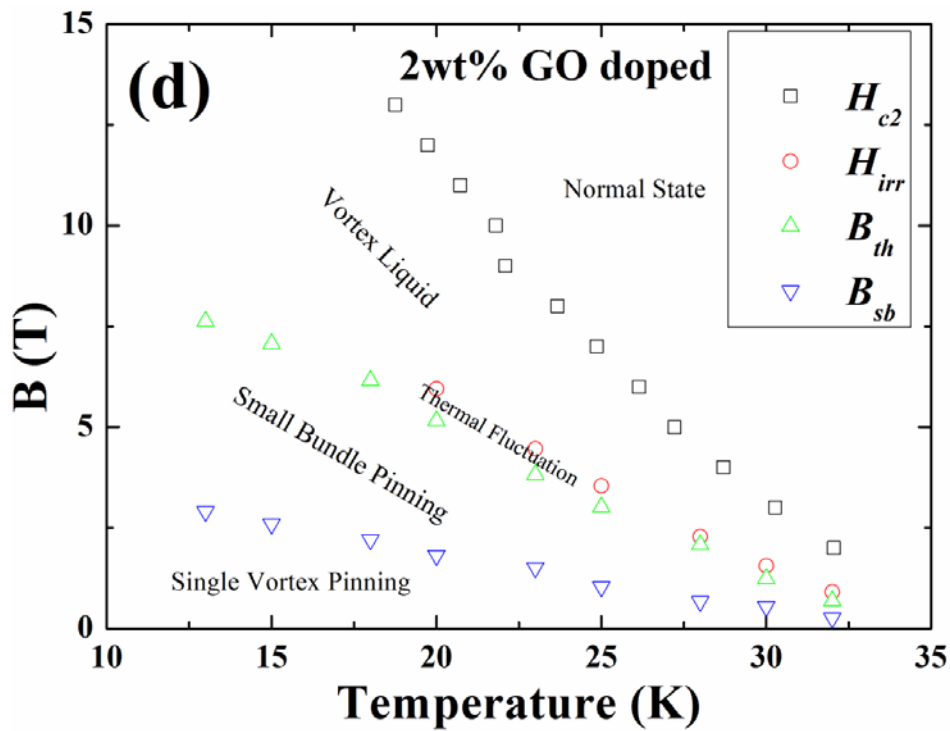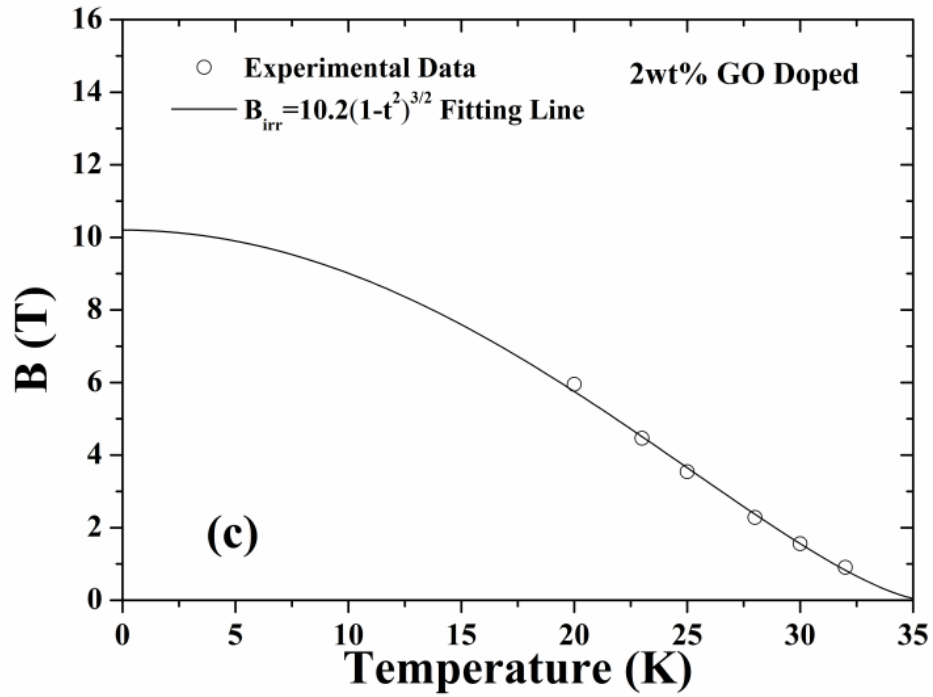
Figure 4.3 (a) J_c at various temperatures for the 2 wt% GO doped sample in a double logarithmic plot as log J_c

vs. log B. The solid lines are fits based on Equation (1). **(b)**. J_c at 23K for 2 wt% GO doped sample in double

logarithmic plot of $\ln[J_c(B)/J_c(0)]$ vs. log B. The solid line is the fitting line according to Equation (1). **(c)** The

irreversibility field obtained from the magnetic J_c curve by the criterion of 100 A·cm^{-2}. The solid line is a fit in

terms of the giant creep model. **(d)** B-T phase diagram of 2 wt% GO doped sample.

70

When the pinning is induced by uncorrelated disorder, the collective pinning theory has been proven very successful in describing the vortex behavior and analyzing the corresponding vortex pinning mechanisms in high temperature superconductors and MgB_2[1-3] According to this theory, the magnetic field dependence of J_c obeys different laws in different magnetic fields. First, when the magnetic field is smaller than B_{sb} (the crossover field from the single vortex to the small vortex bundle pinning regime), the J_c is field independent, exhibiting a plateau in the J_c-B diagram. Then, when $B > B_{sb}$ (in the small bundle pinning regime), $J_c(B)$ obeys an exponential law as

$$J_c(B) = J_c(0)exp[-(B/B_0)^{3/2}]. \tag{1}$$

Where B_0 is a constant. In Fig. 4.3 (a), we can observe the J_c plateau in the GO doped MgB_2 sample, which corresponds to the single vortex pinning regime. Using equation (1) for the small bundle pinning to fit the J_c curves, it can be seen that at intermediate field, the solid fitting lines fit the experimental data very well, while a deviation between the fitting line and the experimental data exists at low and high field. In order to clearly determine the crossover field B_{sb} from the single vortex pinning regime to the small bundle pinning regime, the data was replotted on a double logarithmic plot as $-ln(J_c(B)/J_c(0))$ vs. field, as shown in Fig. 4.3 (b). At intermediate field, a straight line was clearly observed, corresponding to the small bundle pinning regime. The deviation at low field of the fitting line from the experimental data is B_{sb}. Meanwhile, the deviation at high field firstly is considered as the transition from the small bundle pinning to the large bundle pinning regime, although the high-field experimental data cannot be fitted by the power law of $J_c(B)$. From Fig. 4.3 (a), the irreversibility field, H_{irr}, can also be determined by the

criterion $J_c = 100$ Acm^{-2}, which is shown in Fig. 4.3 (c). These data can be fitted by the following equation:

$$H_{irr}(t) = H_{irr}(0)(1-t)^{3/2} . \tag{2}$$

Where $t = T/T_c$. The data indicate that giant flux creep also plays an important role in the 2 wt% GO doped MgB$_2$ sample[27].

After deriving the B_{sb}, the crossover field to the thermal fluctuation regime (B_{th}), H_{irr}, and H_{c2}, we can then try to construct the vortex phase diagram, as shown in Fig. 4.3(d), where H_{c2} is deduced using the criteria of 0.9 of $\rho(H,T)$ at the transition to superconductivity by measuring the resistivity at varying temperatures and fields. Below B_{sb}, there is a single vortex pinning regime, while the small bundle pinning regime is in between the B_{sb} and B_{th}. There exists a small regime between B_{th} and H_{irr} governed by the thermal fluctuation effect. Above the H_{irr} and below the H_{c2} is the vortex liquid pinning regime, and above the H_{c2}, there is the normal state regime. Compared with the un-doped sample, the GO doped sample shows a wider vortex phase region due to the enhanced flux pinning and H_{c2}, which also can be seen in silicone-oil-doped samples[5].

Griessen *et al*[28] derived that in the single vortex regime of a system with randomly distributed weak pinning centers, for δl pinning and δT_c pinning, the J_c obeys the following laws, respectively

$$J_c(t)/J_c(0)=(1-t^2)^{5/2}(1+t^2)^{-1/2} \tag{3}$$

And $\qquad J_c(t)/J_c(0)=(1-t^2)^{7/6}(1+t^2)^{-5/6} \tag{4}$

Where t=T/T_c.

With this model, the δl pinning was found to be the dominant pinning mechanism in YBa$_2$Cu$_3$O$_{7-x}$ (YBCO) films, and δT_c pinning dominates in single domain

(Y,Pr)123[28, 29]. For MgB$_2$, δT_c pinning and δl pinning are respectively found in un-doped and carbon doped samples, and δT_c and δl pinning coexist in silicone oil doped bulk samples[3-5]. So far, however, there has been no report on systematical transformation of the pinning mechanism by using one dopant. Here, we observed that depending on the doping level of GO, the pinning mechanism is systematically transformed from δT_c to δl pinning. We used the two equations given above to fit the experimental data. Clearly, it can be seen that in Fig. 4.4 (a), the data for the un-doped sample is well fitted by the δT_c pinning model, which is consistent with reference[3]; in Fig. 4.4 (b) the data for the 1 wt% GO doped sample is in between the δT_c and δl fitting lines, which means that both δT_c and δl pinning play an important role; and Fig. 4.4 (c) shows that the 2 wt% GO doped sample is dominated by δl pinning.

In Fig. 4.4 (d) we use the normalized temperature dependence to give a clearer picture of the different temperature dependences of J_c for the un-doped, and the 1 wt% and 2 wt% GO doped samples. The transformation from the δT_c pinning to δl pinning is in a good agreement with the varying trend in the residual resistivity ratio (see Fig. 4.1(b)). That is, with increasing doping level, the RRR becomes smaller, and the electron scattering becomes stronger, therefore decreasing the charge carrier mean free path and increasing the δl pinning. This result can be ascribed to the low dimensionality of GO, which carries both C and O into the MgB$_2$ formation process. The simultaneous formation of MgB$_2$ with C incorporation, in combination with the formation of highly dispersed MgO within the MgB$_2$ matrix, results in multiple types of pinning centers, which are GO doping level dependent. Therefore, through adjusting the doping level, the electron scattering intensity can be tuned effectively.
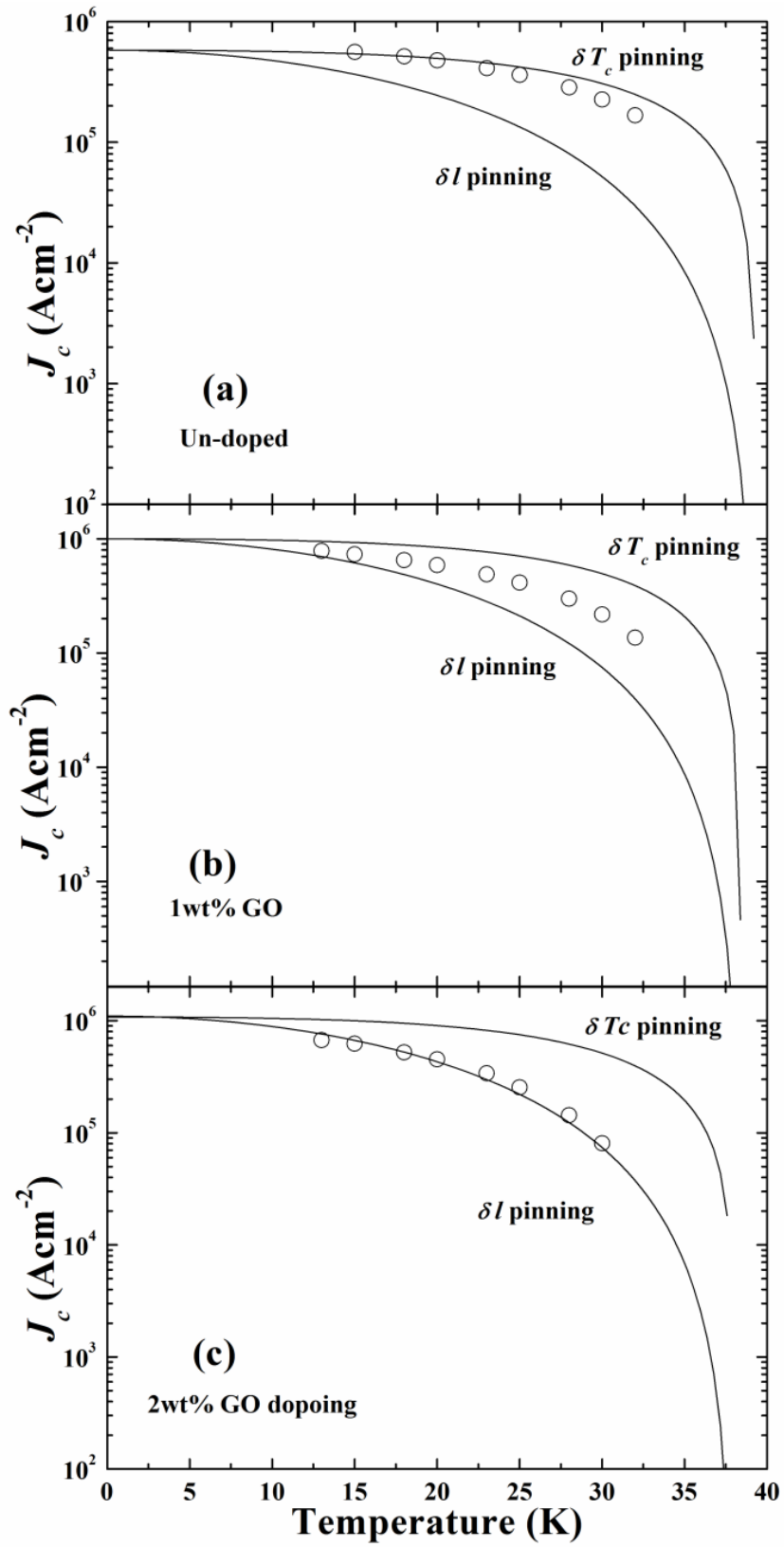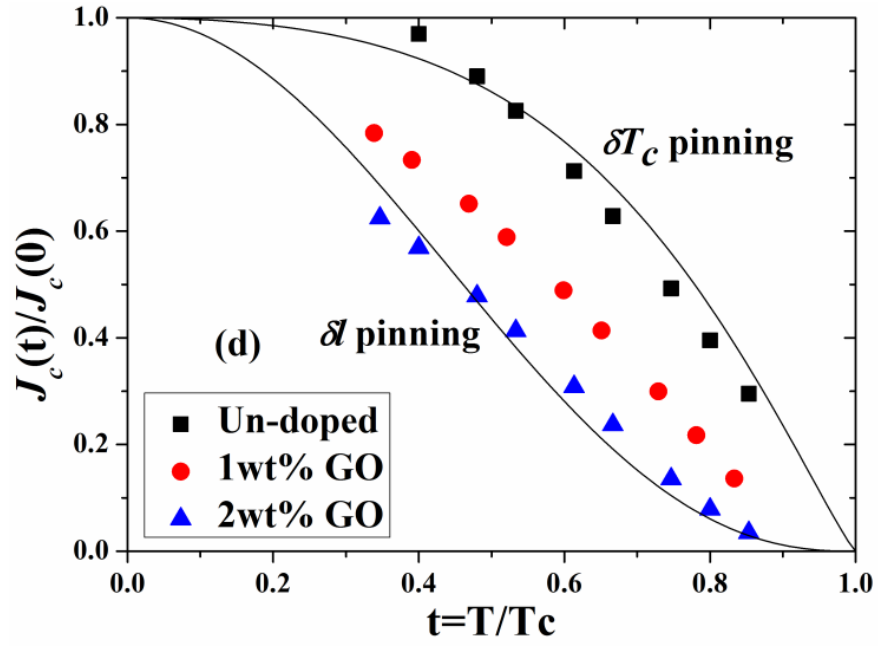
Figure 4.4 Temperature dependence of J_c at 0.05 T for un-doped (**a**), 1 wt% GO doped (**b**), and 2 wt% GO doped (**c**) samples. The solid lines are the fits to the J_c curves in terms of the δl pinning and δT_c pinning mechanisms. (**d**) Normalized temperature dependence of J_c for un-doped, 1 wt% GO doped, and 2 wt% GO doped samples.
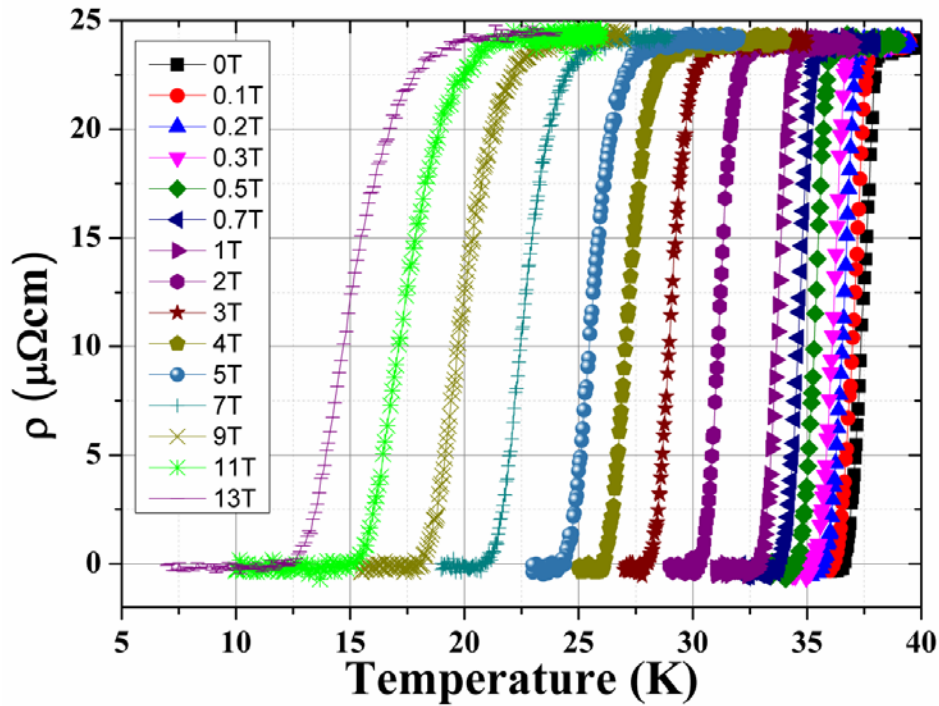
Figure 4.5 Temperature dependence of electrical resistivity for 2 wt% GO doped sample at different magnetic fields up to 13 T.
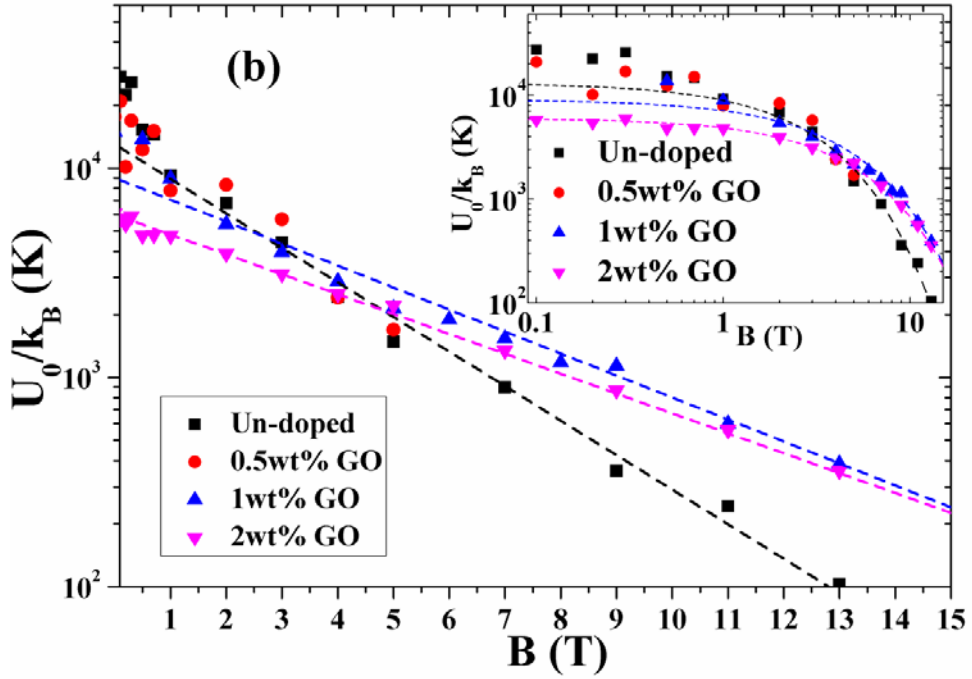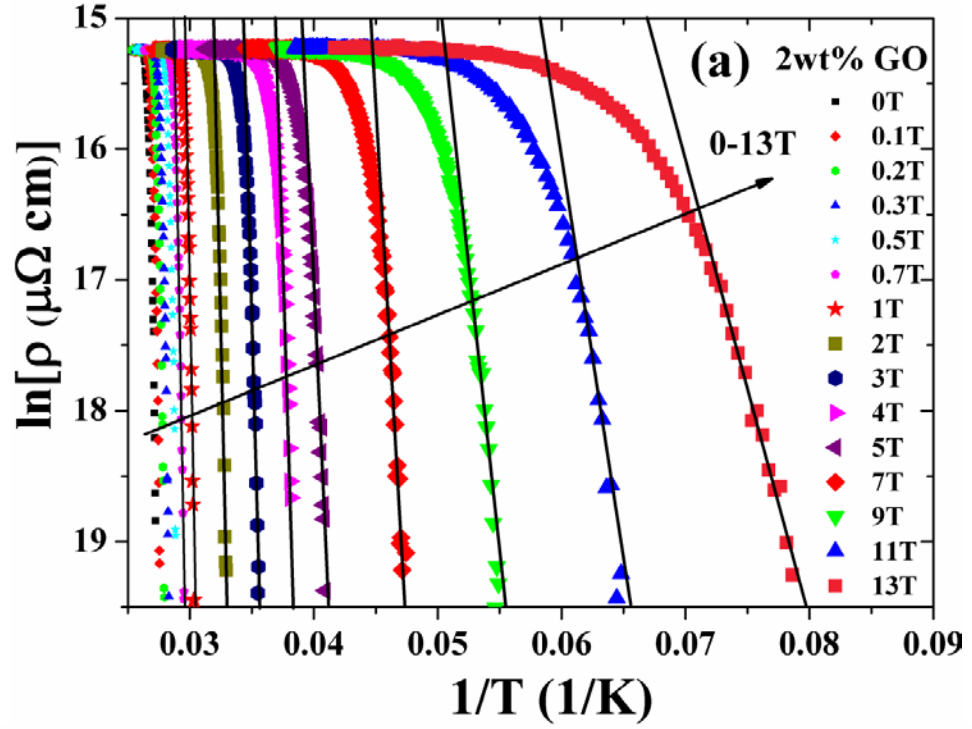
Figure 4.6 (a) Arrhenius plot of the electrical resistivity of 2wt% GO doped MgB$_2$ at various fields up to 13T. The solid lines are the fits of the linear part of the curves. **(b)** Field dependence of the pinning potential, U_0, for the un-doped, and the 0.5 wt%, 1 wt%, and 2 wt% GO doped samples. The dashed lines are the fits corresponding to each sample. The inset shows a double logarithmic plot of U_0/k_B versus B.

Now, let us discuss the GO doping effect on the pinning potential based on the model of thermally activated flux flow (TAFF). The field-dependent broadening of the resistive transition for the layered superconductors is interpreted by the dissipation of energy caused by thermally activated flux flow, which can be described by the Arrhenius law, $\rho(T,B)= \rho_0\exp[−U_0/k_BT]$, where U_0 is the flux-flow activation energy and deduced from the slope of the linear part of an Arrhenius plot, ρ_0 is a parameter, and k_B is Boltzmann's constant[1, 6]. This phenomenon was previously observed in the layered cuprate superconductors, un-doped bulk and thin film MgB_2, and iron based superconductors[6-10], but reports of doping effects on the pinning potential are very limited for MgB_2. Fig. 4.5 in supplemental material shows that the T_c is broadened upon applying magnetic field[22]. The transition width, defined by 90% to 10% of the corresponding resistivity transition, is about 0.99 K at zero field, while it is 3.85 K in 13 T[22]. We replotted the data as $\ln\rho$ vs. $1/T$, as shown in Fig. 4.6(a). The linear part of the transition is clearly observed, corresponding to the thermally activated flux flow regime. The pinning potential U_0 is obtained by calculating the slope. The U_0 values of other samples are also obtained by the same method. In Fig. 4.6(b), our results show that the U_0 values of the un-doped and doped MgB_2 samples exhibit a plateau in low field (B < 1T), but drop very fast in high field. In low fields, the pinning potential gradually decreases with increasing doping level. In high field, for the 0.5 wt% GO doped sample, the field dependence of the pinning potential is similar to that of the un-doped sample, whereas for the 1 wt% and 2 wt% GO doping samples, the U_0 shows different field dependence and is much larger than for the un-doped sample in high field (B > 5 T). Compared with the power law field dependence of the activation energy, $U_0 (B) \propto B^{-n}$ with the exponent n < 1, which is usually observed for other layered systems, such as HTS

and iron based superconductors[6-9], MgB_2 shows similar behavior in low field, but in high field it exhibits a much stronger field dependence (B > 1 T), which is consistent with MgB_2 films. The strong field dependence in high field can be fitted by the exponential law: $U_0 \approx 10^{-kB}$, where k is the fitting parameter and B is the magnetic field. From the inset of Fig 4.6(b), while there is deviation in low field between the fitting line and the experimental data for the un-doped, and the 0.5 wt% and 1 wt% GO doped samples, for the 2 wt% sample, the fitting line is in good agreement with the experimental data both at low and at high field.

4.4 Conclusion

In conclusion, we have systematically studied the flux pinning mechanism of GO doped MgB_2. By GO doping, J_c is enhanced significantly both at low and high field, which is due to the improvements in grain connectivity, H_{irr}, and H_{c2}. In the framework of the collective pinning theory, a *B-T* phase diagram has been derived for GO doped MgB_2. By adjusting the GO level, the pinning mechanism transforms from δT_c to δl pinning. Furthermore, in terms of the TAFF model, the pinning potential in high field (*B* > 5 T) is enhanced by GO doping.

4.5 References

1.   G. Blatter, M. V. Feigel'man, V. B. Geshkenbein, A. I. Larkin and V. M. Vinokur, Reviews of Modern Physics **66** (4), 1125-1388 (1994).

2.   W. Roger, Reports on Progress in Physics **62** (2), 187 (1999).

3.   M. J. Qin, X. L. Wang, H. K. Liu and S. X. Dou, Physical Review B **65** (13), 132508 (2002).

4.   J. L. Wang, R. Zeng, J. H. Kim, L. Lu and S. X. Dou, Physical Review B **77** (17), 174501 (2008).

5. S. R. Ghorbani, X. L. Wang, S. X. Dou, S.-I. K. Lee and M. S. A. Hossain, Physical Review B **78** (18), 184502 (2008).

6. T. T. M. Palstra, B. Batlogg, L. F. Schneemeyer and J. V. Waszczak, Physical Review Letters **61** (14), 1662-1665 (1988).

7. T. T. M. Palstra, B. Batlogg, R. B. van Dover, L. F. Schneemeyer and J. V. Waszczak, Physical Review B **41** (10), 6621-6632 (1990).

8. X. L. Wang, A. H. Li, S. Yu, S. Ooi, K. Hirata, C. T. Lin, E. W. Collings, M. D. Sumption, M. Bhatia, S. Y. Ding and S. X. Dou, Journal of Applied Physics **97** (10), 10B114-113 (2005).

9. X.-L. Wang, S. R. Ghorbani, S.-I. Lee, S. X. Dou, C. T. Lin, T. H. Johansen, K. H. Müller, Z. X. Cheng, G. Peleckis, M. Shabazi, A. J. Qviller, V. V. Yurchenko, G. L. Sun and D. L. Sun, Physical Review B **82** (2), 024525 (2010).

10. A. Sidorenko, V. Zdravkov, V. Ryazanov, S. Horn, S. Klimm, R. Tidecks, A. Wixforth, T. Koch and T. Schimmel, Philosophical Magazine **85** (16), 1783-1790 (2005).

11. J. Chen, V. Ferrando, P. Orgiani, A. V. Pogrebnyakov, R. H. T. Wilke, J. B. Betts, C. H. Mielke, J. M. Redwing, X. X. Xi and Q. Li, Physical Review B **74** (17), 174511 (2006).

12. K. S. B. De Silva, X. Xu, S. Gambhir, X. L. Wang, W. X. Li, G. G. Wallace and S. X. Dou, Scripta Materialia **65** (7), 634-637 (2011).

13. Y. Bugoslavsky, L. F. Cohen, G. K. Perkins, M. Polichetti, T. J. Tate, R. Gwilliam and A. D. Caplin, Nature **411** (6837), 561-563 (2001).

14. S. X. Dou, S. Soltanian, J. Horvat, X. L. Wang, S. H. Zhou, M. Ionescu, H. K. Liu, P. Munroe and M. Tomsic, Applied Physics Letters **81** (18), 3419-3421 (2002).

15. X. L. Wang, S. H. Zhou, M. J. Qin, P. R. Munroe, S. Soltanian, H. K. Liu and S. X. Dou, Physica C: Superconductivity **385** (4), 461-465 (2003).

16. J. H. Kim, S. Zhou, M. S. A. Hossain, A. V. Pan and S. X. Dou, Applied Physics Letters **89** (14), 142505-142503 (2006).

17. X. L. Wang, Z. X. Cheng and S. X. Dou, Applied Physics Letters **90** (4), 042501-042503 (2007).

18. X.-L. Wang, S. X. Dou, M. S. A. Hossain, Z. X. Cheng, X. Z. Liao, S. R. Ghorbani, Q. W. Yao, J. H. Kim and T. Silver, Physical Review B **81** (22), 224514 (2010).

19. K. S. B. De Silva, S. Gambhir, X. L. Wang, X. Xu, W. X. Li, D. L. Officer, D. Wexler, G. G. Wallace and S. X. Dou, Journal of Materials Chemistry **22** (28), 13941-13946 (2012).

20. K. S. B. De Silva, X. Xu, X. L. Wang, D. Wexler, D. Attard, F. Xiang and S. X. Dou, Scripta Materialia **67** (10), 802-805 (2012).

21. S. H. A. K S B De Silva, X Xu, X L Wang, W X Li, K Konstantinov and S X Dou, (Unpublished).

22. W. S. Hummers and R. E. Offeman, Journal of the American Chemical Society **80** (6), 1339-1339 (1958).

23. Y.-X. Wang, L. Huang, L.-C. Sun, S.-Y. Xie, G.-L. Xu, S.-R. Chen, Y.-F. Xu, J.-T. Li, S.-L. Chou, S.-X. Dou and S.-G. Sun, Journal of Materials Chemistry **22** (11), 4744-4750 (2012).

24. M. Eisterer, Superconductor Science and Technology **20** (12), R47 (2007).

25. M. R. John, Superconductor Science and Technology **16** (6), R17 (2003).

26. D. C. L. Y. Iwasa, M. Okada, R. Penco, M. D. Sumption, and X. X. Xi, IEEE Trans. Appl. Supercond. **16**, 1457 (2006).

27. Y. Yeshurun and A. P. Malozemoff, Physical Review Letters **60** (21), 2202-2205 (1988).

28. R. Griessen, H.-h. Wen, A. J. J. van Dalen, B. Dam, J. Rector, H. G. Schnack, S. Libbrecht, E. Osquiguil and Y. Bruynseraede, Physical Review Letters **72** (12), 1910-1913 (1994).

29. H. H. Wen, Z. X. Zhao, Y. G. Xiao, B. Yin and J. W. Li, Physica C: Superconductivity **251** (3–4), 371-378 (1995).

5 EFFECT OF GRAPHENE OXIDE AND SIC CO-DOPING ON SUPERCONDUCTIVITY OF MGB$_2$

5.1 Introduction

Since MgB2 was discovered in 2001[1], it has attracted vast number of efforts to apply this material to the real application because of its relatively high T_c 40 K, no grain boundary weak linkage issue [2]and cheaper cost compared with the HTS and also its easy preparation method such as powder in tube method (PIT)[3]. However, the critical current density (J_c) drops quickly as applied the external field for lacking the pinning sites in pristine MgB$_2$[4]. Thus, the enhancement of the flux pinning in MgB$_2$ and therefore improve its J_c is imperative.

The chemical doping such as nano-SiC[5], carbon[6], silicon oil[7], and carbohydrate[8] has been proven to be effective methods to introduce the pinning center and therefore enhance the in-field J_c. Until now, SiC is still one of the best dopants. Recently, the co-doping such as SiC with graphene[9] further enhanced the J_c formance comparing with only SiC doped samples. Very recently, in our group the graphene oxide was found to be another effective dopant to improve J_c[9, 10], so it motivated us to study the SiC and GO co-doping effect on enhancement of J_c MgB$_2$ samples were fabricated via diffusion of magnesium into boron pellets method. When preparing the co-doping samples, 2wt% GO was regarded as the optimum doping level of GO doping. On that base, 1wt%, 2wt %, 3wt% and 5wt% nano-SiC were added as another variable to see the doping effect. 2wt% GO doped sample and pure MgB$_2$ samples were prepared as references.

5.2 Experimental

The GO was prepared by Humer's method[11]. Before used as dopant in co-doped samples, the dried GO was ground and then sonicated by ultrasonic processor in Tetrahydrofuran (THF) for 1h. The crystalline boron powder (99.999%), nano-SiC (size <30 nm), and GO dispersion were first mixed in the mortar and then dried in the air. The mixture was pressed into pellets, which were put into the iron tubes filled with Mg powders (325 meshes, 99%), then the iron tubes were sealed. The atomic ratio between Mg and B is 1.2:2. The samples were sintered at 800 °C for 10 h in a quartz tube flowed with high purity argon gas. After that, the samples were furnace cooled to the room temperature. The phase and crystal structure of all samples were characterized by x-ray diffraction. The measurement of temperature- and field-dependent electrical resistivity and magnetization was performed in physical property measurement system (Quantum Design). H_{c2}(T) and H_{irr}(T) were defined as the field when the $\rho(H,T)=0.9\rho(H,T_c)$ and $\rho(H,T)=0.1\rho(H,T_c)$. Magnetic Jc was deduced from the Bean model: $Jc=20\Delta M/[a(1-a/3b)]$, with the sample size of $1\times2\times3$ mm^3.

5.3 Results and Discussion

Figure 5.1 shows the powder x-ray diffraction patterns for pure, 2wt% GO doped and 2wt% GO with various amounts of SiC co-doped samples. The XRD patterns indicate that the un-doped sample is MgB_2 single phase, while when doped with GO, trace amount of MgO appears in the sample. For the co-doped samples, besides the main phase MgB_2 and trace phase MgO, the Mg_2Si also exist as impurity phase, and the amount of Mg_2Si increase with the increasing of the SiC from 1wt% up to 5wt%.

For 5wt% SiC co-doped sample, there was a slight amount of SiC remain not reacted.

Figure 5.2 shows the lattice parameters for the *a* axis and *c* axis which are calculated

from the XRD pattern in Fig. 5.1. By doping with GO or GO + SiC, the lattice

parameter *c* remains the same but the for the lattice parameter *a* drops first by doped

with GO, however when co-doped with GO+SiC , a axis increase compared with the

GO doped one and remain the same level for all GO+SiC co-doped ones, The

variation of the lattice parameter can be understood as following: when MgB2 doped

with GO, the carbon released from GO will substitute the boron site which causing

the decrease of a but not decrease of c, when GO co-doped with SiC, the Si released

from SiC will also substitute into boron site and compensate the decrease of a axis.
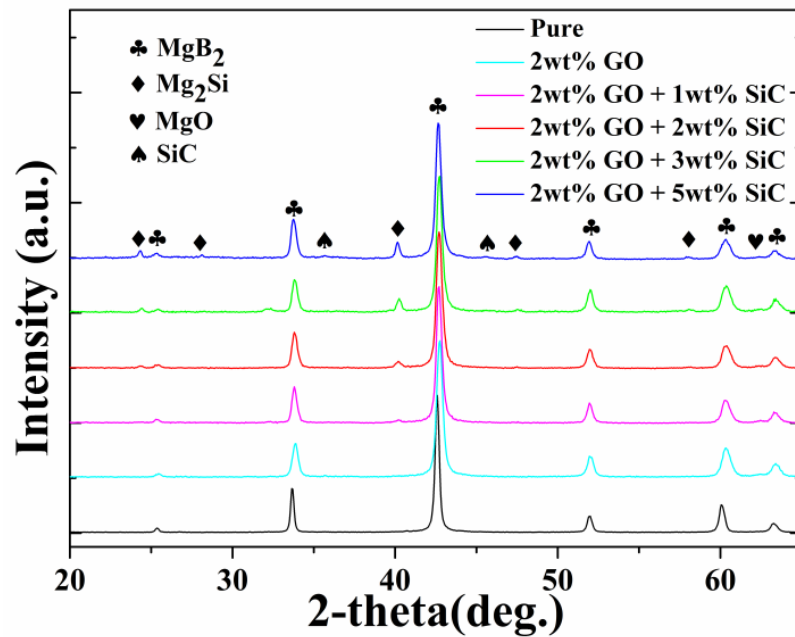
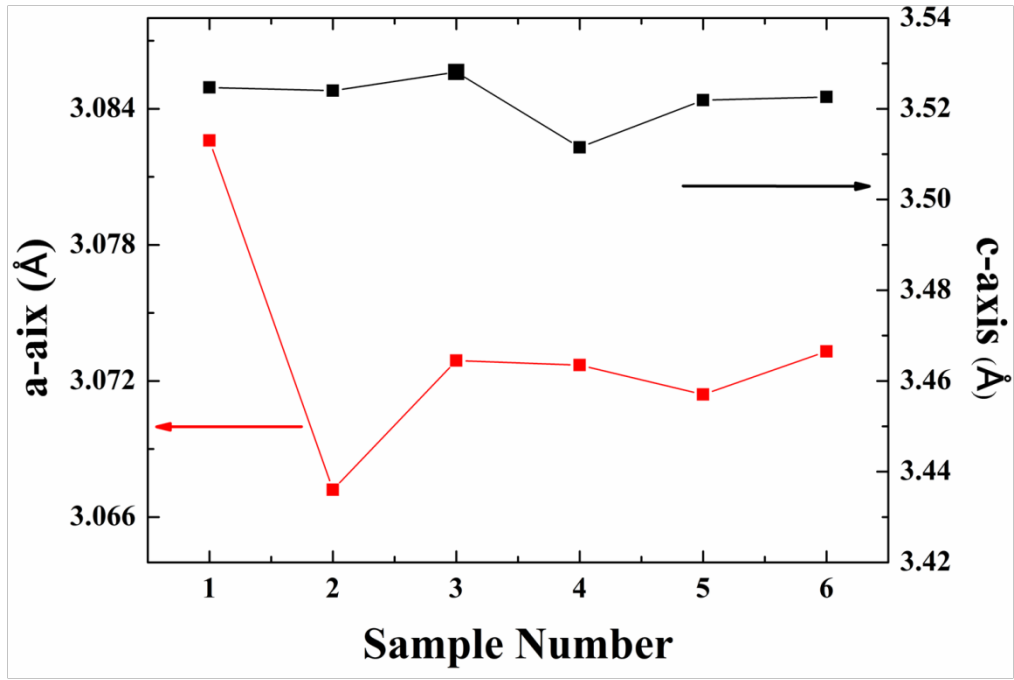**Figure 5.1** XRD patterns for un-doped, GO doped and GO and SiC co-doped MgB$_2$.

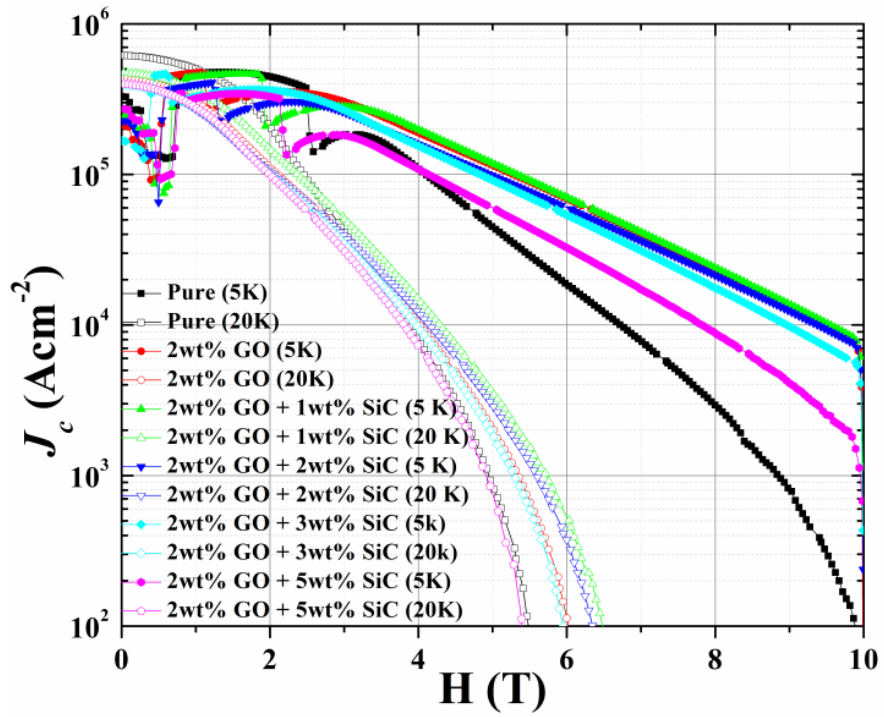**Figure 5.2** Lattice parameter a and c for un-doped, GO doped and GO and SiC co-doped MgB$_2$.

Figure 5.3 Magnetic J_c for for un-doped, GO doped and GO and SiC co-doped MgB$_2$.

85

Figure 5.3 shows the field dependence of the magnetic critical current density for pure, 2wt% GO doped and GO and SiC co-doped samples. It can be seen that 2wt% GO doping can enhance J_c at 9 T and 5 K for more than an order of magnititude. When co-doped with SiC, the low level of SiC such as 1 wt% and 2wt%, the in-field J_c at 5K is maintained comparing with 2wt% GO doping, while the in-field J_c at 20K is further enhanced. However, further increasing the amount of SiC the in-field J_c starts to decrease both at 5K and 20K.
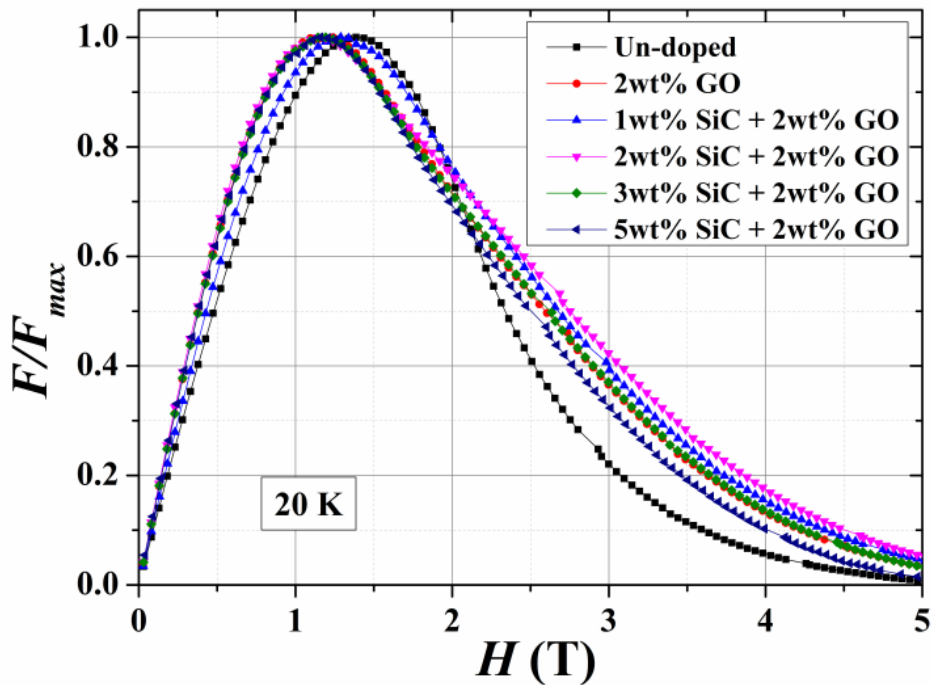
Figure 5.4 The normalized pinning force as function of field for un-doped, GO doped and GO and SiC co-doped MgB$_2$.

Figure 5.4 shows the volume pinning force normalized by the maximum pinning force as function of field for various samples. For the un-doped sample, the volume pinning force drops very fast after the pinning force reach the maximum value. For the 2wt% GO doped sample, the curve slope drops slower than the un-doped sample

after the force peak and show the enhanced pinning force. For the co-doped samples, 1wt% SiC and 2wt% SiC further enhanced the flux pinning but further increase the amount of SiC, the pinning forces began to decrease.
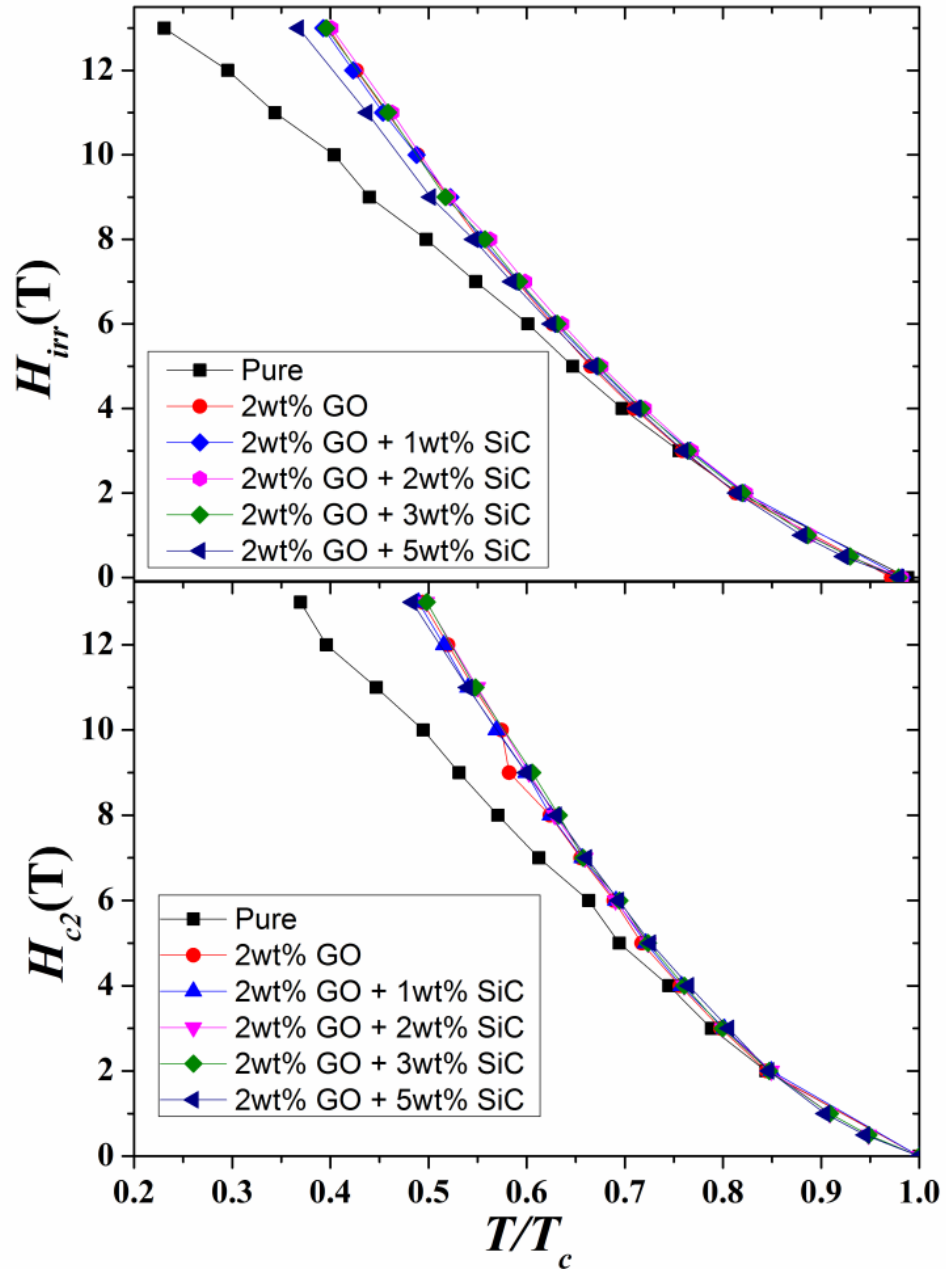
Figure 5.5 Upper critical field, H_{c2}, and irreversibility field, H_{irr}, for un-doped, GO doped and GO and SiC co-doped MgB$_2$.

From the Fig. 5.5 shows the H_{c2} and H_{irr} of the samples. The irreversibility field H_{irr} and H_{c2} could be deduced using the criteria of 0.1 and 0.9 of $\rho(H,T)$, respectively. Comparing with un-doped sample, the H_{c2} of GO and co-doping sample are enhanced significantly. According to $H_{c2}=\Phi_0/2\pi\xi^2\approx \Phi_0/2\pi\xi_0 l$. H_{c2} can be increase when the mean free path l become shorter, and doping with GO or GO+SiC can make the sample dirty and reduce the mean free path l and therefore enhance the H_{c2}. When the H_{c2} was improved, the H_{irr} can also been improved, furthermore the defects introduced by doping can also act as pinning centers and enhance the flux pinning and H_{irr}.
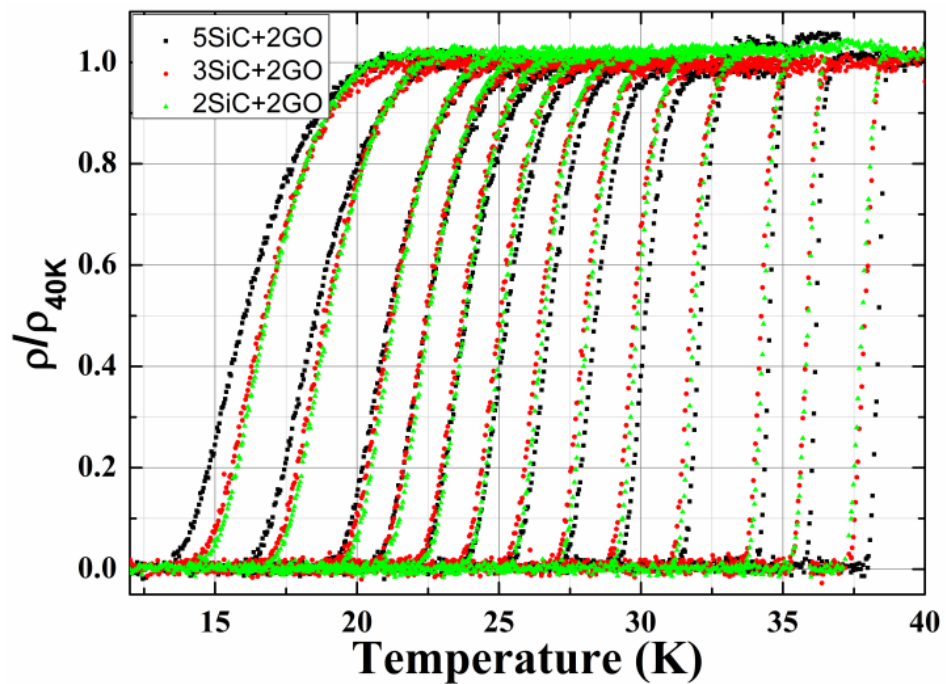
Figure 5.6 Field dependent broadening of superconducting transition $\rho(T)$ at several magnetic fields up to 13 T.
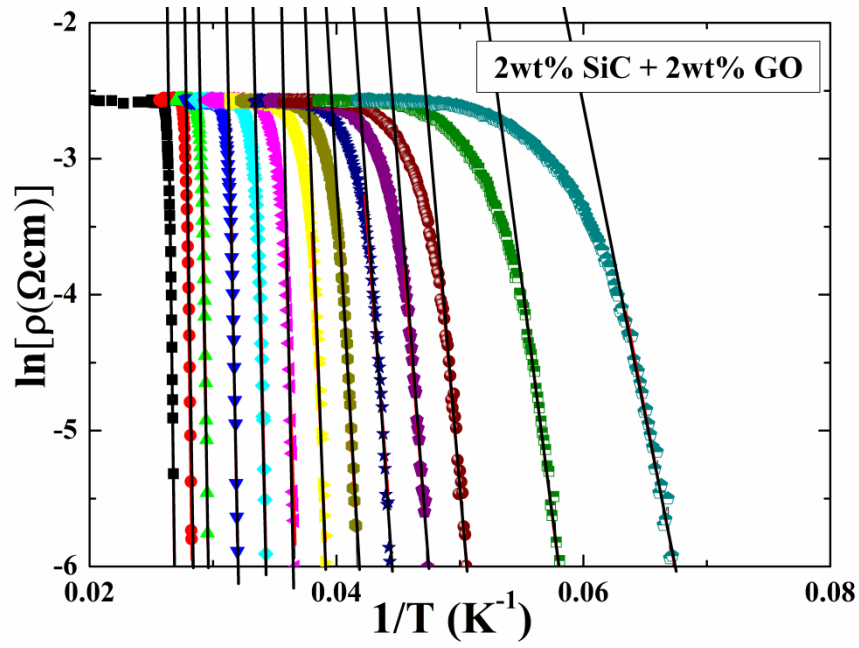
Figure 5.7 Arrenius plot of superconducting transition at various field up to 13T.
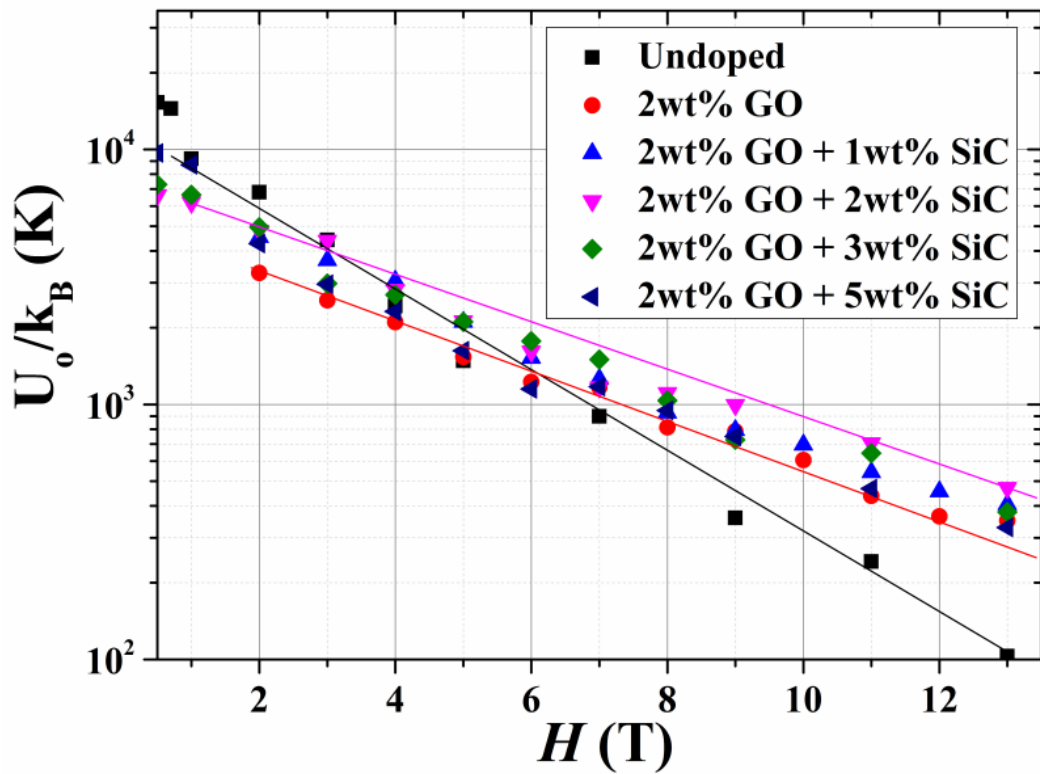

Figure 5.8 The resistive transition broadening in a magnetic field, which is similar to the high temperature superconductors.

The field-dependent broadening of the resistive transition for the layered superconductors is interpreted by the dissipation of energy caused by thermally activated flux flow, which can be described by the Arrhenius law, $\rho(T,B) = \rho_0\exp[-U_0/k_BT]$, where U_0 is the flux-flow activation energy and deduced from the slope of the linear part of an Arrhenius plot, ρ_0 is a parameter, and k_B is Boltzmann's constant[12]. This phenomenon was previously observed in the layered cuprate superconductors, un-doped bulk and thin film MgB_2, and iron based superconductors[12-16], but reports of doping effects on the pinning potential are very limited for MgB_2. The pinning potential of MgB_2 exhibit different features in magnetic field compared with high temperature superconductor. First the low field pinning potential is quite high at the order of 10^4, second the pinning potential show a strong field dependence, the pinning potential drops fast in high field while for high temperature superconductors the pinning potential remain constant. Furthermore, by GO doping the high field pinning potential can be further enhanced. Fig. 5.6 shows the field dependent broadening of GO + SiC co-doped samples. In order to get the pinning potential, the field dependent broadening of resistive was reploted into Arrenius plot. Fig. 5.7 shows the Arrenius plot of 2wt% SiC + 2wt% GO co-doped MgB2 as an example. From the linear part of the slope, the pinning potential was deduced. By using this method, the pinning potentials of other samples were also deduced as shown in the Fig. 5.8; it was shown that the pinning potential of MgB_2 can be enhance by GO and GO + SiC co-doping can further improve the high field pinning potential.

5.4   Conclusion

In summary, GO and SiC co-doping further improves the J_c at 20K and the pinning potential in high field. J_c vale at 4.2K, H_{c2} and H_{irr} show the similar trend comparing with the 2wt% GO doped sample. As presented in this paper, over doping will cause decrease of J_c, we expect reducing the amount of GO to less amount such as 1wt% or 0.5wt%, the J_c will be further increased. The sintering temperature and time also need to be optimized further to improve the performance.

5.5   References:

1.   J. Nagamatsu, N. Nakagawa, T. Muranaka, Y. Zenitani and J. Akimitsu, Nature **410** (6824), 63-64 (2001).

2.   D. C. Larbalestier, L. D. Cooley, M. O. Rikel, A. A. Polyanskii, J. Jiang, S. Patnaik, X. Y. Cai, D. M. Feldmann, A. Gurevich, A. A. Squitieri, M. T. Naus, C. B. Eom, E. E. Hellstrom, R. J. Cava, K. A. Regan, N. Rogado, M. A. Hayward, T. He, J. S. Slusky, P. Khalifah, K. Inumaru and M. Haas, Nature **410** (6825), 186-189 (2001).

3.   S. Jin, H. Mavoori, C. Bower and R. B. van Dover, Nature **411** (6837), 563-565 (2001).

4.   Y. Bugoslavsky, L. F. Cohen, G. K. Perkins, M. Polichetti, T. J. Tate, R. Gwilliam and A. D. Caplin, Nature **411** (6837), 561-563 (2001).

5.   S. X. Dou, A. V. Pan, S. Zhou, M. Ionescu, H. K. Liu and P. R. Munroe, Superconductor Science and Technology **15** (11), 1587 (2002).

6.   S. Soltanian, J. Horvat, X. L. Wang, P. Munroe and S. X. Dou, Physica C: Superconductivity **390** (3), 185-190 (2003).

7. X. L. Wang, Z. X. Cheng and S. X. Dou, Applied Physics Letters **90** (4), 042501-042503 (2007).

8. J. H. Kim, S. Zhou, M. S. A. Hossain, A. V. Pan and S. X. Dou, Applied Physics Letters **89** (14), 142505-142503 (2006).

9. K. S. B. De Silva, X. Xu, X. L. Wang, D. Wexler, D. Attard, F. Xiang and S. X. Dou, Scripta Materialia **67** (10), 802-805 (2012).

10. K. S. B. De Silva, S. Gambhir, X. L. Wang, X. Xu, W. X. Li, D. L. Officer, D. Wexler, G. G. Wallace and S. X. Dou, Journal of Materials Chemistry **22** (28), 13941-13946 (2012).

11. W. S. Hummers and R. E. Offeman, Journal of the American Chemical Society **80** (6), 1339-1339 (1958).

12. T. T. M. Palstra, B. Batlogg, L. F. Schneemeyer and J. V. Waszczak, Physical Review Letters **61** (14), 1662-1665 (1988).

13. T. T. M. Palstra, B. Batlogg, R. B. van Dover, L. F. Schneemeyer and J. V. Waszczak, Physical Review B **41** (10), 6621-6632 (1990).

14. X. L. Wang, A. H. Li, S. Yu, S. Ooi, K. Hirata, C. T. Lin, E. W. Collings, M. D. Sumption, M. Bhatia, S. Y. Ding and S. X. Dou, Journal of Applied Physics **97** (10), 10B114-113 (2005).

15. X. Wang, S. R. Ghorbani, G. Peleckis and S. Dou, Advanced Materials **21** (2), 236-239 (2009).

16. S. L. Prischepa, M. L. Della Rocca, L. Maritato, M. Salvato, R. Di Capua, M. G. Maglione and R. Vaglio, Physical Review B **67** (2), 024512 (2003).

CONCLUSIONS AND RECOMMENDATIONS

In conclusion, the GO doped bulk MgB_2 was prepared, the J_c enhancement both in low and high field was confirmed. flux pinning mechanism of graphene oxide (GO) doped MgB_2 has been systematically studied. In the framework of the collective pinning theory, a *B-T* phase diagram has been constructed. By adjusting the GO doping level, the pinning mechanism in MgB_2 transformed from transition temperature fluctuation induced pinning, δT_c pinning, to mean free path fluctuation induced pinning, δl pinning, is observed. Furthermore, in terms of the thermally activated flux flow model, the pinning potential in high field ($B > 5$ T) is enhanced by GO doping. The unique feature of GO is the significant improvement of both low field J_c and high field J_c.

GO and SiC co-doped MgB2 samples were also prepared. Graphene oxide and SiC co-doping effect on the superconductivity of MgB_2 was systematically studied by powder x-ray diffraction, transport and magnetization measurement. By Co-doping impurity phases Mg_2Si and SiC appeared and *a* axis decrease and *c* axis remain unchanged. Comparing with the un-doped samples, J_c can be further improved at high field for both of 5 K and 20 K. Comparing with the 2wt % GO doped sample, at 20 K the Jc was further enhanced by co-doping but at 5 K the J_c improvement is not obvious as at 20 K. At 20 K, the normalized pinning force shows enhancement at high field compared with un-doped one but decrease compared with 2wt% GO doped ones. The pinning potentials of co-doped samples were further enhanced at high field.

APPENDIX A TITLE

APPENDIX B TITLE